NUMERICAL AND EXPERIMENTAL STUDY OF MRI RF SIGNAL INTERACTIONS WITH VARIOUS MEDICAL DEVICES

A Dissertation

Presented to

the Faculty of the Department of Electrical and Computer Engineering

University of Houston

In Partial Fulfillment

of the Requirements for the Degree

Doctor of Philosophy

in Electrical Engineering

by

Yan Liu

December 2012

NUMERICAL AND EXPERIMENTAL STUDY OF MRI RF SIGNAL INTERACTIONS WITH VARIOUS MEDICAL DEVICES

_____

Yan Liu

Approved:

_____

Chairman of the Committee
Ji Chen, Associate Professor
Electrical and Computer Engineering

Committee Members:

_____

David Jackson, Professor
Electrical and Computer Engineering

_____

Donald Wilton, Professor Emeritus
Electrical and Computer Engineering

_____

George Zouridakis, Professor
Engineering Technology

_____

Driss Benhaddou, Associate Professor
Engineering Technology

_____

Suresh K. Khator, Associate Dean
Cullen College of Engineering

_____

Badrinath Roysam, Professor and Chairman
Electrical and Computer Engineering

Acknowledgements

I am deeply grateful to my dissertation advisor, Dr. Ji Chen, for his continuous research supervision, encouragement, and valuable suggestions. Without any of these, my research would have been impossible. As advisor, mentor, and friend, his influence and guidance will have a lasting effect on my career and my life.

I would like to express my sincere gratitude to the members of my advisory committee: Dr. David Jackson, Dr. Donald Wilton, Dr. George Zouridakis, Dr. Driss Benhaddou for their assistance and constructive criticism. I would like to appreciate Dr. Wolfgang Kainz from U.S. Food and Drug Administration for his valuable suggestion in my research. I would also like to thank the research sponsorship from St. Jude Medical and the support from the MRI team: Dr. Shirley Min, Ms. Shiloh Sison, Mr. Jon Dietrich and Dr. Gabriel Mouchawar.

I would like to thank the past and present members of our research group: Dr. Rui Qiang, Dr. Minsheng Wang, Dr. Jianxiang Shen, Dr. Yanmin Wu, Dr. Zubiao Xiong, Dr. Yanmin Yu, Dr. Songsong Qian, Mr. Hao Huang, Mr. Cong Gao, Mr. Shi Feng, Ms. Xichen Guo, Mr. Xiyao Xin, Mr. Xin Huang, Mr. Qinyan Wang, Mr. Dawei Li and Mr. Kuang Qin for their assistance, encouragement, and support. It was a great pleasure to work with them.

I would also like to thank Ms. MyTrang Baccam, Ms. Stephanie Shock, Ms. Mary Nguyen and all the other staff in the ECE department. They were of great help to me. Last, but not the least, I would like to thank my parents for their confidence in me and their encouragement at all times.

NUMERICAL AND EXPERIMENTAL STUDY OF MRI RF SIGNAL INTERACTIONS WITH VARIOUS MEDICAL DEVICES

An Abstract

of a

Dissertation

Presented to

the Faculty of the Department of Electrical and Computer Engineering

University of Houston

In Partial Fulfillment

of the Requirements for the Degree

Doctor of Philosophy

in Electrical Engineering

by

Yan Liu

December 2012

Abstract

This dissertation consists of three topics related to the RF-induced heating on medical devices in the magnetic resonance imaging (MRI) system. The first topic is the RF heating for passive medical devices. Electromagnetic simulation using the Finite Difference Time Domain (FDTD) method and thermal simulation are applied to understand the potential temperature increase inside the human body when the patient with an implantable device undergoes the MR scanner. Measurements are performed to validate simulation results. For devices with multiple components and complex structures, e.g., the external fixation devices, the RF heating mechanism is discussed extensively by investigating various parameters that can contribute to the device's RF heating effect.

The second topic is the RF heating for active implantable medical devices (AIMDs). It is studied using alternative approaches due to the fine features inside leads attached to AIMDs. The Tier 2 approach proposed by the International Electrotechnical Commission (IEC) is used to study the RF effect on leads tip under different configurations such as coil dimension, patient loading location in MRI, tissue properties as well as leads winding pattern. Due to the overestimation of the Tier 2 approach, another method based on the reciprocity theorem is used to establish the relationship between incident fields and field intensity at leads tip to estimate the temperature rise. This method is proven to be a powerful method to estimate the RF heating for leads structure on AIMDs.

The third topic covers the measurement uncertainty of using fiber optic thermal probes in the RF heating assessment. The fiber optic probes which are used to measure temperature rise around the medical device can lead to significant temperature variation from the original temperature without probes. Three medical devices have been

investigated to quantify the effect on the change of temperature rise due to the existence of thermal probes. It is found that thermal probes have more influence on the temperature rise around small and tiny structures such as screws and leads.

Table of Contents

List of Figures

List of Tables

Chapter 1 Introduction

1.1 Medical Device Conditioning in the MRI System

With the increased use of implantable medical devices and the fast spread of Magnetic Resonant Imaging (MRI) in the past 20 years, there have been concerns about the device compatibility and safety in the MRI systems. The interaction between the fields generated by the MRI system and medical devices implanted in a patient's body could produce magnetically-induced displacement force and torque, radio frequency (RF) heating, image artifact, and some electromagnetic compatibility problems on both active and passive implanted medical devices [1]. While most devices are manufactured using non-magnetic materials which efficiently control the displacement force and torque at a safety level, the RF-induced heating near the devices becomes a primary safety issue. Accordingly, MRI labeling is required for implants and devices to ensure patient safety according to the recommendations from the Food and Drug Administration (FDA). The procedures on establishing the labeling are based on those appropriate test methods presented by the American Society for Testing and Materials (ASTM) International. Sufficient testing needs to be performed in order to characterize the behavior of magnetically induced displacement force [2], magnetically induced torque [3] and RF heating [4] for medical devices.

With regard to MRI-related heating, the ASTM International has set forth test procedures that involve placing the implant in a gelled-saline-filled phantom in a "worst case" position and recording temperatures at multiple sites on implants during an MRI procedure using a relatively high level of radiofrequency (RF) energy, as indicated by the

specific absorption rate (SAR) [1]. Given the fact that many implants, especially orthopedic implants, may have complicated shapes as well as various possible dimensions depending on the clinical requirements (e.g., an orthopedic implant may have different lengths available depending on the size needed for the patient), it is particularly challenging to assess MRI-related heating for each of a given type of implant. Of further note is that to determine the worst case heating, it requires significant experimental efforts to test all possible sizes and combinations of the implant and to locate the maximum heating on the implant's surface. Using the ASTM heating phantom with the implant, it may be necessary to place multiple temperature probes on and around the periphery of the implant to identify the worst case heating location. Even by doing so it is not guaranteed that the maximum heating location will be found. Thus, the time and effort involved in properly studying the combinations of all these parameters experimentally can be prohibitive.

For active implantable medical devices (AIMDs) such as cardiac pacemakers and implantable neurological pulse generators (IPGs) it is even more difficult to measure the heating effect because of the implanted configuration variations for different patients [5]. For example, a pacemaker may have a different implanted location in the human pectoral region and leads may have different winding patterns with different venous access citing locations. In addition, the permittivity and conductivity for human tissues vary from patient to patient. Furthermore, commercial MRI coils coming from different manufactures have different dimensions. All of these variations may result in a huge data set that has thousands of combinations. Measurement is not enough to cover all these combinations. However, a study including numerical simulations for all representative

clinical implanted lead pathways as well as other variables can be more feasible for an MRI safety labeling evaluation. Some medical devices such as the external fixation system which is even not discussed in MRI safety standard documents also need an MRI safety evaluation.

Plenty of studies have been performed on MRI safety problems in the past [6]. Chou et al. investigated the RF heating of an implanted spinal fusion stimulator during MR scan [7]. Nyenhuis et al. studied the RF heating effect for leads structure in pacemakers [8][9]. Mattei et al. utilized a numerical model to estimate RF-induced heating on a pacemaker device and validated the results by experiment [10]. Martin et al. evaluated the cardiac pacemaker safety in a 1.5-Tesal MRI system [11]. Rezai et al. evaluated the heating effect for neurostimulation system in vitro [12]. Blouin et al. measured the thermal effect of electrode catheter in RF field [13].

1.2 Numerical Modeling of RF Induced Heating

With recent advances in numerical modeling for electromagnetic fields [14], it is now feasible to perform rigorous simulations of implant heating exposed to MRI conditions [15][16]. Therefore, rather than placing the implant inside the ASTM heating phantom and recording temperatures for each device from different configurations and sizes at various locations on the implant's surface, electromagnetic simulations may be used to determine the maximum heating location/position for each implant size and configuration. The numerical simulation results can provide the heating pattern for the entire implant surface. The finite-difference time domain is generally used in the numerical simulation which is also widely used in cell phone safety studies [17]-[21]. In addition, the surface heating pattern of various orientations relative to the incident

electric field can also be obtained. With simulation studies, it is possible to identify the worst-case heating for the entire device family. Then, only the worst-case heating configuration at the worst-case heating location on the implant's surface needs to be experimentally verified using the technique described by the ASTM International [4]. This combined modeling and experimental approach can quickly identify, in a cost-effective and timely manner, the worst case heating for an entire implant family.

This modeling approach typically begins with electromagnetic simulations to determine the SAR distribution and temperature rise in the vicinity of the implants in a gelled testing phantom. The ASTM heating phantom [4] is used for both the experimental and computational studies. Most modeling tools have the capability of directly importing engineering designs in their native CAD (Computer Aided Design) format, which significantly simplifies the modeling procedure. By being able to use the original CAD data of the implant, it is possible to accurately represent the device in the computational tool. This accurate representation of the implant guarantees correct thermal heating patterns from practical medical device designs. Once simulation results are obtained, the measurement shall be performed to ensure the accuracy of EM and thermal modeling.

Chapter 2 Methodology

2.1 Introduction of MRI RF Coil

Over the past decade, various RF coils have been developed. They can be categorized into two categories. The first category is the volume coil and the second category is the surface coil [22]. For MRI imaging purposes, a highly uniform B1 field is often required. If the B1 field is not uniformly distributed on the prospective imaging plan, the image will be largely altered. Surface coils have a relatively poor B1 field homogeneity and are mainly used as receiver coils. In the volume coil, the birdcage coils are most popular because they can produce a very homogeneous B1 field over a large volume within the coil. These coils are often used for both transmission and reception. In this study, the RF volume coil is used as the transmitting coil.

2.2 Numerical Modeling of MRI Environment

2.2.1 Modeling of Birdcage RF Coil using the FDTD Method

SEMCAD X is a commercial full-wave electromagnetic and thermal simulation package [23]. In the following simulation studies, SEMCAD X is used to model the interactions between MRI RF signals and medical devices. In most commercial MRI scanners, the high pass RF coil is used. Other types of RF coils are low pass and band pass RF coils. For 1.5 T and 3 T systems, the high pass coil should work at two different frequencies: 64 MHz and 128 MHz. A physical RF coil is usually difficult to model because it requires the information of the detailed RF coil size, included the shape and size of the individual rungs and end-rings. And the simulation takes a much longer time.

It has been shown that using a non-physical coil could reduce the simulation time while providing the same result as that from a physical coil [23]. Therefore, rather than modeling the exact physical coil, the non-physical coil is modeled in this study. For simplicity, the RF coil only has eight lungs as provided by the SEMCAD model as shown in Figure 2-1.

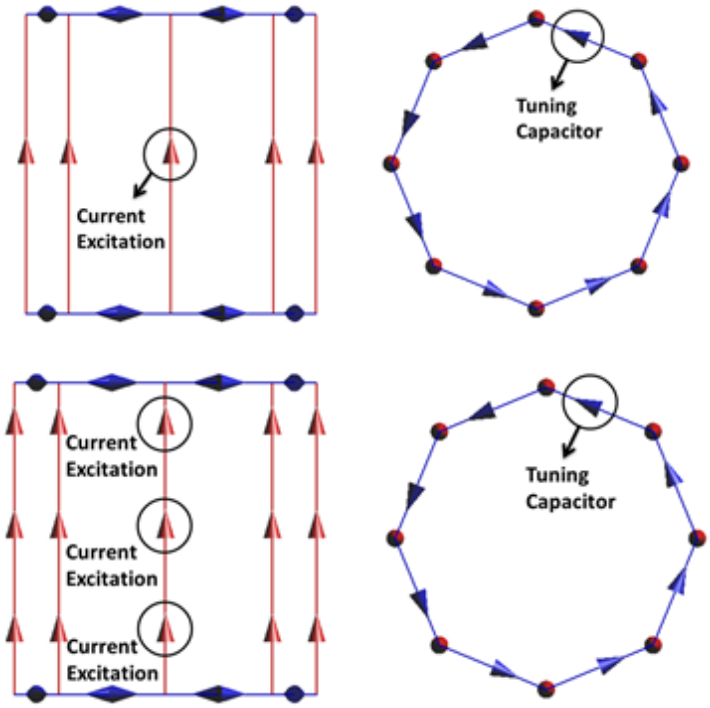

Figure 2-1 1.5-Tesla RF Coil (Top) and 3-Tesla RF Coil (Bottom) Models in SEMCAD.

The top two models are for the 1.5-T RF coil, and the bottom two models are for the 3-T RF coil. The red arrows correspond to the current excitation while the blue arrows correspond to the end ring capacitor. To ensure a uniform magnetic field inside the RF coil for the 3-T system RF coil as shown in the bottom left figure, one needs to add three constant current sources for each lung and re-adjust the capacitor values on the end ring. The diameter of the RF coil is 63 cm. The height of the RF coil is 65 cm. The capacitance value is determined from several broadband simulations so that the second

highest resonant frequency was set to 64 MHz for 1.5-Tesla and 128 MHz for 3-Tesla. The detailed steps are: 1) Set an initial capacitance value for all capacitors on end rings and add a broadband pulse signal on one single rung. The other seven rungs are modeled as zero ohm resistors. 2) After the simulation, the power spectrum is extracted. If the second highest resonant frequency is not at 64 MHz, the capacitance needs to be adjusted. 3) After three to five broadband simulations, the second highest resonant frequency needs to be located at 64 MHz as shown in Figure 2-2.

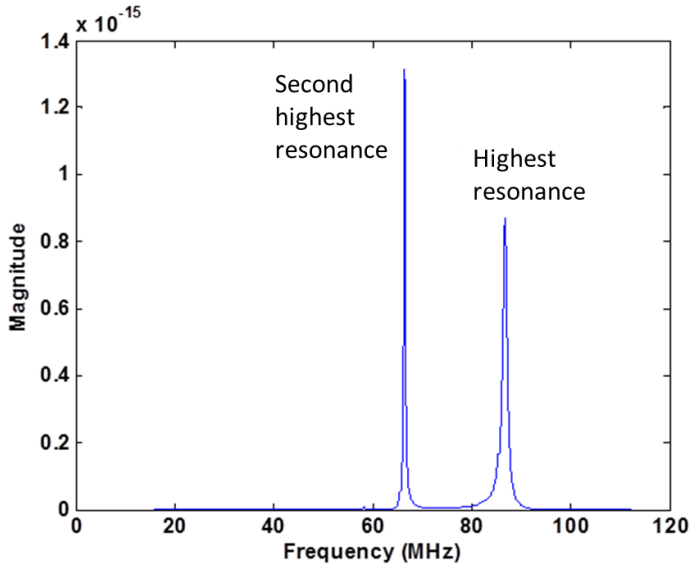

Figure 2-2 Spectrum of 1.5-Tesla MRI RF coil excited by broadband signal with end ring tuning capacitance = 7.2 pF.

From our study, the capacitance for the end ring tuning capacitor is 7.2 pF for 1.5-Tesla RF coil and 1.3 pF for the 3-Tesla RF coil. Figure 2-3 shows the electric and magnetic field distribution at the coil center inside the RF coil. The electric field is centrosymmetric and decreases along the radial direction. The magnetic field is uniformly distributed. From Figure 2-2 and Figure 2-3, it is concluded that the RF coils are

operating at the right resonant mode and the field patterns are also correct. Thus, the RF coils can be used for the following simulation studies.

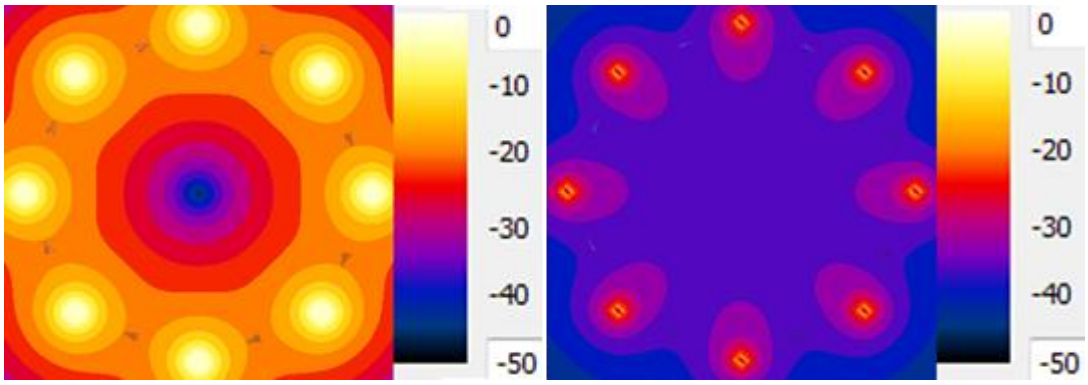

Figure 2-3 Electric Field (Left) and Magnetic Field (Right) distributions at center plane of MRI RF Coil.

2.3 ASTM Testing Procedure

Once the RF coils were developed and their operating modes were verified, it was necessary to determine the location of the maximum electric field inside the ASTM heating phantom [4]. To evaluate the maximum electric field inside the ASTM phantom, the ASTM heating phantom was placed into each RF coil as shown in Figure 2-4. The center of the "trunk" section of the ASTM phantom was placed at the center of the RF coil. The bottom of the phantom was 23.85 cm above the lowest point of the RF coil, mimicking the sliding bed configuration equivalent to an actual clinical MRI setup. The ASTM phantom consists of a plastic box with $\varepsilon_r = 3.7$ and $\sigma = 0$ S/m.

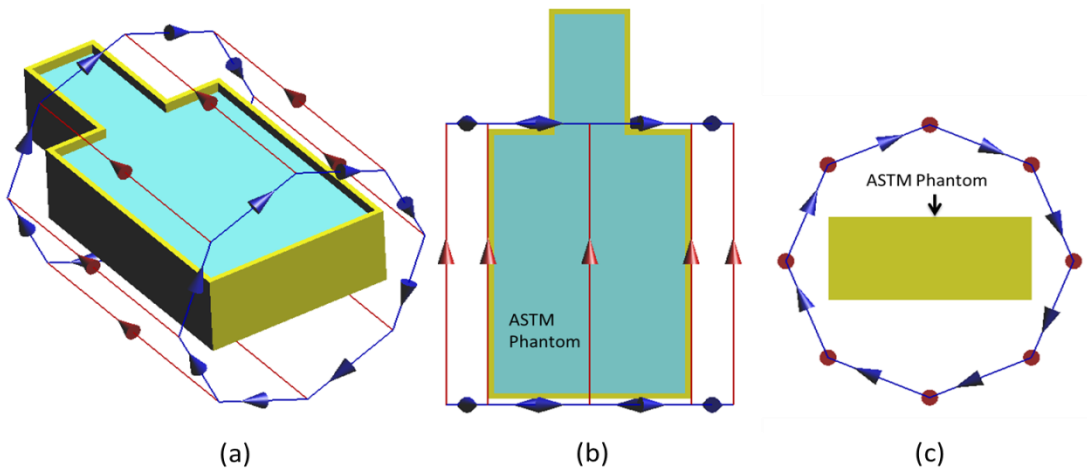

Figure 2-4 The illustration simulation setup to determine the maximum electric field location inside the ASTM heating phantom.

With this phantom placement, electromagnetic simulations were performed to determine the electric field distributions within the ASTM heating phantom. Figure 2-5 shows the top view of the electric field distributions in the center plane. Figure 2-6 shows the side view of the electric field distribution in the plane along the center cut (vertical direction) of the phantom. As shown in the figures, the maximum electric field locations are near the side walls of the phantom as indicated by Nordbeck et al. [24], along the center for both horizontal and vertical directions. Thus, these locations were selected to place the implant to maximize the exposure and minimize the measurement uncertainty relative to MRI-related heating. While there are other locations, such as the corners of the ASTM heating phantom that have very large electric fields due to "edge effects," these were not chosen since the region is very small and not suitable for implant placement. According to the side view, the electric field has a tilted angle to the boundaries of the gelled phantom. The tilted angle is due to the circular polarized field pattern inside MRI RF coil.

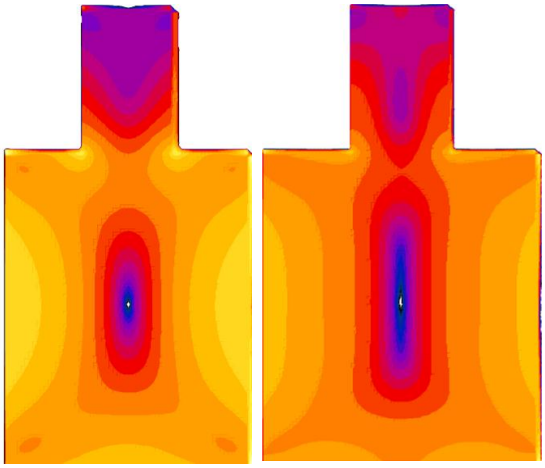

Figure 2-5 The electric field distribution for 1.5-T/64-MHz (left) and 3-T/128-MHz (right) MR systems in ASTM heating phantom (Top View).

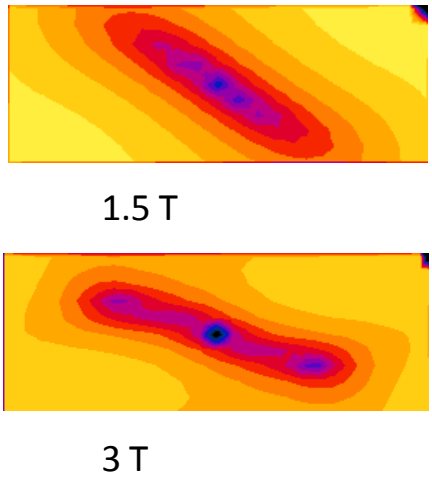

Figure 2-6 The electric field distribution for 1.5-T/64-MHz (top) and 3-T/128/MHz (bottom) systems in ASTM phantom (Side View).

The next step was to place the implants of different sizes inside the ASTM phantom as shown in Figure 2-7. The spacing between the devices and the side wall is at 2 cm for all simulations. With such appropriate placement, the EM study can be executed.

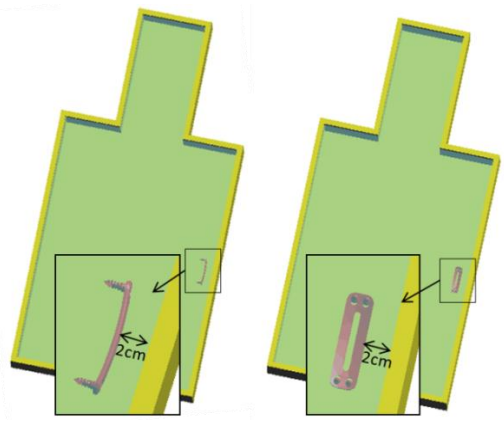

Figure 2-7 The placement of two different orientations: orientation 1 (left) and orientation 2 (right) for the orthopedic implant in the ASTM heating phantom.

2.4 Thermal Simulation

Based on the electromagnetic field distribution obtained from the previous study, the specific absorption rate (SAR) is then calculated using Equation 2-1 [23],

$$SAR(r) = \frac{\sigma(r)}{2\rho(r)} E(r) \cdot E^*(r), \qquad [2\text{-}1]$$

where $\sigma(r)$ is the conductivity ($\mathrm{S/m}$),

$\rho(r)$ is the mass density ($\mathrm{kg/m^3}$),

and $E(r) \cdot E^*(r)$ is the squared magnitude of the induced electric field.

The local SAR is not always useful, since it is too sensitive to approximation in the computational methods. Furthermore, the energy deposited at a point is invariably smeared out due to heat conduction; therefore, single point values are not thermally significant. For these reasons, SAR is mostly presented in an averaged form. The two most commonly used averaged SAR's are whole body SAR (wbSAR) and IEEE/IEC62604 1g averaged SAR [25].

wbSAR: The ratio between total power loss in the entire region of interest divided by the total mass of the entire region of interest. For example, if the entire region of interest is a full human body, the wbSAR is defined in Equation 2-2,

$$\text{wbSAR} = \frac{1}{2M}\int_V \sigma E^2 dv, \qquad [2\text{-}2]$$

where M is the total weight for the human body, and the integration region is the full human body.

IEEE/IEC62704-1 avgSAR: This is defined in the latest standard by IEEE and the International Electrotechnical Commission (IEC). It recommends the region as a cube aligned to the computation grid and sized to contain a specific mass of lossy tissue and at most 10% of the volume filled with background material (i.e., air or other non-conductive tissues). This cube is expanded at each location to compute the average, resulting in a distribution of averaged SAR values along the entire region of interest. Normally, the peak value in this distribution is the object of interest, named IEEE/IEC62704-1 psSAR.

In most cases SAR is not enough to evaluate the electromagnetics safety for implanted medical implants. Thus, the temperature increase which is directly related to heating effect needs to be analyzed. Developed in 1948 by Pennes, the "Bioheat Equation" (PBE) is the most used model for thermal BioEM simulaions [26]. The formula is shown in Equation 2-3,

$$\rho c \frac{\partial T}{\partial t} = \nabla \cdot \left(k \nabla T\right) + \rho Q + \rho S - \rho_b c_b \rho \omega \left(T - T_b\right), \qquad [2\text{-}3]$$

where k is the thermal conductivity, S is the specific absorption rate, ω is the perfusion rate, and Q is the metabolic heat generation rate. ρ is the density of the medium, ρ_b, c_b and T_b are the density, specific heat capacity, and temperature of the blood. In the ASTM

phantom, the equation can be further simplified since there is no metabolic heat generation or heat transfer by blood.

In the ASTM phantom, the heat transfer equation is shown in Equation 2-4,

$$\rho c \frac{\partial T}{\partial t} = \nabla \cdot \left(k \nabla T \right) + \rho SAR, \qquad [2\text{-}4]$$

where ρ, c and k are the density, specific heat capacity, and thermal conductivity. The maximum time step for which stability can be guaranteed is given by Equation 2-5,

$$dt \le \frac{8k}{\rho c \left(dx \right)^2}, \qquad [2\text{-}5]$$

where dt is the thermal simulation time step and dx is the unite mesh size. The above equation is only valid for uniform mesh, for non-uniform mesh, the stable time-step is more complicated.

2.5 ISO/TS 10974 Standard for AIMDs

Determining local tissue temperature rise due to interaction of an AIMD with the RF field of an MRI scanner is a complex process and depends on AIMD design, MRI scanner technology (RF coil and pulse sequence design), patient size, anatomy, position, AIMD location, and tissue properties. Depending on the specific conditions, variation of in vivo temperatures may span several orders of magnitude. For example, a small compact device implanted in an anatomical region that receives minimal RF exposure may pose relatively little RF heating risk, whereas an elongated metallic device, such as a neurostimulator or pacemaker lead, may present an elevated risk. A four tier testing approach is described [27] in order to accommodate the diversity of AIMD

configurations and specific applications and to determine a conservative estimate of energy deposition—including the uncertainty—in a controlled in vitro test system.

2.5.1 Outline of the Four-Tier Approach

Tiers 1 and 2 follow an identical step-by-step measurement procedure but differ in the magnitude of the specified electric test field. Please note that Tiers 1 and 2 are only applicable if the AIMD does not include any concentrated filter (lumped elements) in the elongated part of the AIMD so that the AIMD cannot be modeled using continuous properties per unit length. Tier 1 is the most conservative and computationally simple and it requires no additional electromagnetic modeling. Tiers 2 and 3 provide successively less overestimation of test field magnitudes, justified by electromagnetic computational analysis. Tier 4 provides the least overestimation of test fields, and requires the most stringent electromagnetic computational analysis.

The following steps simply describe the four tier approach:

Tier 1:

Step 1: Determine the incident electric field in the body regions where the AIMD is located. This can be defined simply as determining the highest regional electric field.

Step 2: The AIMD is immersed in a homogeneous simulated tissue medium and exposed to a uniform electric test field (uniform magnitude and uniform phase) at the amplitude equal to the value determined from Step 1. The maximum energy deposited by the AIMD is determined using SAR measurements or temperature measurements.

Step 3: If the electrode leads or similarly elongated structures are longer than 100 mm, the resonant length of the device must be determined by measuring the energy deposition for lengths between 100 mm and the largest commercial length of the elongated AIMD.

Tier 2:

Step 1: Determine the incident field for testing the AIMD for any averaged 10 g tissue for the anatomically relevant implant locations.

Step 2 and 3 are similar to Steps 2 and 3 of Tier 1.

Tier 3:

Step 1: Determine the incident field for the tangential electric field (magnitude and phase) and the magnetic field averaged over any 20 mm of anatomically relevant elongated AIMD path (this only applies for structures with length-to-diameter ratio of greater than 10) for the anatomically relevant implant locations. Determine the uncertainty of the determined incident test field.

Step 2: Immerse the AIMD in constant phase of the incident electric field with the same magnitude distribution determined in step 1. The maximum energy deposited by the AIMD is determined using SAR measurements or temperature measurements.

Step 3: Similar to Step 2 for Tier 1.

Tier 4:

Step 1: Develop and validate an electromagnetic model (full-wave or lumped element) of the AIMD being evaluated. The AIMD model is validated by demonstrating the equivalence of the model and experimental results.

Step 2: Compute the energy deposition normalized to the appropriate incident field, e.g., B_1, normal mode, etc., using the validated numerical AIMD model for the defined patient population considering all relevant parameters.

Step 3: Determine the uncertainty budget of the evaluation. This will include measurement, computational, and patient population coverage uncertainty.

Step 4: Compute the maximum tissue temperature rise for the energy deposition.

Figure 2-8 shows the flow graph for the four-tier approach.

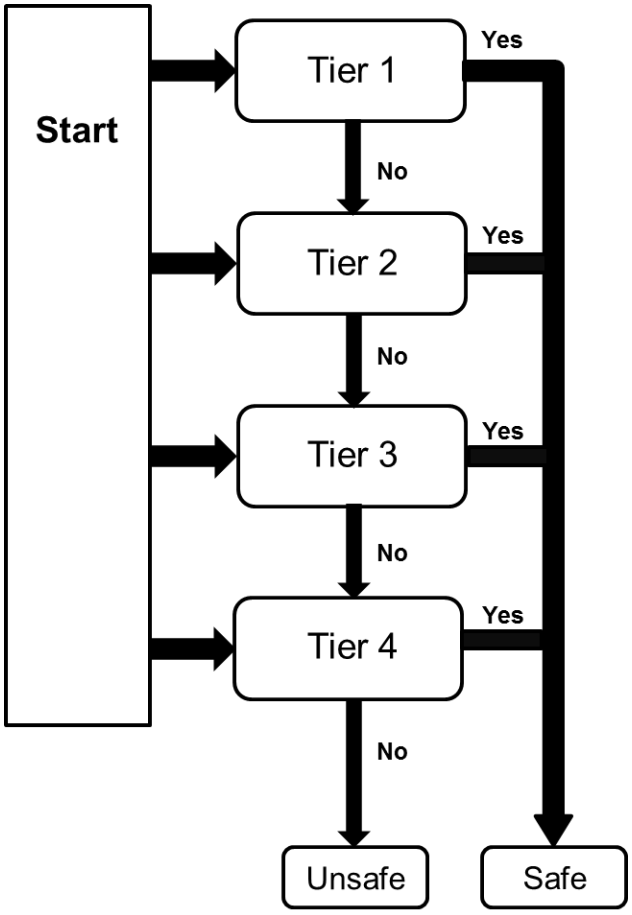

Figure 2-8 General Procedure to evaluate AIMD MRI Safety using four-tier approach.

2.6 Measurement in MRI RF Environment

The numerical simulation method for the MRI RF Coil and medical device is introduced in the previous sections. Another important aspect is the measurement for temperature rise around the devices in the RF coil. In the following sections, phantom preparation, device configuration in ASTM phantom, and RF coil and control system operation will be introduced.

2.6.1 Phantom preparation

As is mentioned in ASTM F2182-11a [4], the measurement of RF-induced heating requires the implant to be placed in a phantom that simulates the electrical and thermal properties of the human body. The gelled saline which consists of sodium chloride and polyacrylic acid is made to meet the criteria for the purpose of simulating human tissue. The conductivity of the gelled saline shall be 0.47 $\pm$ 10% S/m at room temperature. The heat capacity is around 4150 $J \cdot Kg^{-1} \cdot K^{-1}$ and the relative electric permittivity shall be 80 $\pm$ 20 at the test frequency (64 MHz or 128 MHz). The recipe for the gelled saline is NaCl and polyacrylic acid (PAA) as described in the standard. NaCl with over 99% pure reagent grade is obtained from The Science Company, Denver, CO. Polyacrylic acid is obtained from Aldrich Chemical Company, Inc., Milwaukee, WI. The procedure for preparing PAA gelled saline is to 1) Add NaCl to water and make sure the concentration of NaCl is 1.32 g/L. Stir completely and then measure the conductivity. The conductivity should be in the range of 0.26 $\pm$ 10 % at this time. If the conductivity is less than the minimum limit of the desired value, add NaCl slowly and stir to make sure the conductivity meets the requirement. This step is necessary and important to make sure the prepared gelled saline has a final conductivity of 0.47 S/m. 2) Add PAA to a

concentration of 10 g/L and stir to suspend completely. This step might take 5 to 10 minutes until the liquid becomes a suspension. 3) After one hour, blend the suspension into slurry. A kitchen mixer is used in this step. During the 20 minutes blending, the mixer head needs to be immersed totally into the suspension to avoid bubbles. The slurry will be ready to use after 24 hours. The prepared gelled saline is shown in Figure 2-9. It has little bubbles inside and is semi-transparent with a conductivity of 0.448 S/m which meet the criteria. The concentration for PAA and NaCl is critical for preparing ASTM phantom. A gelled phantom with low thermal conductivity is required for temperature measurement in order to obtain a stable result [28].

Figure 2-9 ASTM Phantom after preparation.

According to the standard, all implants need to be tested in worst case configuration and orientation that would produce the largest heating in the phantom. However, this could be very difficult during measurement when various medical devices with different shapes and dimensions are presented. Both numerical simulation and measurement [29] show that measured temperature data is very sensitive to the position

of the temperature probe. This means a little shift of the probe position during the measurement could result in large measurement error. A preferred method to determine the worst case heating configuration for the device is to use numerical simulation to evaluate several device configurations which are able to represent all the clinical possible configurations. This combined modeling and experimental approach can quickly identify the worst-case heating for an entire implant family. The approach will be further discussed in Chapter 3.

2.6.2 RF Coil and control system operation

The RF coil and control system used in the measurement is the MITS 1.5 system from Zurich Med Tech. It is designed to simulate incident RF fields with user-defined modulation and time sequences as generated by commercial 1.5 Tesla magnetic resonance scanners. Figure 2-10 shows the 1.5 T MRI RF coil (left) and the control system (right).

Figure 2-10 1.5Tesla/64MHz MRI RF Coil with Shied (Left); MITS 1.5 control system (Right).

By adjusting the initial input parameters on the MITS1.5 system, pulse shape as well as the field polarization can be obtained inside the RF coil. Typical pulse shape used in the MITS1.5 system is $\mathrm{sinc}(2\pi)$ wave form. A circular polarized field is formed by using IQ feed as shown in Figure 2-11, where the phase difference between Feed I and Feed Q is 90^{o}.

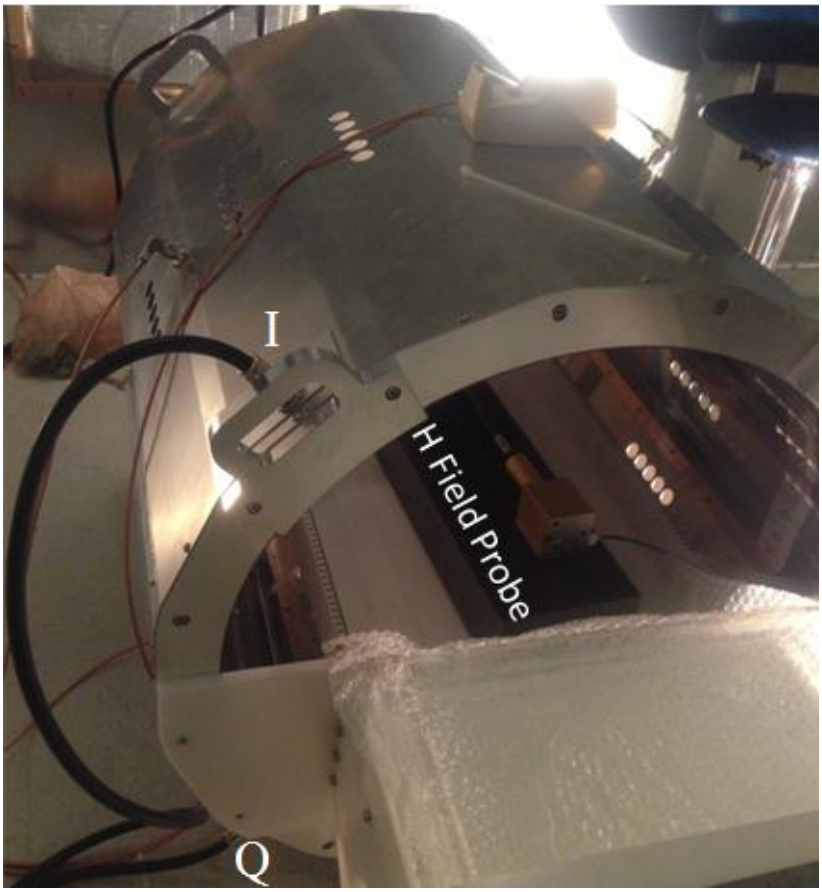

Figure 2-11 IQ feed for RF coil and H field probe.

2.6.3 Thermal measurement

Fiber optic temperature probes (Neoptix) are used to monitor the real time temperature rise around the device. Figure 2-12 shows the Neoptix™ Reflex™

thermometer that has four channels which enable multiple temperature measurement simultaneously. The fiber optic T2^{TM} probe consists of a 300-micron O.D. solid-state sensitive element bonded to an optical fiber. The fiber is covered with a 1.06 mm O.D. oil-permeable protective PTFE Teflon sheath. The entire probe is protected by a 3.1 mm O.D. PTFE “spiral wrap” reinforcement. Only chemically resistant and low dielectric constant materials are used for these temperature probes. This temperature probe complies with ASTM D2413 and D149 standards [30][31]. During the measurement, the measurement end of the probe is attached to the medical device. The real-time visualization of the temperature can be directly displayed and saved on the PC.

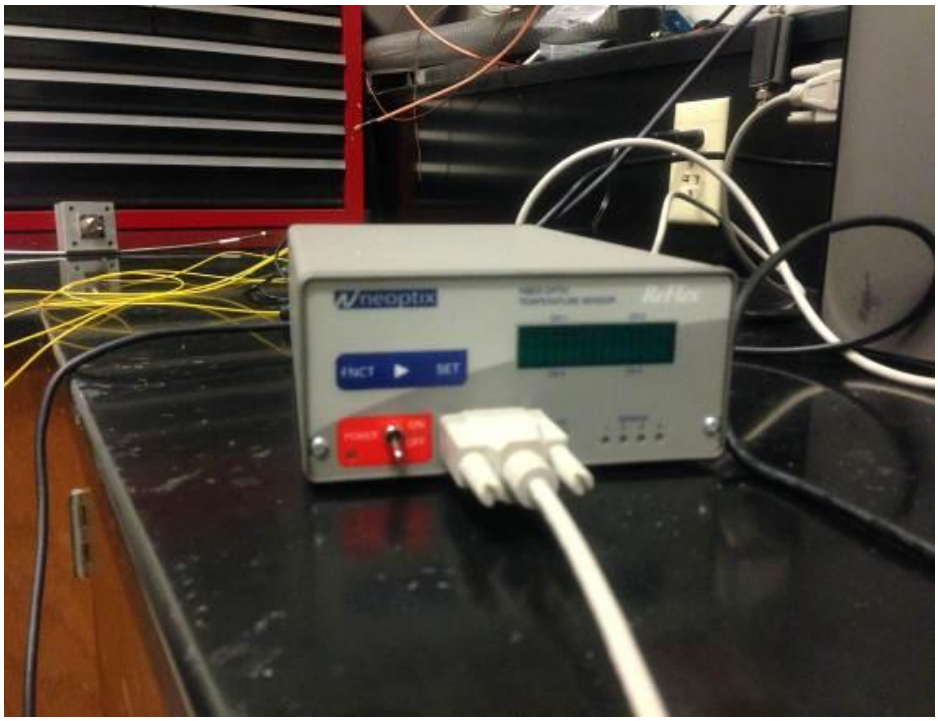

Figure 2-12 Neoptix temperature.

Chapter 3 MRI RF Effect for Passive Devices

Orthopedic devices are medical devices used to replace or provide fixation of bone or to replace articulating surfaces of a joint. In simpler words, orthopedic implants are used to replace damaged or troubled joints. Most orthopedic implants and materials do not pose problems for patients undergoing MR procedures. However, because of the length of the implant or the formation of a conductive loop, MR examinations may be hazardous for certain orthopedic implants [32][33][34]. In the ASTM F2182 standard, the test method assumes that testing is done on devices that will be entirely inside the body. However, there are other implantation conditions where the devices are not entirely inside the body. For example, external fixation devices which are used to keep fractured bones stabilized and in alignment are attached to the screws from outside the skin and can be adjusted externally to ensure the bones remain in an optimal position during the healing process. The major parts of external fixation devices are outside the human body. Also, percutaneous needles, catheters such as RF ablation probes, and microwave ablation probes are all devices used to insert from outside the body. These devices might potentially result in a higher RF heating due to the higher electric field intensity outside the human body [35]. In this chapter, the RF heating for passive medical devices will be discussed. In the first part, the RF heating for spinal cord implanted devices will be studied both numerically and experimentally. In the second part, studies will be extended to the RF heating for external fixation devices.

3.1 Implanted Passive Medical Device

Based on the numerical procedure described in previous sections, a set of electromagnetic simulations were performed for both 1.5 T/64-MHz and 3-Tesla/128-MHz transmit RF coil conditions. In all electromagnetic simulations, the results were normalized to an input power of 1W. However, the results can be easily normalized to 2W/Kg and 4W/Kg [36] which correspond to normal mode and first level control mode for MRI machine, respectively.

3.1.1 Simulation Study

The normalized SAR distributions inside the ASTM phantom are shown in Figure 3-1. To remove potential numerical errors, the 1g averaged SAR distributions are also shown, in addition to the un-averaged peak SAR distributions. In general, the global views of these two SAR distributions have a similar pattern. The zoomed views of the local SAR distributions near the implants are shown in Figure 3-2. The small green squares in the figure indicate the maximum SAR location. As indicated in the figure, the local peak SAR distribution and the 1 g averaged distribution can be different although both indicate that the maximum SAR values (corresponding to maximum heating) occur at the end of the device. However, this is not necessarily the case when the length of the orthopedic implants increases to 6.7 cm as shown in Figure 3-3. As indicated in Figure 3-3, the maximum peak SAR is located at the tip of a screw while the maximum 1 g averaged SAR is located at the top of the implant. Since the temperature rise is a diffusion process [26], the maximum temperature is more likely located close to the location where the maximum 1 g averaged SAR is observed. In order to clearly identify the maximum heating position, thermal simulations are necessary.

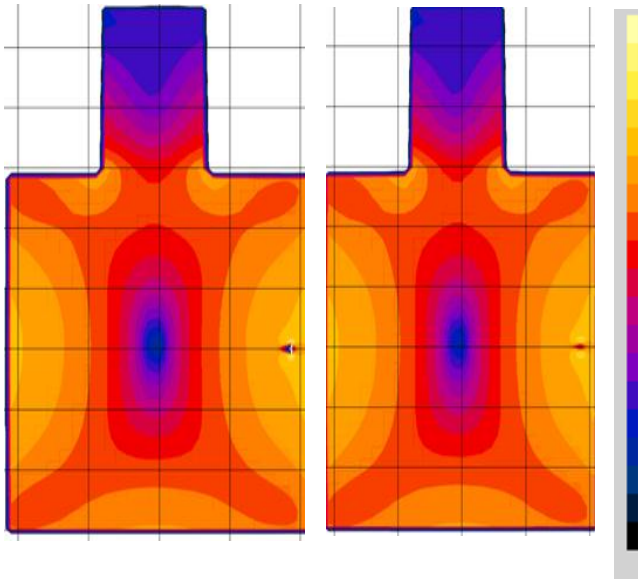

Figure 3-1 SAR distribution within the ASTM heating phantom. Left: peak level SAR distribution. Right: 1g averaged SAR distribution.

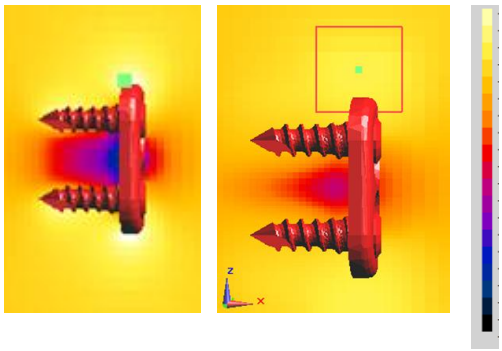

Figure 3-2 Zoomed view of the SAR distribution near the implants with 2.1 cm length. The green spots indicate the maximum SAR location. Left: peak SAR distribution. Right: 1g averaged SAR distribution.

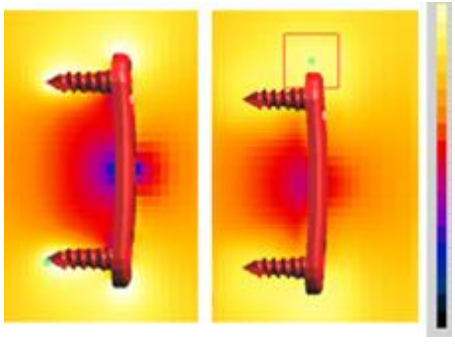

Figure 3-3 Zoomed view of the SAR distribution near the implants with 6.7 cm length. The green spots indicate the maximum SAR location. Left: peak SAR distribution. Right: 1g averaged SAR distribution.

Table 3-1 shows the maximum peak SAR and the 1 g averaged SAR for the orthopedic implant at different lengths. For this implant, the SAR increases as its length increases. The maximum heating locations are expected around either the ends of the implant or the tips of the screws.

The SAR distribution within the ASTM phantom for the same implant was investigated at 3-T/128-MHz for all different lengths. The results of this study are tabulated in Table 3-2. As the length of the implant increases, the SAR also increases. However, for this particular placement, the SAR value at 1.5-T/64-MHz near the implant was higher than those at 3-T/128-MHz. Since 3T/128-MHz systems are operating at a higher frequency compared to 1.5-T/64-MHs scanners for implants that may be implanted “deeper” in the body, more energy loss can be expected along the path from the surface of the ASTM phantom to the implant. Therefore, the incident electric field onto the implant at 3-T/128-MHz could be lower.

Table 3-1 The maximum peak SAR and 1g averaged SAR for the device at different lengths (1.5-T/64-MHz transmit RF coil)

Length of Model (mm)	Peak SAR (W/Kg)		Peak 1g Averaged SAR (W/Kg)	
	Orientation1	Orientation2	Orientation1	Orientation2
Without Device	0.08		0.08	
21	0.90	0.90	0.13	0.13
23	0.92	0.93	0.13	0.14
25	0.99	0.99	0.14	0.15
27	1.05	1.14	0.15	0.16
30	1.21	1.18	0.17	0.17
32	1.44	1.38	0.18	0.19
37	1.61	1.73	0.21	0.22
41	1.87	1.87	0.24	0.24
43	2.00	1.96	0.25	0.25
45	2.16	2.14	0.26	0.26
47	2.43	2.34	0.28	0.27
50	2.64	2.77	0.28	0.31
62	4.04	3.93	0.39	0.40
67	4.51	4.64	0.39	0.41
87	7.17	7.67	0.55	0.58
107	9.70	10.30	0.69	0.75

Table 3-2 The maximum peak SAR and 1g averaged SAR for the device at different lengths (3-T/128-MHz transmit RF coil)

Length of Model (mm)	Peak SAR (W/Kg)		Peak 1g Averaged SAR (W/Kg)	
	Orientation1	Orientation2	Orientation1	Orientation2
Without Device	0.05		0.03	
21	0.33	0.34	0.05	0.05
23	0.35	0.37	0.05	0.05
25	0.38	0.38	0.05	0.06
27	0.41	0.43	0.06	0.06
30	0.48	0.51	0.07	0.07
32	0.59	0.58	0.07	0.08
37	0.70	0.71	0.09	0.09
41	0.88	0.89	0.10	0.10
43	0.94	0.98	0.10	0.11
45	1.05	1.08	0.11	0.12
47	1.20	1.15	0.12	0.12
50	1.39	1.38	0.13	0.14
62	2.14	2.06	0.18	0.18
67	2.44	2.43	0.18	0.19
87	3.48	3.55	0.23	0.24
107	3.68	3.70	0.24	0.24

In Figure 3-4 and Figure 3-5, the maximum local SAR as a function of implant length at 1.5-T/64-MHz and 3-T/128-MHz is displayed. As indicated in the figures, peak SAR and 1g averaged SAR for both implant orientations are similar. They both increase as the implant length increases.

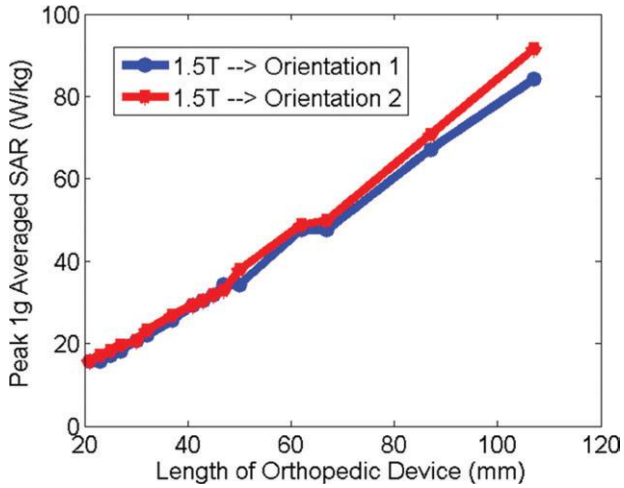

Figure 3-4 Peak 1g averaged SAR values as a function of implant length for two different orientations at 1.5 T/64-MHz.

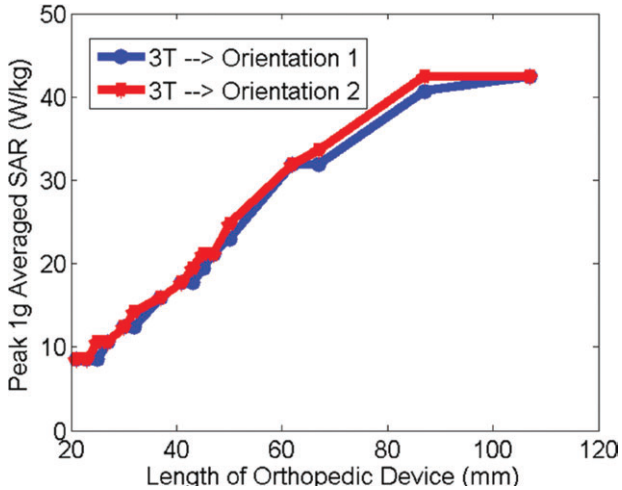

Figure 3-5 Peak 1g averaged SAR values as a function of implant length for two different orientations at 3-T/128-MHz.

For the same level of input power at 3-T/128-MHz, the SAR is lower near the tip region, indicating that possible lower heating for 3-T/128-MHz will be less for this setup

in this study. Figure 3-5 shows that the SAR values for this device at 3-T/128-MHz seem to reach a plateau near 10 cm in implant length. This could be explained as the resonant wavelength effect. When the implant is longer than 10 cm, the length is less than half the wavelength at 3-T/128-MHz inside the gelled-saline. For such scenarios, the maximum heating locations will probably be close to the ends of the implants. However, as the length increases, the implant's dimensions can become comparable to the wavelength of the incident electromagnetic field. Due to the resonant effects as well as the phase variation of the incident field along the implant, the potential heating will no longer have the monotonic increment trend. These simulations were not performed because this particular implant does not exist longer than 107-mm. The input power for cases shown here is at 1W for illustration purposes. These results need to be scaled based on local SAR values for future temperature rise evaluations.

The maximum averaged SAR location near the implanted device is a good indication of where the maximum temperature rise may occur. To obtain the actual temperature rise, thermal simulations need to be carried out. This can be achieved by performing additional thermal simulations based on the bio-heat equation [37][38]. To determine the temperature rise as a function of time, thermal sensors are placed near the locations on the implant where the maximum temperature rises are expected. Before starting the thermal simulations, all SAR values will be scaled. For example, to determine the SAR values near the implant when the whole-body averaged SAR is 2W/kg, it is necessary to calculate the total energy loss within the phantom and then scale it to the total weight of the phantom.

As in the previous 1.5-T/64-MHz electromagnetic simulations, it is observed that when the input power from the RF coil is at 1 W, the total energy loss inside the ASTM phantom is at 0.735W. With the weight of the ASTM phantom at 44.86 Kg, the whole body averaged SAR for the ASTM phantom is at 0.016W/kg. For the MR system operating normal mode, the whole body averaged SAR is limited to 2W/kg (include the reference on operating mode). Therefore, a scaling factor of 122 (2W/kg / 0.016W/kg) should be applied to previous SAR values. Using this scaled SAR value, thermal simulations were then carried out for the whole body-averaged SAR at 2W/kg. Another way to perform the scaling is to use local SAR. This requires one additional measurement of local SAR value using a titanium rod [39]. All results will then be normalized using this value [40].

3.1.2 Measurement Study

Carefully designed temperature measurements are carried out for both 1.5-T/64-MHz and 3-T/128-MHz MR systems. As indicated in Figure 3-6, the temperature probes were placed near the locations where maximum temperature rise was expected according to our simulation results.

Figure 3-7 shows the simulated and measured temperature rise over time for 15 minutes at the two temperature probe locations as a function of time for 1.5-T/64-MHz conditions. As indicated in Figure 16, the measurement and simulation results agree well with each other.

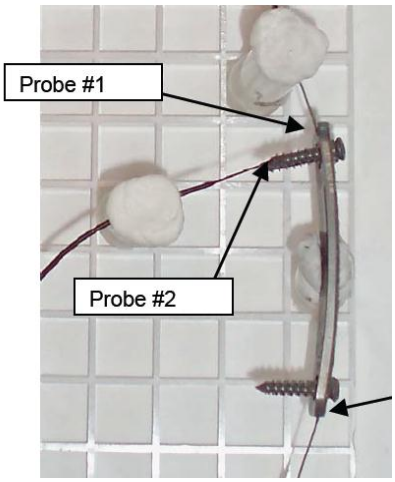

Figure 3-6 Positions for the fluoroptic thermometry probes, #1 and #2, relative to the orthopedic implant, Basis Spinal System.

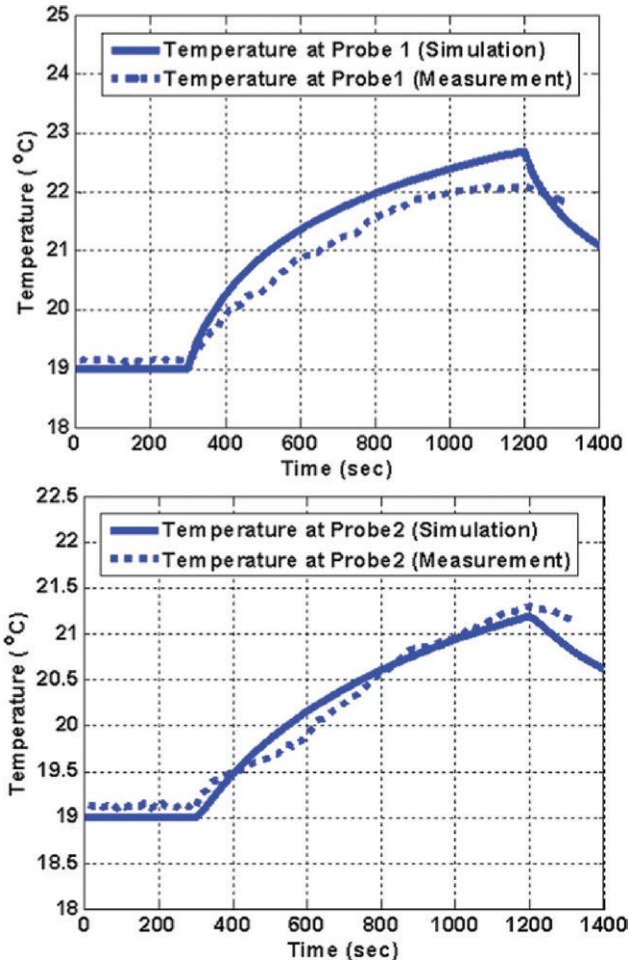

Figure 3-7 Simulated and measured temperature rises at temperature Probe 1 (Top) and Probe 2 (Bottom) for 1.5-T/64-MHz MRI system.

Similarly, the temperature rise simulations were performed for the 3-T/128-MHz system based on the results obtained from the electromagnetic simulation. Table 3-3 shows the temperature rise after 15 minutes for both 1.5-T/64-MHZ and 3-T/128-MHz at the probe location obtained by the simulation and measurement. As clearly indicated in Table 3-3, a good correlation is observed.

Table 3-3 Simulated and measured temperature changes for 1.5-T/64-MHz and 3-T/128-MHz MR systems after 15 minutes of RF exposure at the two temperature probe locations

	Simulation 1.5 T	**Measurement 1.5 T**	**Simulation 3 T**	**Measurement 3 T**
Probe 1	3.6 ºC	3.1 ºC	2.1 ºC	1.9 ºC
Probe 2	2.2 ºC	2.2 ºC	1.6 ºC	1.7 ºC

3.1.3 Discussion

From the electromagnetic and thermal simulation results, it can be clearly seen that numerical techniques were able to provide a good assessment of the maximum heating location for the evaluated orthopedic implant tested. For this particular orthopedic implant, the maximum heating locations were close to the tips of the screws and the ends of the implant. As the length of these orthopedic implant increases, especially when the device length is comparable to the wavelength of the MR operating frequencies, the heating patterns as well as the maximum heating location appear to be device-dependent.

From this study, the findings suggest that, when the orthopedic implant's length is less than 100 mm, the maximum heating of the device is almost linearly proportional to its length. This can be explained as a wavelength effect. At 1.5T the electromagnetic incident wavelength is ~4.5 m in free space and ~0.52 m in the gelled saline. When this

orthopedic implant's length is less than 100 mm, the overall length is still less than a quarter wavelength. Therefore, it is not expected for the incident field to have a large phase variation or have a resonant effect. However, for 3T electromagnetic signals, the wavelength in gelled saline is 0.26 m. The device length of 100 mm is approaching the half-wavelength resonant dimension. Therefore, the incident field will have a large phase variation along the device, and the device will exhibit resonant behavior. Thus, a monotonic relationship between the maximum heating and the device length will no longer be valid. For device lengths over 100 mm, an electromagnetic/thermal simulation is recommended to be performed at centimeter increments to capture the maximum heating for different lengths.

This investigation demonstrated that with numerical calculations it is possible to quickly predict which device configuration and size will lead to maximum heating as well as the maximum heating location for the device. With this information, one can correctly place the temperature probe, as well as the number of devices that need to be tested. Consequently, it can significantly reduce the time and expense of testing performed to evaluate MRI-related heating. Using this testing procedure, one can quickly predict the worst-case heating of a device family.

In conclusion, electromagnetic and thermal simulations were used to determine the worst-case heating for an orthopedic implant with lengths of from 21-107 mm. For this particular implant family, it was observed that the temperature rise is related to the length of the implant, and the maximum temperature rise locations are close to the ends of the implant or at the screw tip. MRI-related heating experiments were performed to record temperatures to validate the simulation results, and good correlations were

observed. The findings demonstrated that electromagnetic and thermal simulations may be used as an excellent tool to provide the heating pattern for implants and to identify the maximum heating locations for the entire device family. If only a measurement technique is used, temperature probes need to be placed near the entire device to determine the worst-case heating spot near the device. Therefore, numerical modeling is an accurate and efficient way to determine the worst-case heating.

Because the maximum heating can change for different implant sizes or configurations, the location of the maximum heating is important for a proper measurement setup. Numerical simulations provide the means to drastically reduce the number of measurements needed to assess the worst-case configuration and size for an entire device family. The numerical results are also the only practical way to find the location of the maximum heating on the implant surface and to place the temperature probe at this position during the measurements. Importantly, for validation purposes, the numerical simulations should always be accompanied by proper temperature measurements.

3.2 External Fixation Device

In this section the MRI safety of external fixation devices will be discussed. An external fixation device is usually used to keep fractured bones stabilized and in alignment. And the device can be adjusted externally to ensure the bones remain in an optimal position during the healing process [41]. In orthopedic surgeries, the exact construct of an external fixation device needs to be adjusted to fit shapes and sizes of patient populations. A typical device is composed of bars, pins, and clamps. A generic model of the external fixation device is shown in Figure 3-8. Often, large body sizes

require large pin spacing as well as deep pin insertion depth to achieve a good fixation or alignment. As a result, different patients may have different device configurations. Therefore, the effect of different insertion depth and pin spacing on device tip heating shall be investigated. In addition, the electromagnetic properties of the connecting bar between the clamps may also affect the heating. In most practices, the connecting bars are made of metal to retain mechanical strength. Recently, other materials, such as carbon-fiber and plastic glass have been proposed and tested for improving mechanical strength [42]. In this work, a comprehensive study of the effect of bar material will also be performed to understand the heating mechanism.

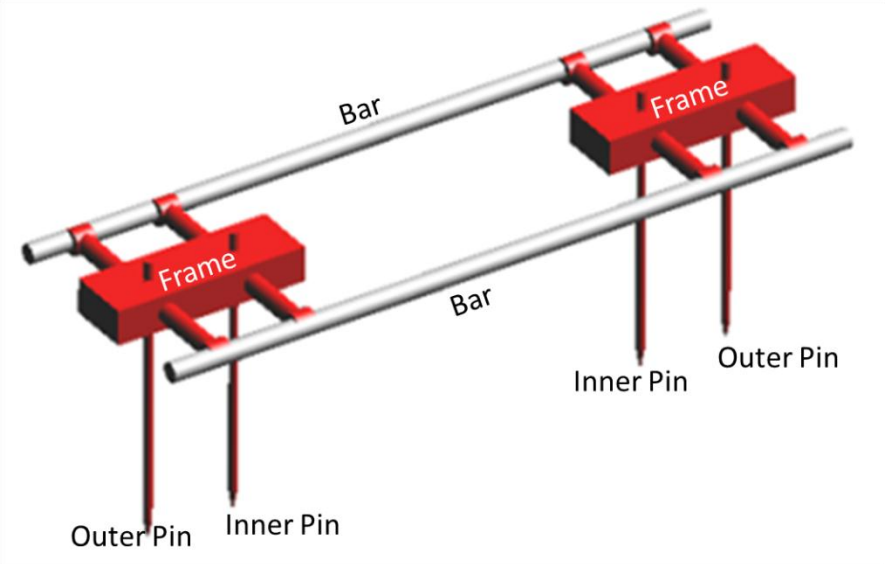

Figure 3-8 Generic external fixation system model.

3.2.1 Insertion Depth, Clamp Spacing, Bar Material Effect on RF Heating

According to the ASTM standard, implanted devices need to be placed at the locations with maximal exposure electric fields in order to minimize the measurement

uncertainty relative to MRI-related heating. In our study, the device pins will be placed at these locations [43].

The external fixation device model used in this study consists of three parts as shown in Figure 3-8. These three parts are: two metallic blocks to represent the clamps, two connectors or bars to represent the rods outside the body for rigid support, and four parallel long pins which are screwed into the bones during surgery. The metallic block has the dimension of 11.4 cm by 2 cm by 3.75 cm. The pin has a diameter of 0.5 cm and length of 16 cm. The connecting bar has a diameter of 1.1 cm and has four different lengths of 31.5 cm, 36.5 cm, 41.5 cm, and 46.5 cm. When different bar lengths are used, the clamp spacing will be changed to 15 cm, 20 cm, 25 cm, and 30 cm. In all the studies, the distance between the two connecting bars is 5 cm.

The simulations were repeated with four different device pins with insertion depths at 2 cm, 5 cm, 8 cm, and 11 cm. Different setups for the simulations are summarized in Table 3-4. With deep pin insertion, the spacing between the connecting bar and the surface of the ASTM gel will be reduced as shown in Figure 3-17. There is a 2 cm space between the pins and the inner side wall of the ASTM phantom. The three different bar materials used in this study are 1) carbon-fiber with a relative dielectric constant of $\varepsilon r = 10$ and electric conductivity of $\sigma = 5.7e6$ S/m, 2) plastic glass with a relative dielectric constant of $\varepsilon r = 4.4$ and conductivity of $\sigma = 0$ S/m and 3) a perfect electric conductor (PEC) bar. The ASTM phantom consists of a plastic box which has a relative dielectric constant of 3.7 and electric conductivity of 0 S/m. The gelled-saline has a relative dielectric constant of $\varepsilon r = 80.38$ and conductivity of $\sigma = 0.448$ S/m. The pins and main blocks of the device are modeled as a perfect electric conductor.

Table 3-4 Electrical and thermal properties for different materials used in simulations

	Permittivity	Electrical Conductivity (S/m)	Thermal Conductivity (W/m/K)	Heat Capacity (J/kg/K)	Density (kg/m^3)
ASTM Phantom GEL	80.38	0.448	0.42	4160	1000
ASTM Phantom Shell	3.7	0	0.2	1000	1000
Device Bar (carbonfiber)	10	5600000	7	400	1000
Device Bar (PEC)	\	\	7	400	8000
Device Bar (plastic glass)	1	4.4	0.2	1000	1000
Device Other Parts(PEC)	\	\	7	400	8000

Table 3-5 Device configurations and bar materials used in simulation study

Device Configuration ID	Clamp Spacing (cm)	Insertion Depth (cm)	Bar Material
1	15	2	Carbon Fiber/PEC/Plastic Glass
2	15	5	Carbon Fiber/PEC/Plastic Glass
3	15	8	Carbon Fiber/PEC/Plastic Glass
4	15	11	Carbon Fiber/PEC/Plastic Glass
5	20	2	Carbon Fiber/PEC/Plastic Glass
6	20	5	Carbon Fiber/PEC/Plastic Glass
7	20	8	Carbon Fiber/PEC/Plastic Glass
8	20	11	Carbon Fiber/PEC/Plastic Glass
9	25	2	Carbon Fiber/PEC/Plastic Glass
10	25	5	Carbon Fiber/PEC/Plastic Glass
11	25	8	Carbon Fiber/PEC/Plastic Glass
12	25	11	Carbon Fiber/PEC/Plastic Glass
13	30	2	Carbon Fiber/PEC/Plastic Glass
14	30	5	Carbon Fiber/PEC/Plastic Glass
15	30	8	Carbon Fiber/PEC/Plastic Glass
16	30	11	Carbon Fiber/PEC/Plastic Glass

Electromagnetic simulations are first conducted to determine electric energy deposition near the pins of the devices. Then, thermal simulations are carried out to estimate the temperature rise near the tips. Based on the energy deposition near the device tips, the temperature rise in the ASTM phantom is calculated using the heat transfer equation given in Equation 3-1,

$$\rho c \frac{\partial T}{\partial t} = \nabla \cdot \left(k \nabla T \right) + \sigma \left| E \right|^2, \qquad [3\text{-}1]$$

where ρ is the gel density which is 1000 kg/m^3 in the simulation, and c is the specific heat. The thermal conductivity k for the ASTM plastic box, the ASTM gelled-saline, and the device are 0.2 $W \cdot m^{-1} \cdot K^{-1}$, 0.42 $W \cdot m^{-1} \cdot K^{-1}$, and 7 $W \cdot m^{-1} \cdot K^{-1}$, respectively. The specific heat capacity for gelled-saline is 4160 $J \cdot Kg^{-1} \cdot K^{-1}$. For the plastic box and device, the specific heat capacity is 1000 $J \cdot Kg^{-1} \cdot K^{-1}$. The electric and thermal properties of the materials in this study are listed in Table 3-5.

The ASTM standard requires an RF field producing a sufficient whole body-averaged SAR at 2 W/Kg for approximately 15 minutes for temperature rise measurement [4]. Thus, in all following discussions for both 1.5-Tesla and 3-Tesla RF coils, the whole-body (WB) averaged SAR of 2 W/Kg is used to normalize the results. The WB averaged SAR is defined by the total absorbed power of the phantom gel divided by the total mass of the phantom gel.

In Figure 3-9 to Figure 3-14, the maximum 1g averaged SAR in the ASTM phantom and the temperature rises near the device pins are shown for both 1.5-T and 3-T MRI systems. The temperature rise data are recorded for 15 minutes of MRI RF scan time. The results are listed in six groups with different bar materials and MRI systems. In each group, e.g., 1.5-T MRI environment and bar material as carbon-fiber, the 1g averaged SAR and temperature rise data are shown with different clamp spacing (15 cm, 20 cm, 25 cm, and 30 cm). And the four different curves in the plot represent four different insertion depth values: 2 cm, 5 cm, 8 cm, and 11 cm, respectively.

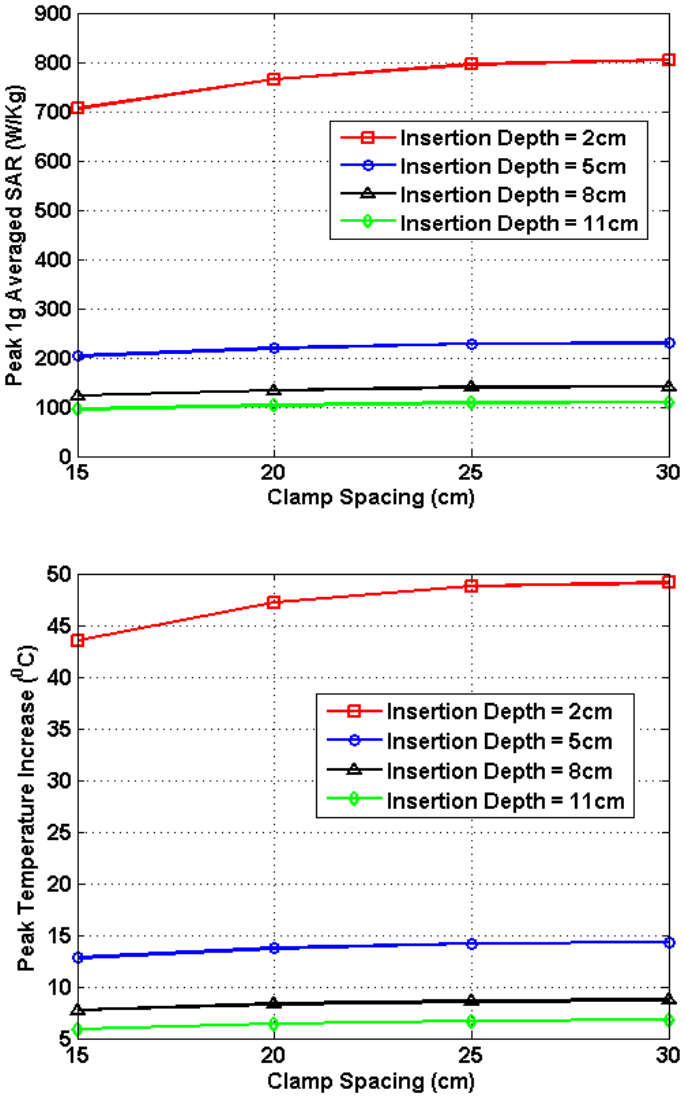

Figure 3-9 Peak 1g Averaged SAR (Top) and maximum temperature rise after 15 min MRI scan (Bottom) for PEC bar in 1.5T MRI.

In the results shown in Figure 3-9 to Figure 3-14, all peak 1g averaged SAR results correlate very well with the temperature rise results since the temperature rise is related to power deposition inside the ASTM phantom. Higher peak-averaged SAR value means higher local power loss around the pin. This will result in higher surface heating from the device pin, and a larger temperature rise can be obtained.

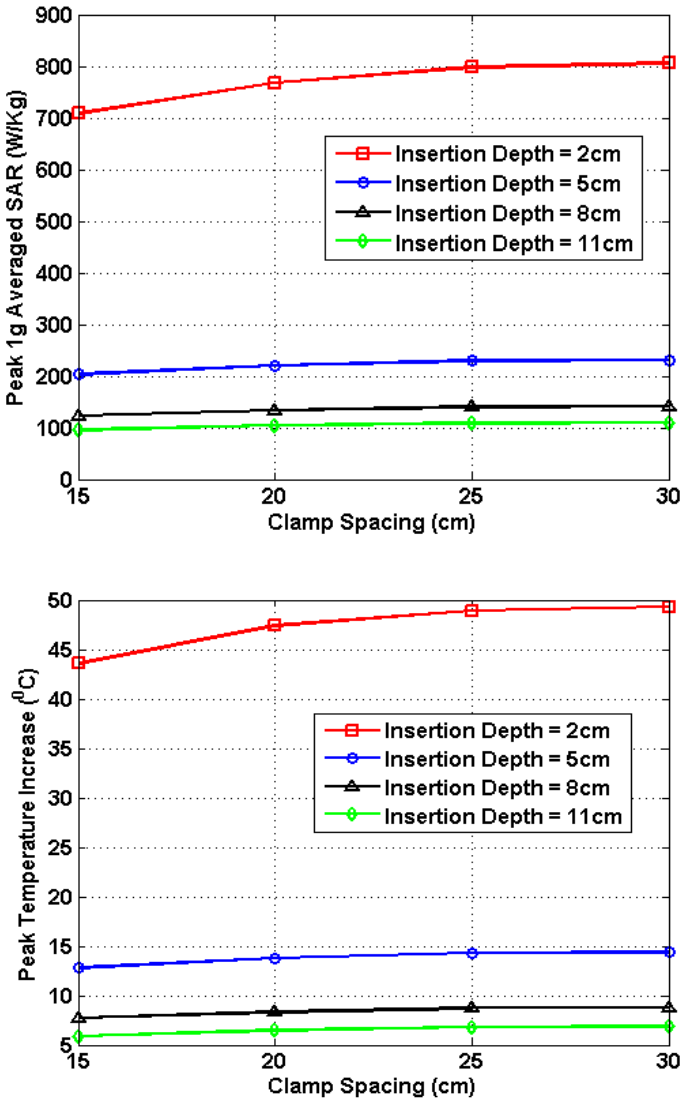

Figure 3-10 Peak 1g Averaged SAR (Top) and maximum temperature rise after 1 5min MRI scan (Bottom) for carbon fiber bar in 1.5T MRI.

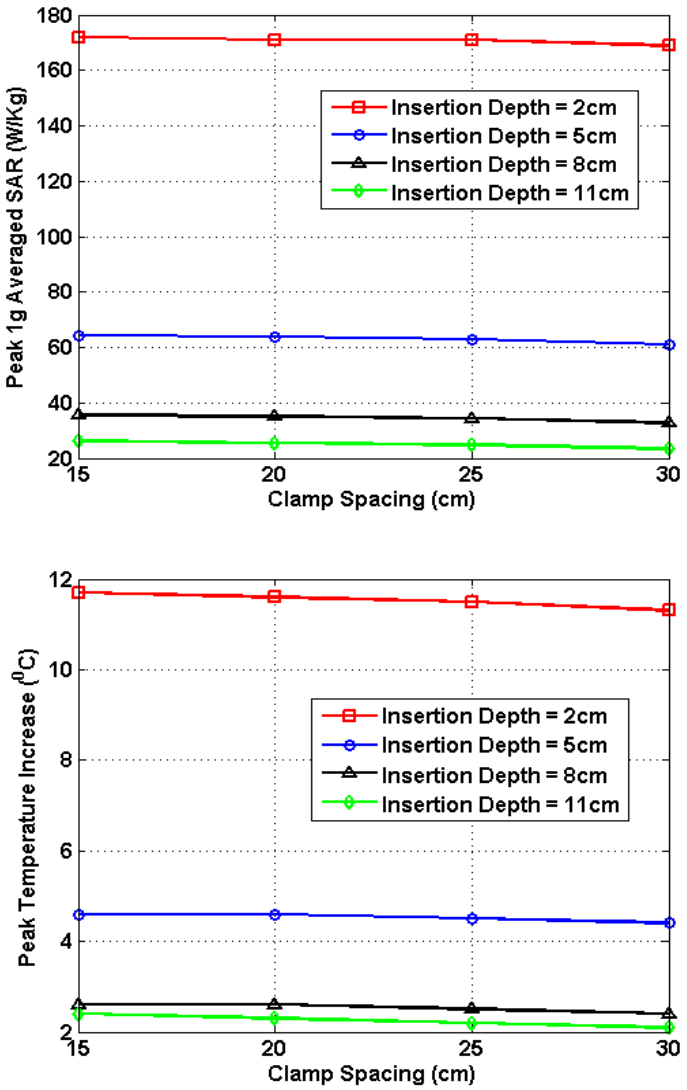

Figure 3-11 Peak 1g Averaged SAR (Top) and maximum temperature rise after 15 min MRI scan (Bottom) for plastic glass bar in 1.5T MRI.

In the 1.5-T MRI system, when the device bar is made of carbon fiber, as the insertion depth increases the temperature rise decreases dramatically. When clamp spacing increases, the temperature rise increases slightly. When the device bar is made of PEC, the temperature rise has a very similar trend and similar value as those for the carbon fiber bar. Therefore, in the 1.5 Tesla MRI coil the carbon fiber device bar can be modeled as PEC to simplify modeling. In Figure 3-11, the bottom figure shows the

temperature rise results using plastic glass bars. Structures with plastic glass bars have much less heating than those devices with the carbon fiber bar and PEC bar in the 1.5 Tesla MRI coil since the plastic glass bars are electrical insulators. Such insulators will not induce additional energy deposition to the pins of the external fixation devices.

In the 3-T MRI, the temperature rise turns out to be much less than in the 1.5-T MRI for the specific configurations studied here. For example, the worst-case temperature rise (30 cm pin spacing and 2 cm insertion depth) after a 15 minute MRI scan is 11 degrees in the 3-T MRI compared with 59 degrees in the 1.5-T MRI. Similarly, for the 3-T MRI system, the PEC bar is also a good approximation for a carbon fiber bar. Both of them have very similar heating results. It is also found that, in the 3-T MRI, when the insertion depth increases, the temperature rise no longer keeps on decreasing. The heating for a 2 cm insert depth structure is higher than the other three insertion depths. However, temperature rises for 5 cm, 8 cm, and 11 cm inserting depth structures are comparable to each other. Increasing of clamp spacing does not contribute to the small increment of RF heating as noticed in 1.5 T RF coil. The most possible reason is the wavelength effect. In 3 T RF coil, the resonance frequency is around 128 MHz which is twice as high as the 64 MHz resonance frequency in 1.5 T RF coil. The wavelength of the RF field for 3 T MRI is then around 26 cm. Therefore, the clamp spacing is comparable to the wavelength in 3 T MRI which indicates a RF field with more than 180^{o} phase different along the device frame. And the phase cancellation along the device frame is considered the main reason that causes a temperature fluctuation as the clamp spacing increases.

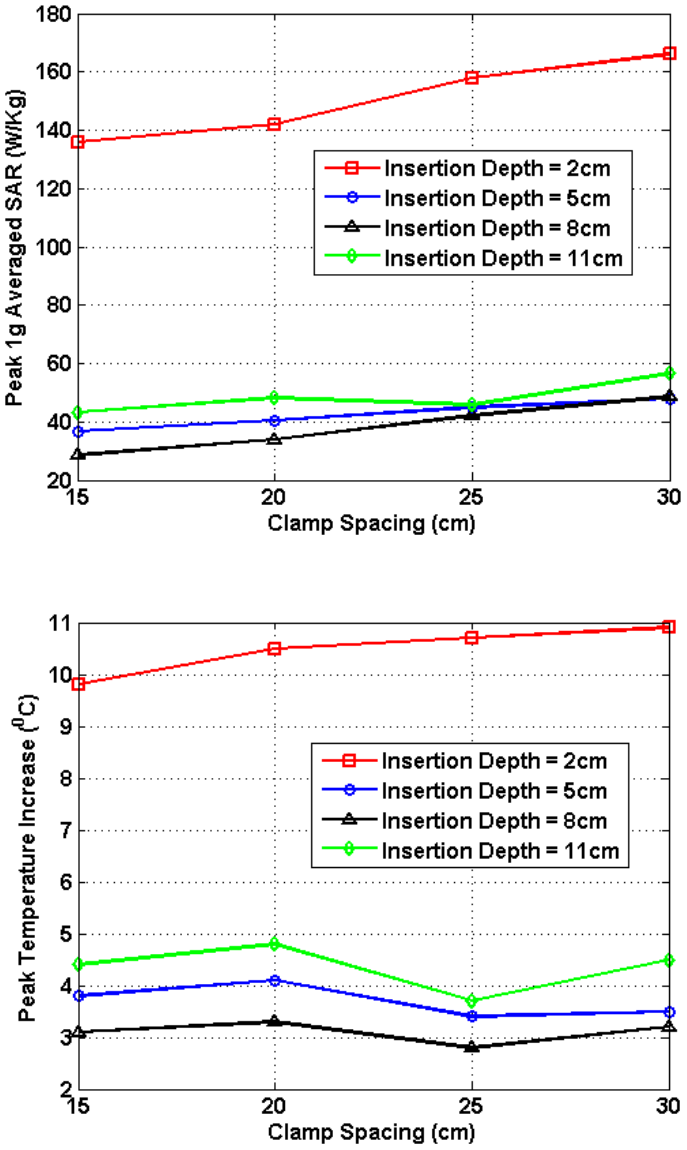

Figure 3-12 Peak 1g Averaged SAR (Top) and maximum temperature rise after 15 min MRI scan (Bottom) for carbon fiber bar in 3T MRI.

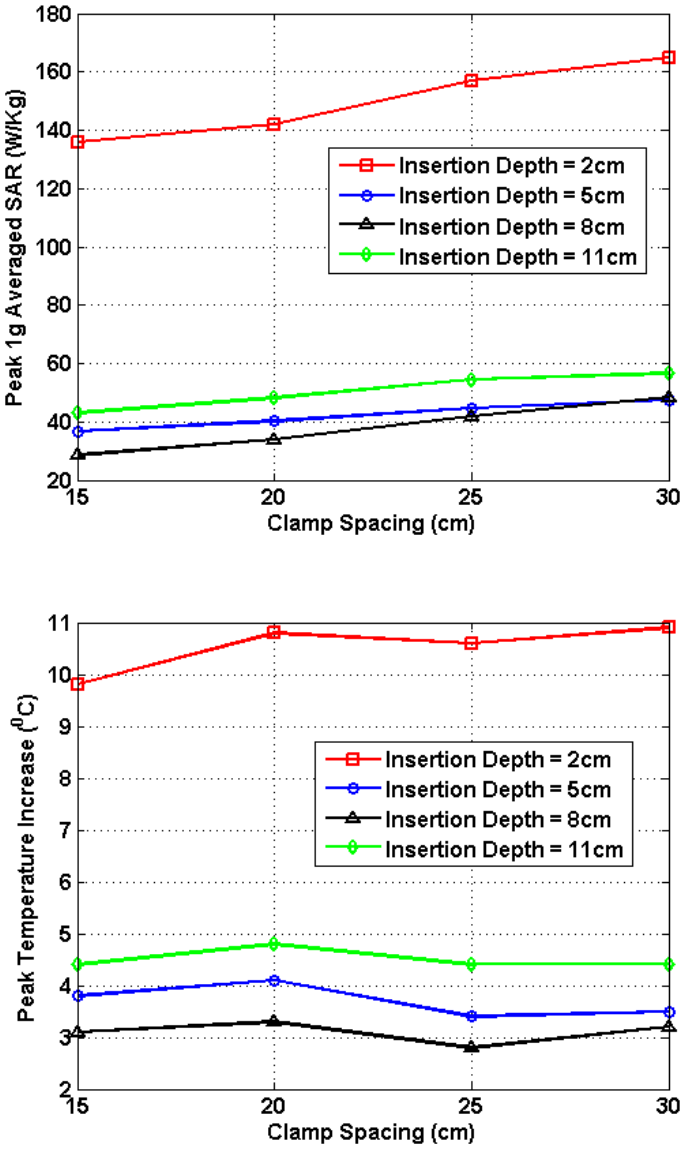

Figure 3-13 Peak 1g Averaged SAR (Top) and maximum temperature rise after 6 min and 15 min MRI scan (Bottom) for PEC bar in 3T MRI.

Similarly, the in 3-T MRI, the device with a plastic glass bar results in less surface heating than devices with the carbon fiber bar and PEC bar. However, the difference between temperature rises is not significant. This indicates that at 3T, the major heating sources come from the induced energy on the clamps and the pins.

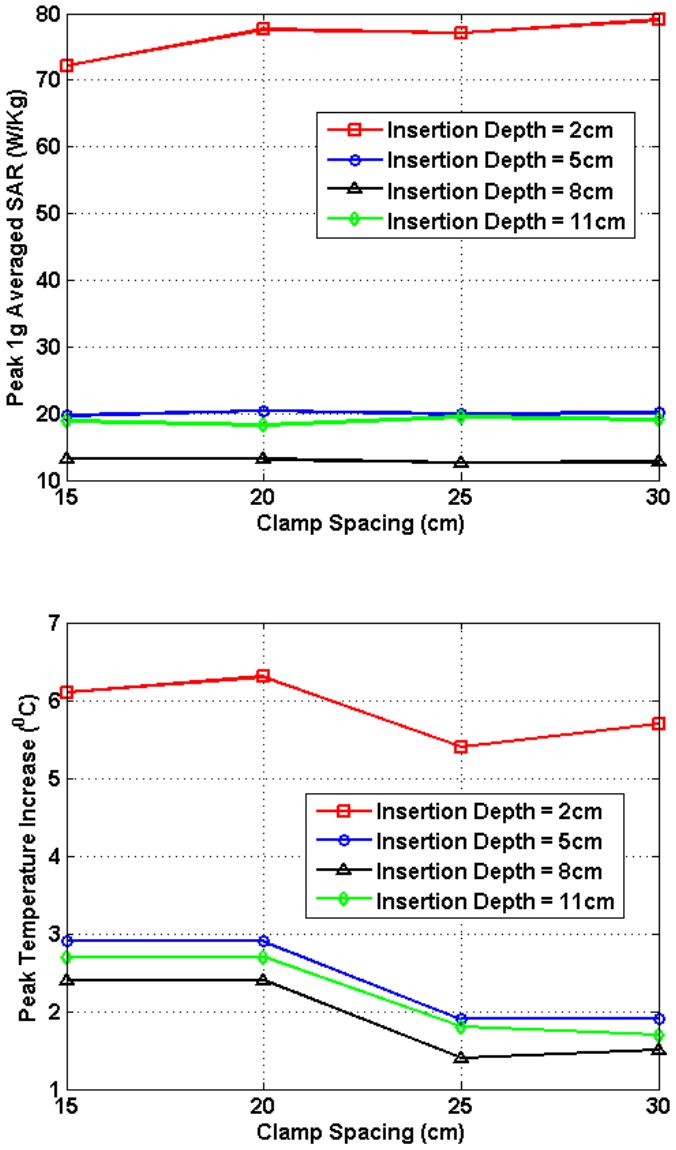

Figure 3-14 Peak 1g Averaged SAR (Top) and maximum temperature rise after 15 min MRI scan (Bottom) for plastic glass bar in 3T MRI.

From these simulation results, it is determined that the heating of the external fixation device is related to the power loss at the pin area which comes from the induced current flowing towards the tips of these pins. The total induced current comes from three parts: induced current on the device bars, induced current on clamps, and induced current on pins. The primary component of the electric field generated by the MRI RF coil is

parallel to the bar and perpendicular to the pins (this is especially true for the 1.5T system). Therefore, the induced current on the pins may be negligible compared with the induced current coming from the other parts of the device. It is also observed that when the pin spacing increases, the induced current on the device bar will increase as long as the bar is conductive. When the connecting bar is insulated, there will be no induced current on the bar which results in less power loss in the pin, and thus a lower temperature rise.

The energy depositions inside the ASTM gel along different pins are shown in Figure 3-15 and Figure 3-16 for 15 clamp spacing at four different insertion depths. For the 1.5-T system, the highest energy deposition occurs at the tip of the outside two pins. The inner two pins have less energy deposition near them. When the inserting depth increases, the heating effect tends to decrease dramatically. Because the ASTM gel is electrically lossy, as the induced energy travels towards the tip of the pin, a longer insertion depth will lead to more power dissipated along the path. Thus, the shortest insertion depth can reserve the most power and generate the worst-case heating.

For the 3T system, the frequency for the RF field is 128 MHz which is twice the frequency for the RF field in the 1.5T system. Consequently, the induced energy traveling along the pin inside the phantom gel will decay faster in the 3T system than in the 1.5T system. As a result, the 2 cm insertion structure still has the highest heating. However, when the insertion depth goes beyond 5 cm. the power loss will occurs around a longer path. Therefore, for deep pin insertion at 3T, the pin tip heating is no longer of concern.

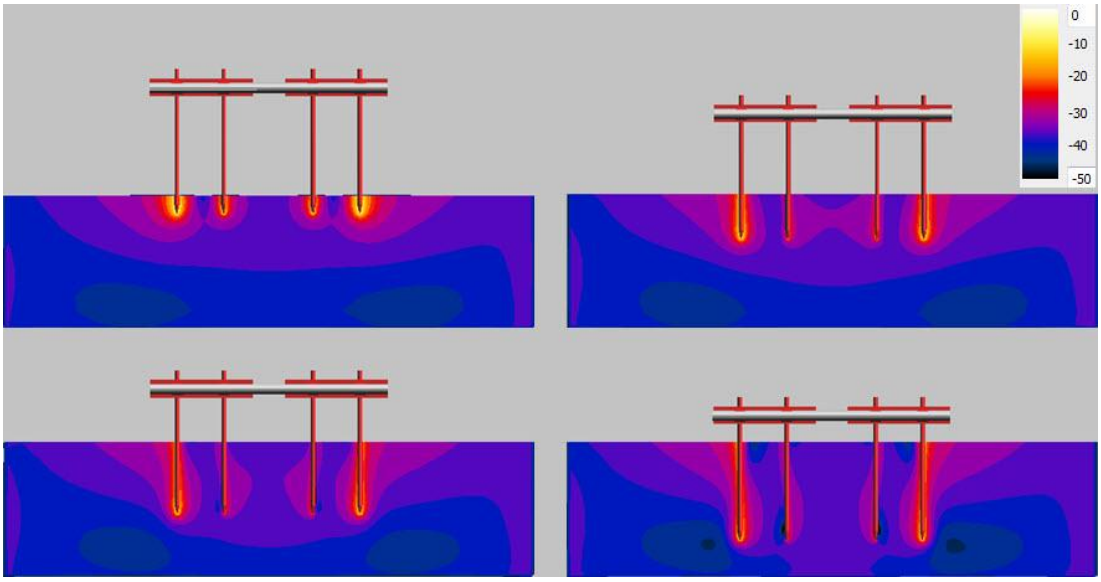

Figure 3-15 Power loss along the device pin with different insertion depth in 1.5-T MRI.

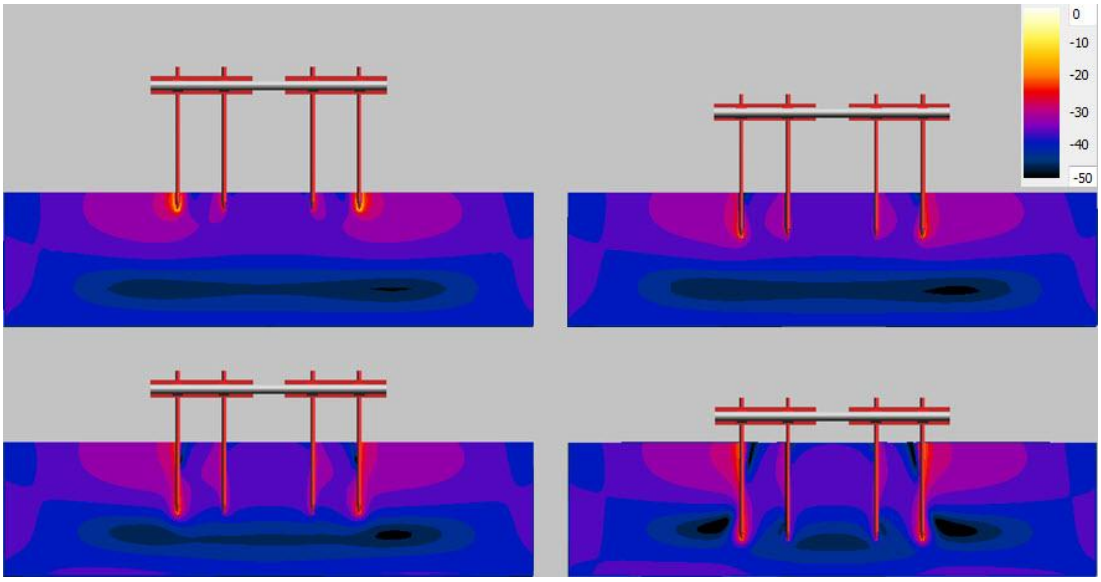

Figure 3-16 Power loss along the device pin with different insertion depth in 3-T MRI.

Numerical simulation is used to study surface heating for external fixation devices in both the 1.5-T and 3-T MRI coils. Typically, the shortest insertion depth and largest pin spacing with the conductive bar will result in worst-case heating. The heating

mechanism is explained using induced current along the device and power decay inside the ASTM phantom.

3.2.2 Dielectric Layer Effect on RF Heating

In the previous section, it was observed that the external fixation device often has a higher heating than that of the implanted passive device. During MR scans, the induced currents are generated on the metallic surfaces of the device. The induced energy propagates towards the pin and generates large local energy deposition at the tip region. This localized energy deposition then produces high local heating. If the pin is electrically connected to other metallic components of the device, all the current can flow freely to the pin. Accordingly, a significant temperature increase can be observed at the tip of the pin. However, if the pins are insulated from the clamps, it can potentially reduce the energy propagation onto the pin from other metallic components. Consequently, in some designs, an insulation layer was placed between the pins and clamps. If this assumption is true for the external fixation device, it may be a feasible method to reduce the RF induced heating by adjusting the electrical properties for the insulated layer material.

If this assumption is true for the external fixation device, it will be a feasible method to reduce the RF induced heating by changing the electrical properties for the insulated layer material. The external fixation device is used for stabilization and immobilization of long bone open fractures. The device is generally composed by frames, clamps, pins, and connection bars. A simplified external fixator model has been used to study the clamp spacing, insertion depth, and connection bar material effect on the RF heating in the MRI environment [8]. The simplified model is shown in Figure 3-17. It is

comprised of three parts: 1) two metallic blocks to represent the frames and clamps; 2) two connection bars between the metallic blocks; 3) four pins which are screwed into the bones during surgery. The metallic block has the dimension of 11.4 cm by 2 cm by 3.75 cm. The pin has a diameter of 0.5 cm and length of 16 cm. The connection bar has a diameter of 1.1 cm and a length of 41.5 cm. From [44], four different insertion depths are used and a shallow insertion of 2 cm is found to produce the highest RF heating. In this study, to minimize the error, a 2 cm insertion is used.

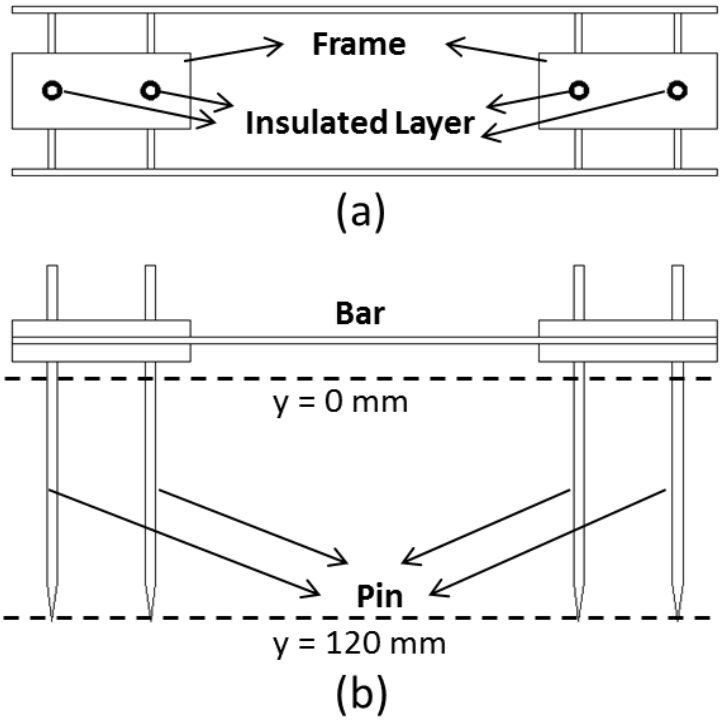

Figure 3-17 (a) Insulated layer position on external fixation device; (b) Location of y = 0mm and y = 120mm on device pins.

The ASTM standard has recommended the implanted medical device be placed at the maximum incident electric field location to minimize the error. Liu, et al. [43] indicates that the region that has the maximum electric field is located at the center plane of ASTM gel and close to the inner side wall of the ASTM phantom shell. So the

implanted orthopedic device is placed in that region which is 2 cm away from the inner side wall of the ASTM shell. However, the ASTM standard didn't mention the placement information for external fixation. In fact, the heating mechanism for the external fixation device is much more complicated than most implanted orthopedic devices [44]. It is related to a lot of factors, e.g., incident tangential electric field distribution, insertion depth of pin inside the ASTM phantom gel, and non-conductive material used at the connection part on the device. In this study, a high-incident tangential electric field is used to place the device. Even if a high RF heating is not guaranteed when the incident electric field is high, the fixed device placement will be enough for the study of the insulated layer effect on RF heating. The dielectric layer is modeled as a ring structure with inner diameter = 5 mm and outer diameter = 7 mm placed between the block and pin to simulate the insulator used in the real device product. Detailed structure of the device model is shown in Figure 3-17. And the electrical properties for materials are shown in Table 3-4.

Table 3- 1 Electrical Properties for Materials of External Fixation System and ASTM Phantom

	Relative Permittivity	Electrical Conductivity (S/m)
ASTM Phantom GEL	80.38	0.448
ASTM Phantom Shell	3.7	0
Device Bar (Carbon Fiber)	10	5600000
Insulated Layer 1	1	0
Insulated Layer 2	2	0
Insulated Layer 3	3	0
Insulated Layer 4	5	0
Insulated Layer 5	7	0
Insulated Layer 6	9	0
Device Other Parts(PEC)	\	\

In Figure 3-18 (a), the external fixation device is shown with the ASTM gel. Fours pins, namely Pin1, Pin2, Pin3 and Pin4 are defined from left to right. The

maximum heating region is found to be located at the tip of pin4. Variation of the dielectric constant of the insulated layer material is found to have a significant effect on the local SAR value at the maximum heating region. Comparison of local SAR distribution in the maximum heating region using different insulated materials ($\varepsilon_r = 1$ and $\varepsilon_r = 9$) is shown in Figure 3-18 (b). Comparison results for all insulated materials are shown in Figure 3-19. Maximum 1g averaged SAR values near the four pins are plotted. The local SAR for external fixation device without any insulated layer is plotted as a reference. From Figure 3-18 and Figure 3-19, it is noticed that high permittivity for insulated material ($\varepsilon_r = 5, 7, 9$) could result in worse heating at the pin tips than insulated material with a low permittivity ($\varepsilon_r = 1, 2, 3$). The dotted line in Figure 3-19 is the local SAR results at pin tips without the insulated layer.

The local SAR for the device with insulated layers ($\varepsilon_r = 1, 2, 3$) is smaller than that without the insulated layer, which shows a capability to reduce heating using a low permittivity material as the insulated layer is placed between pin and clamp. However, high permittivity materials ($\varepsilon_r = 5, 7, 9$) could induce even higher heating than that without the insulated layer. Normally, the insulated layer between two good conductors is equivalent to a series capacitor. High permittivity material can result in high capacitance and increase the capacitor coupling between pins and clamps. Thus, adding an insulated layer between pin and clamp could not guarantee a decrease in RF heating compared to a device configuration without an insulated layer. In this study, material with $\varepsilon_r = 2$ is found to be good enough to reduce the local SAR from 649 W/Kg (no insulated layer) to 209 W/Kg which is equivalent to reducing 67.8% temperature rise at pin tips.

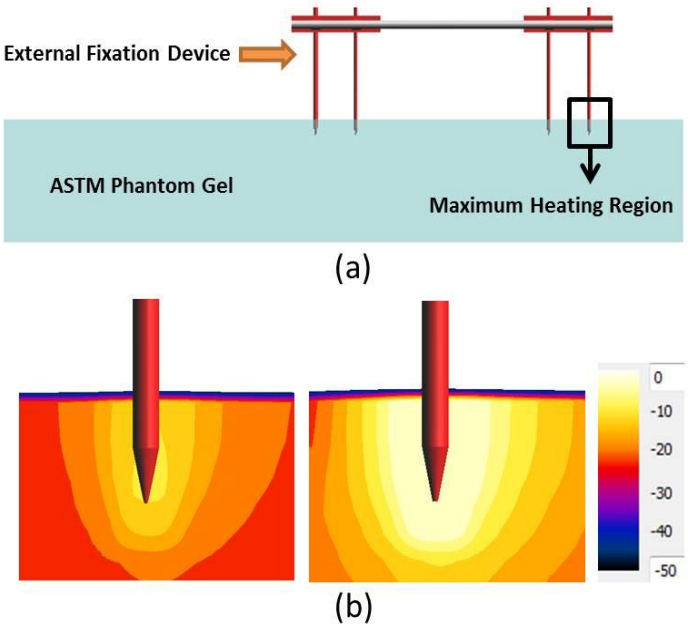

Figure 3-18 a) External fixation device insertion in ASTM Phantom Gel; b) Local SAR (1g averaged) distribution for different dielectric layer material: $\varepsilon_r = 1$ (left) and $\varepsilon_r = 9$ (right).

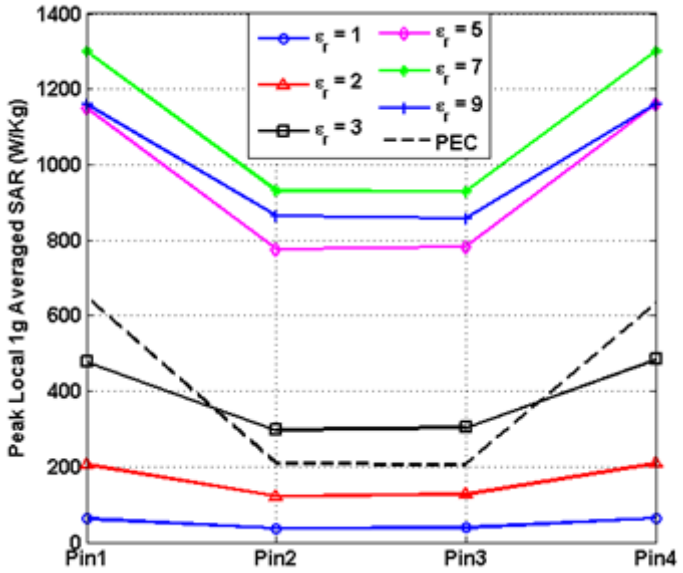

Figure 3-19 Peak local 1g Averaged SAR at four pins (Pin1, Pin2, Pin3, Pin4) for 5 insulated layer material ($\varepsilon_r = 1$, $\varepsilon_r = 2$, $\varepsilon_r = 3$, $\varepsilon_r = 5$, $\varepsilon_r = 7$, $\varepsilon_r = 9$) and no insulated layer (PEC).

To understand the efficient of the coupling path between pins and clamps, the induced current along the pins starting from y = 0 mm (closed to insulated layer) to y =

120 mm (pin tip). The locations for y = 0 mm and y = 120 mm are shown in Figure 3-17. The magnitude of current along the pins can be calculated from the magnetic field around the pins. Figure 3-20 to Figure 3-23 show the magnitude of induced current with different insulated layer materials ($\varepsilon_r = 1, 2, 3, 5, 7, 9$). The power level is normalized to a 2 W/Kg whole body SAR. Current at y = 0 mm is considered as the total induced current coming from bars and frames. Figure 3-20 and Figure 3-23 show the current distribution on the outer two pins (Pin1, Pin4). Figure 3-21 and Figure 3-22 show the current distribution on the inner two pins (Pin2, Pin3). The outer pins have a larger induced current starting at y = 0 mm than the current on inner pins. The magnitude of current on the pins show the same trend to decay starting from the surface of gel (y = 100 mm) and vanish at the tip of the pin (y = 120 mm). The induced current distribution on the pin is a good illustration on how the RF power outside the ASTM phantom is coupled into the phantom gel from the device pins. And the insulated layer material can affect the efficiency for the coupling path between pins and the other component for the external fixation system. Again, for an insulated layer with $\varepsilon_r = 2$, the magnitude of induced current at y = 0 mm is 2.7 A compared with 5.0 A without the insulated layer. The induced current on the pin is reduced by 46%, and the corresponding power level is reduced by 70.8% which agrees well with the local SAR results.

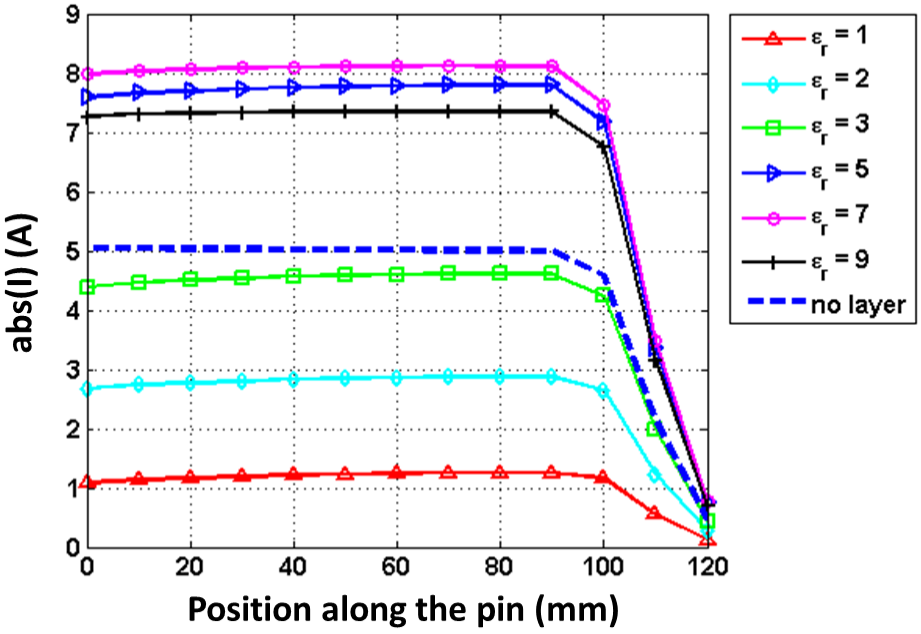

Figure 3-20 Magnitude of induced current along Pin1 without insulated layer (no layer), and with insulated layer ($\varepsilon_r = 1, 2, 3, 5, 7, 9$).

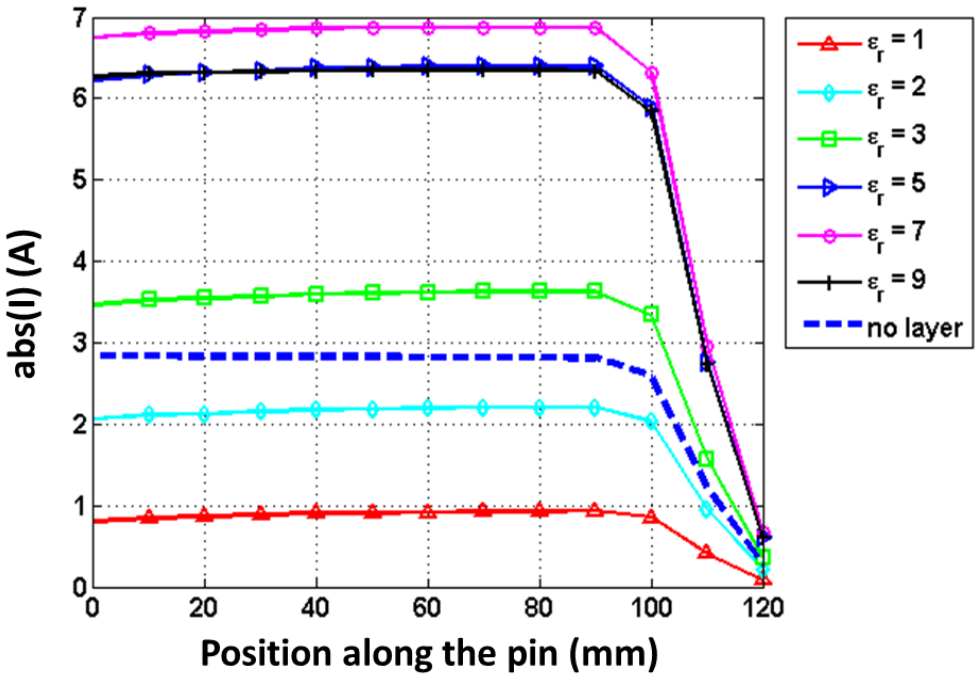

Figure 3-21 Magnitude of induced current along Pin2 without insulated layer (no layer), and with insulated layer ($\varepsilon_r = 1, 2, 3, 5, 7, 9$).

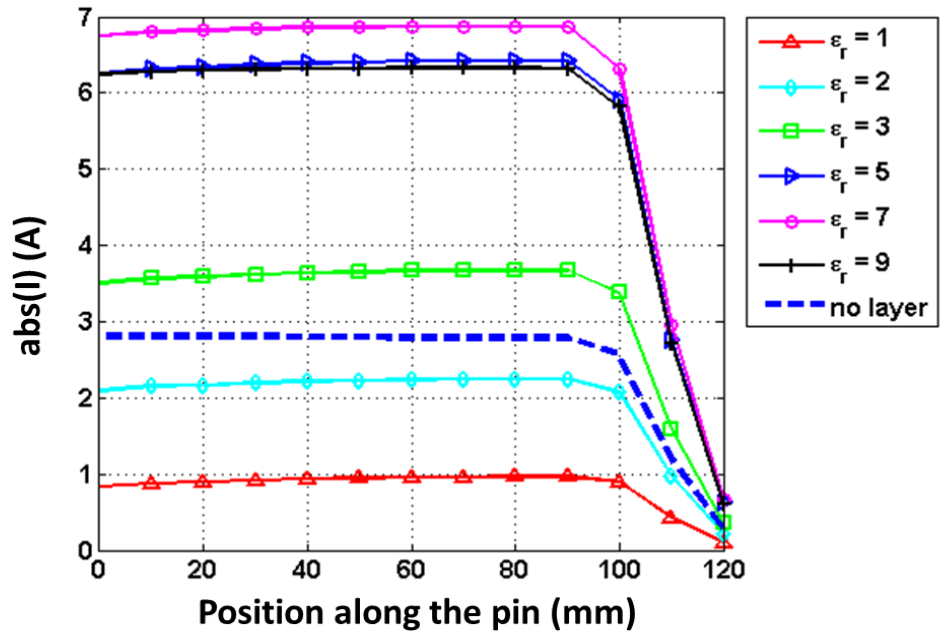

Figure 3-22 Magnitude of induced current along Pin3 without insulated layer (no layer), and with insulated layer ($\varepsilon_r = 1, 2, 3, 5, 7, 9$).

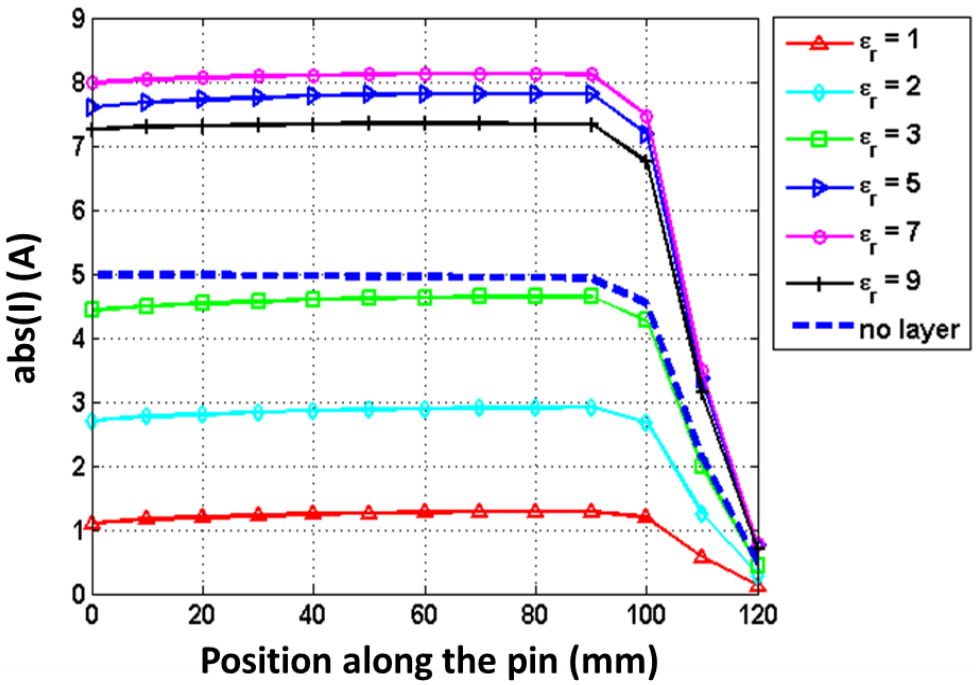

Figure 3-23 Magnitude of induced current along Pin4 without insulated layer (no layer), and with insulated layer ($\varepsilon_r = 1, 2, 3, 5, 7, 9$).

The insulated layer material used in the external fixation device which is originally designed to avoid sparks in the magnetic resonance imaging system is found to be efficient to reduce RF heating at the tip of the device pins. Low permittivity materials are found to be a good candidate to weaken the coupling path between pins and the other parts of the devices. The effects on MRI RF heating of using insulation material between clamp and pin for the external fixation device was studied. It was observed that such insulated layers can potentially reduce the induced RF heating. It was also observed that a 67% heating reduction can be achieved when proper insulated material was used.

Chapter 4 AIMDs Compatibility in MRI

The passive medical devices have been studied in the previous chapter. There is, however, another type of device called the active implanted medical device (AIMD) that could potentially cause a much higher heating effect in human tissue. One widely used AIMD is the cardiac pacemaker. The pacemaker consists of a small metallic device about the size of a pocket watch and a long electrode used to deliver the electric pulse to the heart muscle. Implanted neurological pulse generator (IPG) is another kind of AIMD that is a battery-powered device designed to deliver electrical stimulation to the brain.

The AIMD has been studied extensively for a long time because of its implanted region in the human body usually located inside heart muscle or brain or some other vital part of the human body. Kainz, et al. [45] reported a maximum of 2.1^{o}C temperature increases at the lead tip for neurological pulse generators which is not considered harmful to the patient. However, much more hazardous heating effects are found by some other studies. Achenbach, et al. [46] reported a temperature increase of 63.1^{o}C for a particular pacemaker lead and Sommer, et al. [47] obtained temperature increase ranging from 0.1^{o}C to 23.5^{o}C, depending on the electrode type. Pisa, et al. [48] found temperature increments from 0.6^{o}C to 15^{o}C for a 6-minute MRI investigation using a thorax model. Mattei, et al. studied the induced heating on metallic leads by measuring 374 experimental configurations, and demonstrated that the locations of the leads in the phantom and the lead structure have significant influence on pacemaker leads tip heating. In addition, a maximum of about a 28^{o}C temperature increase is discovered in this study [5]. In order to reduce the heating effect induced by the RF field inside MRI coil medical companies have tried to improve their pacemaker products to make them safe or at least

conditionally safe in MRI RF coils. According to [49], the new design of cardiac pacemaker can reduce the RF heating at the electrode from 20^{o}C to less than 2^{o}C in vitro. However, all the new designs for MRI safe or MRI conditional AIMDs need to be approved by the FDA before they go to the market. While it is nearly impossible to measure the temperature rise at the electrode tip in the human body, alternative methods have been developed to determine the heating effect using numerical methods [50]-[57]. In the following sections of this chapter, several modeling methods will be discussed. The first one is a direct modeling method which considers the detailed structure of AIMDs in an electromagnetic modeling tool. The second one is called the four-tier approach. This approach was first proposed by a joint working group between ISO TC 150/SC6 on Active Implants and International Electrotechnical Commission (IEC) SC 62B MT40 on magnetic resonance equipment for medical diagnosis in early 2007 [27]. The third approach is based on the reciprocity theorem which not only shows how the heating at the electrode tip could be calculated but also explains the mechanism of the RF heating.

4.1 Limitation of Direct Simulation

The MRI safety problem becomes much more difficult to analyze when considering AIMDs with very fine structure such as the cardiac pacemaker and the vagus nerve stimulation (VNS) devices. Generally, the most challenging part in numerical modeling is to generate correct mesh in the FDTD method to describe lead structure. The lead is the long and thin electric conduction coaxial line or twin line structure which delivers an electrical pulse from the pacemaker to the electrode. The length of the lead is typically 40 cm to 60 cm. The diameter of the lead is generally less than 3 mm. Moreover,

the thickness of the conductors is usually measured to be less than 0.5 mm. All of these factors make it impossible to numerically model a detailed lead. To generate an accurate FDTD mesh, a minimum resolution of 0.2 mm is selected. The mesh size is more than 500 Mega cells. In order to accelerate the simulation, the NVidia Tesla 2070 graphic card is used. In Figure 4-1, it shows that even the graphic card can largely accelerate the simulation speed; the computational size is limited by the memory of the graphic card which can only handle a maximum of 400 Mega cells. This plot comes for the SEMCAD X performance data available at the website for Schmid & Partner Engineering AG [58].

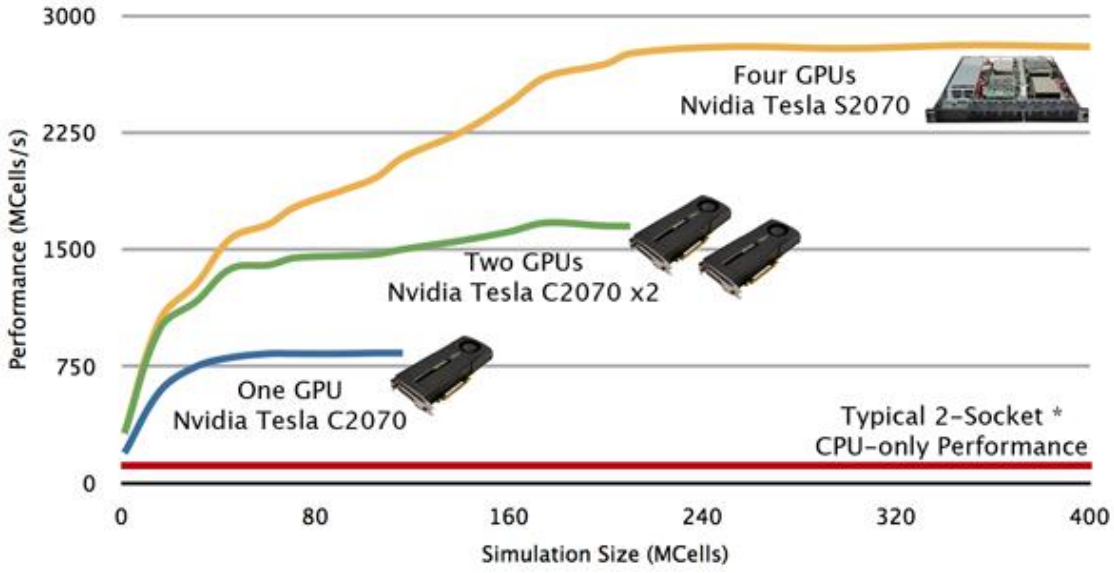

Figure 4-1 Acceleration of Nvidia graphic cards.

It turns out that the large mesh size is not only caused by the thickness of the inner and outer conductors of the coaxial lead, but also is caused by the arbitrarily winding pattern. A typical lead path starts from the pectoral region under the human skin, goes into the Subclavian vein, then goes into the heart and is inserted into the heart muscle. This winding pattern is much more difficult to model than a simple straight lead.

Thus, the straight lead structure became the first step to understanding the AIMD RF heating.

The straight coaxial lead turns out to be very easy to model using SEMCAD X. But this method is largely limited when modeling the real winding lead model shown in figure 4-3. Another limitation is the ability to model lumped structure or more detailed distributed structure (e.g., helix lead). To improve the RF safety property of the pacemaker device, one efficient way is to add a filter structure before the distal lead to choke the 64 MHz or 128 MHz RF field flowing along the lead. This technique is used to shift the heating spot from the distal lead to the filter location. The filter is equivalent to a parallel resonant circuit which has the maximum impedance at resonant frequency. To consider the parallel resonant circuit in the winding lead model, the lumped element needs to be added into the lead structure which further increases the final mesh size. The most challenging issue for direct modeling is perhaps the consideration of the helix lead. In the AIMD product, the conduction lead is not exactly the same as the coaxial cable. Instead of using a continuous conductor, the lead is constructed using a helix line while the adjacent pitches are in touch with each other. This structure is intentionally manufactured to ensure the mechanical property of the lead since it needs to be wound or twisted during surgery. In low frequencies, however, this helix conduction lead is equivalent to the coaxial lead. But when the frequency is high, there will be a difference between the performance of the helix lead and the coaxial lead.

4.2 The Four-Tier Approach

Due to the limitation of direct modeling of AIMDs in MRI RF environment, the ISO/TS 10974 Standard for AIMDs was developed in 2007 [27]. According to the

ISO/TS 10974 Standard for AIMDs, the Tier 1 approach was meant to get the maximum electric field inside the human body, and the Tier 2 approach was meant to get the maximum electric field inside the implanted region which includes the pectoral region, vein, and heart. Tiers 1 and 2 are very simple to process as long as the implanted region or chest region is generated. The Tier 3 approach is to get the tangential electric field along the lead path. Obviously, the first step of Tier 3 is to define enough curves to cover the clinical lead paths as much as possible. The following work is collaborated with St. Jude Medical, Inc. to generate a total of 14 subcutaneous device pocket sites, 6 venous access sites, and 9 intra-cardiac pacing sites. These sites were selected to be clinically representative lead paths and to implement Tier 3 approaches on all the lead paths. The subcutaneous device pocket sites were limited to the pectoral and submammary regions on either the left or right sides. The venous access sites were limited to the axillary, subclavian, and jugular veins on either the left or right sides. The intra-cardiac lead tip implanted sites were limited to the right atrial and right ventricular endocardium. Using the various combinations of selected sites a total of 198 pathways were defined. Among the 198 pathways there are a total of 54 pathways originating from a subcutaneous device pocket located in the submammary region which are only applicable to the adult female model, thereby reducing the total number of pathways to 144 for the obese male, adult male, girl, and boy models. Depending on the length of the MRI pacing lead chosen, the number of pathways may be further reduced if the lead length is not sufficient to extend over the entire pathway encountered with each model.

4.2.1 Tier 3 Approach

Induced currents on the metallic housing of small metallic implants due to radio frequency (RF) fields during MRI scans can cause heating in the tissue around it. The ISO/IEC Joint Working Group (JWG) has developed the tiered approaches to establish the worst case RF heating conditions for active implantable devices utilizing computer simulations. The lower the tier, the more stringent is the criteria amongst the four tiers. Tier 2 utilizes the maximum electric field averaged over 10 g (E_{max}) in the clinically relevant implant regions. The simulated Emax value is used to set up an in vitro test condition for estimating the worst in vivo heating.

MRI simulation conditions included human body model, landmark, tissue properties, and RF coil type, diameter, and length. The flow chart in Figure 4-2 shows detailed steps taken to determine the E_{max} in the most conservative conditions. The five human body models simulated were obese male (Fats), adult male (Duke), adult female (Ella), girl (Billie), and boy (Thelonius) and the parameters are shown in Table 4-1. Following the flow chart in Figure 4-2, comprehensive simulation studies are performed.

Table 4-1 Parameters for Anatomical Human Models

Body Model	Name	Gender	Age (years)	Height (m)	Weight (kg)	Number of tissues
Obese Male	Fats	Male	37	1.78	120	84
Adult Male	Duke	Male	34	1.74	70	77
Adult Female	Ella	Female	26	1.6	58	77
Girl	Billie	Female	11	1.46	35.6	77
Boy	Thelonius	Male	6	1.17	19.5	77

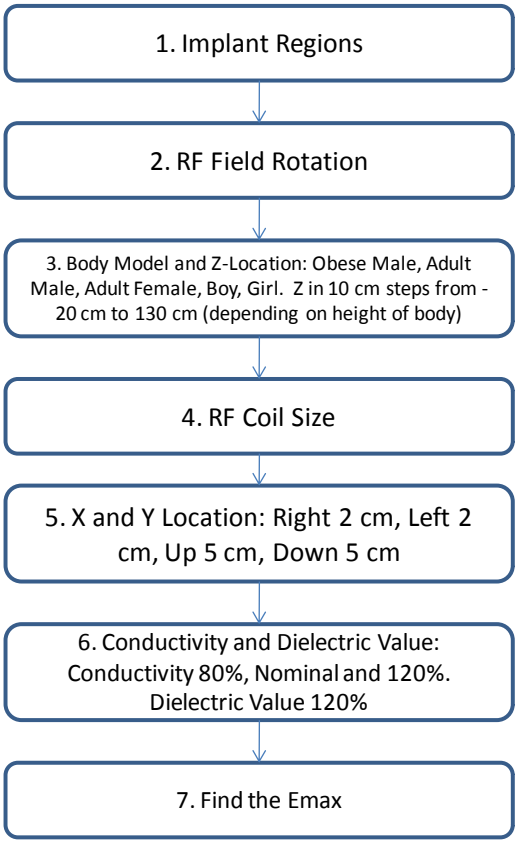

Figure 4-2 Summary of simulation conditions and model parameters.

4.2.2 SEMCAD X Simulation of Human Body Models

A SEMCAD X software package was used to simulate the electric fields generated in a human body when it is exposed to electromagnetic energy generated by an MRI RF body coil. The SEMCAD X software uses Finite-Difference Time-Domain (FDTD) methods to iteratively compute the electric and magnetic fields. These electric fields are then extracted inside the implant regions with a 10 or 8 g average. All the reported electrical fields in RMS were scaled to 4W/kg or 2W/kg. SEMCAD X models of 16-rung copper circularly polarized high-pass and low-pass RF body coils were created. For the high-pass RF body coil an ideal source (red cones in Figure 4-3) was inserted halfway between each rung. The amplitude of each source was set to 1 V. The phase delay between adjacent sources was set to $2\pi n/16$. For the low-pass RF body coils an ideal source was inserted halfway along the length of each leg. The amplitude of each source was set to 1V and the phase delay between adjacent sources was set to $2\pi n/16$. Modeling the sources this way forces the current to that of an ideal circularly polarized RF body coil [61]. Using this kind of RF body coil model reduces the simulation time and eliminates the need for tuning compared to models containing capacitors. A copper shield for the coil was also used in each simulation.

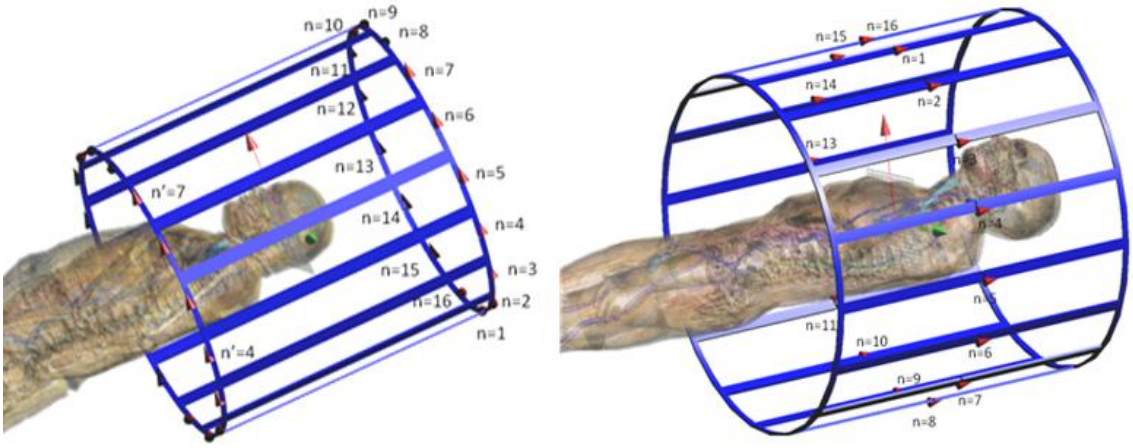

Figure 4-3 High-pass (Left) and low-pass (Right) RF body coils (shield not shown).

The simulation was halted once the electric field distribution in the simulation domain had converged (this typically requires a simulation time of 20-30 periods of the RF signals). The simulation boundaries were enclosed by the Uniaxial Perfectly Matched Layer Absorbing Boundary Condition (UPML ABC) so that impinging waves would not reflect back into the computational domain. Table 4-2 shows the grid parameters used, which created approximately 160M cells in SEMCAD simulations.

Table 4-2 Grid parameters in SEMCAD simulations

	X max step (mm)	Y max step (mm)	Z max step (mm)
Body Model	2	2	2
Coil and Shield	3	3	3
Background	20	20	20

4.2.2.1 Scale Emax to Whole Body SAR 2W/kg with Head SAR Limit of 3.2 W/kg

Once the simulation was finished the whole body SAR and the head SAR were extracted. In this process the input power was normalized to 1W, the simulation frequency was set to 64MHz and all but the RF body coil and shield were selected to be included in the SAR extraction.

The whole body SAR calculated in the previous step was relative to an input power of 1W, the target power was re-nomalizing to $\frac{2}{\text{whole body SAR}}$ in order to scale the electric field to a whole body SAR of 2W/kg.

E fields (Ex, Ey and Ez) were scaled to the 2W/kg by the square root of Desired Input Power (DIP) and then Emax was obtained in the implant region.

The head SAR calculated was relative to an input power of 1W. For the head SAR, the target power was re-nomalizing to $\frac{3.2}{\text{Head SAR}}$ in order to scale the electric field to a head SAR of 3.2 W/kg.

In order to calculate $E_{\max}$ at 2W/kg with a head SAR, the calculation can be based as $E_{\max}$ at 2W/kg and a ratio will be applied to $E_{\max}$. The ratio,

$$R_{HD\_to\_WB} = \left(\frac{3.2}{\text{Head SAR}} \right) \Big/ \left(\frac{2}{\text{Whole Body SAR}} \right).$$

If $R_{HD\_to\_WB}$ is less than 1,

$$E_{\max} = \sqrt{R_{HD\_to\_WB}} \cdot E_{\max\_2W/Kg}.$$

All the fields were scaled to 2W/kg whole body SAR with a head SAR limit of 3.2 W/kg. The simulations began with an investigation into the largest Emax values

generated in all five body models. In order to determine the effect of the body position along the Z-axis, all five body models were simulated at 10 cm steps along the Z-axis. The results of this investigation showed that the obese male model generated the highest Emax around Z-axis location = 10 mm. The next step was to determine the effect of shifting the body in the X and Y direction. The results showed that X =-20 mm and Y = 50 mm was the most conservative XY location but the effect was very small. The effect of tissue conductivity was then studied for each body model and multiple Z-axis locations. The results showed that decreasing the conductivity to 80% of nominal increased the Emax. The results of all these investigations were used to define a set of simulation conditions that would generate the most conservative Emax. All these simulations were performed with the obese model. Conductivity shifted to 80% of nominal, dielectric value shifted to 120% of nominal and within ±100mm of the most conservative Z-axis location. Effects of coil size and type as well as XY variation were studied. The entire set of simulations performed is listed in Table 4-3.

The magnetic field B1 generated by an RF coil has a circular rotation that can be either left or right in relation to the patient depending on the orientation of the main field. Both directions of rotation need to be investigated due to the natural asymmetry of the human body [62]. The oscillating B1 field induces an electric field which in turn can generate a temperature rise in the lead. The electric fields for left hand circular polarized (LHCP) and right hand circular polarized (RHCP) are conjugated to each other [63].

Table 4-3 Simulations Performed (HP = High-Pass, LP = Low-Pass)

Body Model	Coil Type	Coil Diameter (cm)	Coil Length (cm)	X (cm)	Y (cm)	Z (cm)	Conductivity	Permittivity
Obese Male	HP	73	71	0	0	-20 to 100 in 10cm steps	Nominal	Nominal
	HP	73	71	-2,0,2	0	10	Nominal	Nominal
	HP	73	71	0	-5,5	10	Nominal	Nominal
	HP	73	71	-2,0,2	0	20	Nominal	Nominal
	HP	73	71	0	-5,5	20	Nominal	Nominal
	HP	73	71	-2,0,2	0	30	Nominal	Nominal
	HP	73	71	0	-5,5	30	Nominal	Nominal
	HP	73	71	0	0	-20 to 70 in 10cm steps	80%, 120%	Nominal
	HP	73	71	0	5	0, 10	80%	120%
	HP	73	73	0	5	10	80%	120%
	HP	75	60, 66, 72	0	0	10	80%	120%
	HP	75	60	0	5	10	80%	120%
	HP	75	60	-2,2	0	10	80%	120%
	LP	75	66	0	0	10, 20, 30	Nominal	Nominal
	LP	75	60,66,72	0	5	10	80%	120%
	LP	75	60,66,72	-2,2	0	10	80%	120%
	LP	73	73	0	5	10	80%	120%
	LP	73	73	-2,2	0	10	80%	120%
	LP	75	60	0	50	0	80%	120%
	LP	75	60	-2	0	0	80%	120%
	LP	75	66	0	50	0	80%	120%
Adult Male	HP	63	71	0	0	-20 to 80 in 10cm steps	Nominal	Nominal
	HP	63	71	0	0	0 to 100 in 10cm steps	80%, 120%	Nominal
	HP	60	60,66,72,84	0	0	30	Nominal	Nominal
	HP	68,75	60,66,72	0	0	30	Nominal	Nominal
	LP	60	60,66,72,84	0	0	30	Nominal	Nominal
	LP	68,75	60,66,72	0	0	30	Nominal	Nominal
Adult Female	HP	63	71	0	0	-20 to 60 in 10cm steps	Nominal	Nominal
	HP	63	71	0	0	-10 to 80 in 10cm steps	80%, 120%	Nominal
Boy	HP	63	71	0	0	-20 to 80 in 10cm steps	Nominal	Nominal
	HP	63	71	0	0	-10 to 70 in 10cm steps	80%, 120%	Nominal
Girl	HP	63	71	0	0	-20 to 70 in 10cm steps	Nominal	Nominal
	HP	63	71	0	0	-10 to 70 in 10cm steps	80%, 120%	Nominal

4.2.3 Body Model and z Location

Five body models were used from the Virtual Population Project: obese male (Fats), adult male (Duke), adult female (Ella), girl (Billie), and boy (Thelonius) as shown in Figure 4-4 below [59][60]. The models have a meshed spatial resolution of 2 mm x 2 mm x 2 mm.

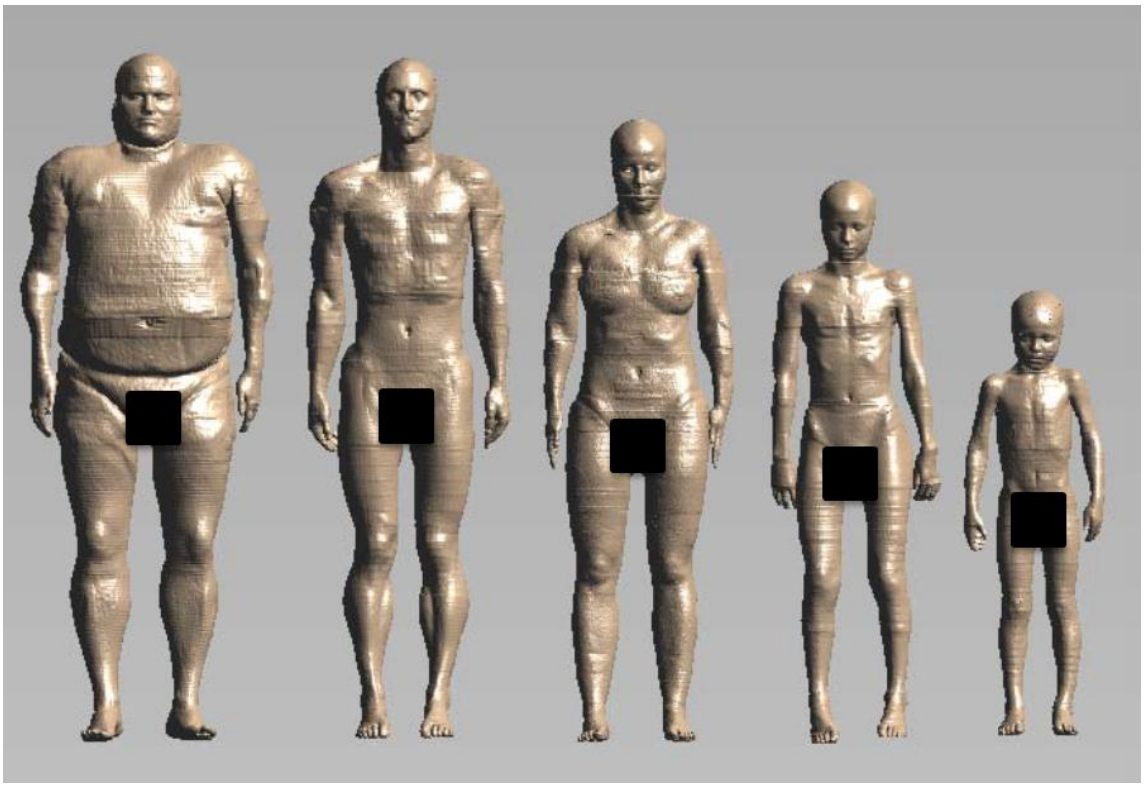

Figure 4-4 Fats, Duke, Ella, Billie and Thelonius

Each of the five body models was simulated at multiple landmark positions along the Z-axis. A 63cm (diameter) x 71cm (length) high-pass RF body coil was used for all models except for the obese male. Due to the size of the obese male, a 73cm x 71cm body coil was used in order for the model to fit inside. The models were moved in 100 mm steps along the Z-axis, with the total number of steps dependent upon the height of the models. Figure 4-5 illustrates how the 0 mm position is defined by the center of the

eyes aligned with the center of the coil, i.e., the isocenter of the coil, and 200 mm is defined as a 200 mm movement of the body towards the top of the coil.

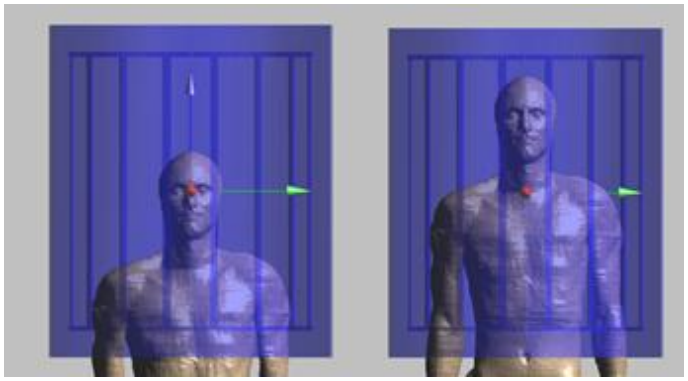

Figure 4-5 Left: Z-Axis Landmark = 0cm. Right: Z-Axis Landmark = 20cm

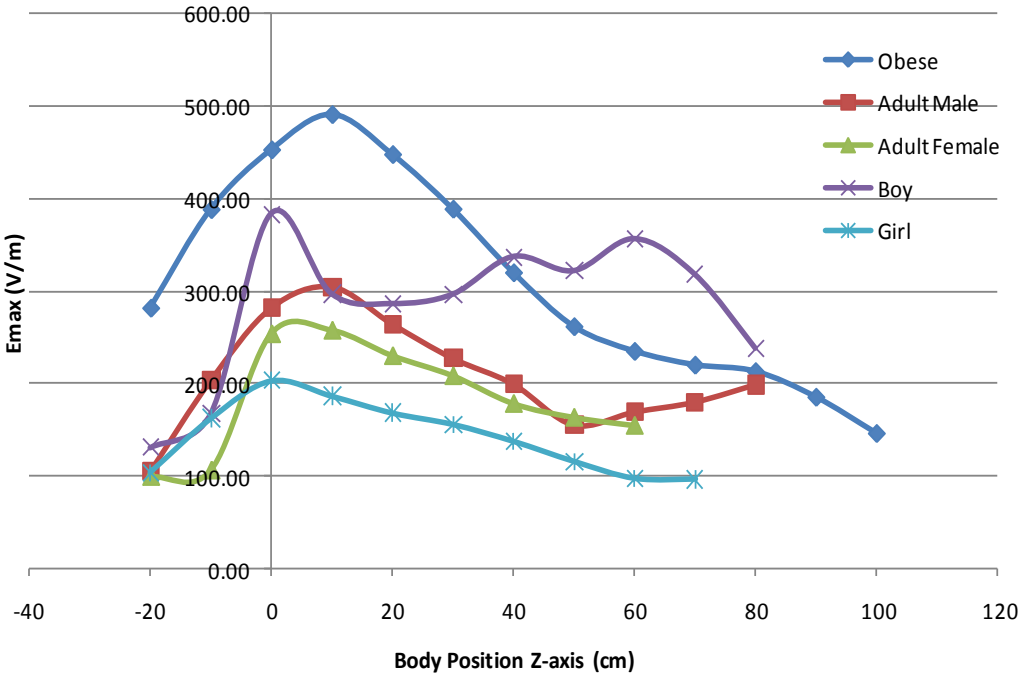

Figure 4-6 shows the maximum Emax in the implant regions of a small device in the five human body models. The largest values are seen in the obese male model, with a Z-axis position between 0 cm and 20 cm. This agrees with expectations, as the obese model is closest to the RF coil, and is therefore expected to have the worst case Emax. This also agrees with recent literature indicating that the peak spatial SAR [62] and electric field [27] are highest with the obese model. Therefore, the obese model is used in

the most conservative simulations, when fit allows (since a variety of coil sizes are simulated). Interestingly, the boy model has the next largest peak E_{max}.

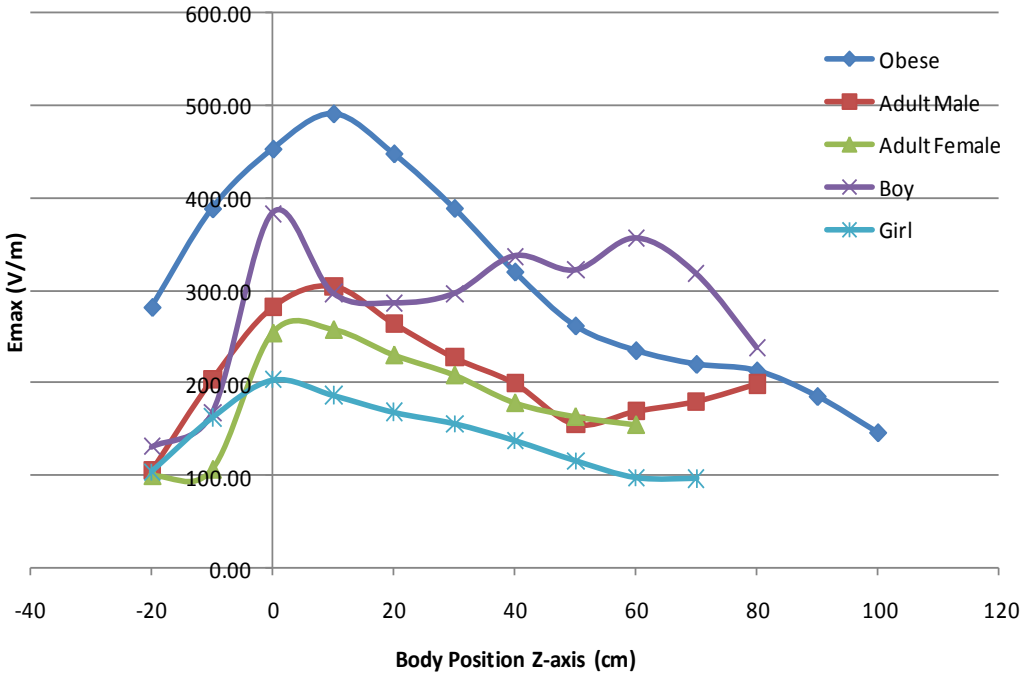

Figure 4-6 Emax vs Z-Axis position for the five body models

4.2.4 X and Y Location

The effect of the X and Y-axis landmark was investigated to determine the additive effect of patient position or shifting within the coil. Figure 4-7 below defines the three axes (as seen by the patient): the X-axis is right to left, the Y-axis is back to front, and the Z-axis is foot to head in the supine position. Simulation setup is shown in Table 4-4.

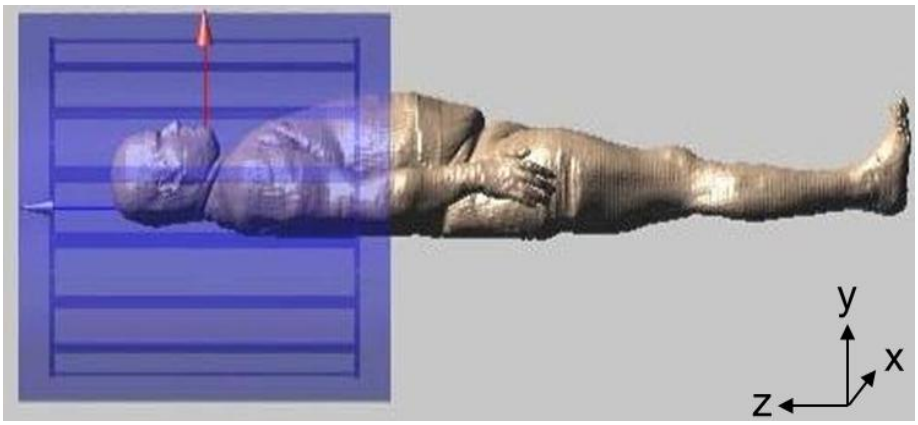

Figure 4-7 Obese Male, Landmark X = 0mm, Y = 50mm, Z = 100mm

As expected, even in the largest coil, the obese model does not allow much room for movement along the X and Y axes while keeping the model completely inside the RF coil structure. The X and Y-axis shifts were studied at the three Z-axis locations near the largest Emax. As a result, the following landmarks were simulated with the obese model using a 73 cm x 71cm high-pass coil:

Table 4-4 X, Y, Z Landmarks Simulated

X (mm)	Y (mm)	Z (mm)
0	0	100
20	0	100
-20	0	100
0	50	100
0	-50	100
0	0	200
20	0	200
-20	0	200
0	50	200
0	-50	200
0	0	300
20	0	300
-20	0	300
0	50	300
0	-50	300

The maximum E_{max} for each simulation is shown in Figure 4-8.

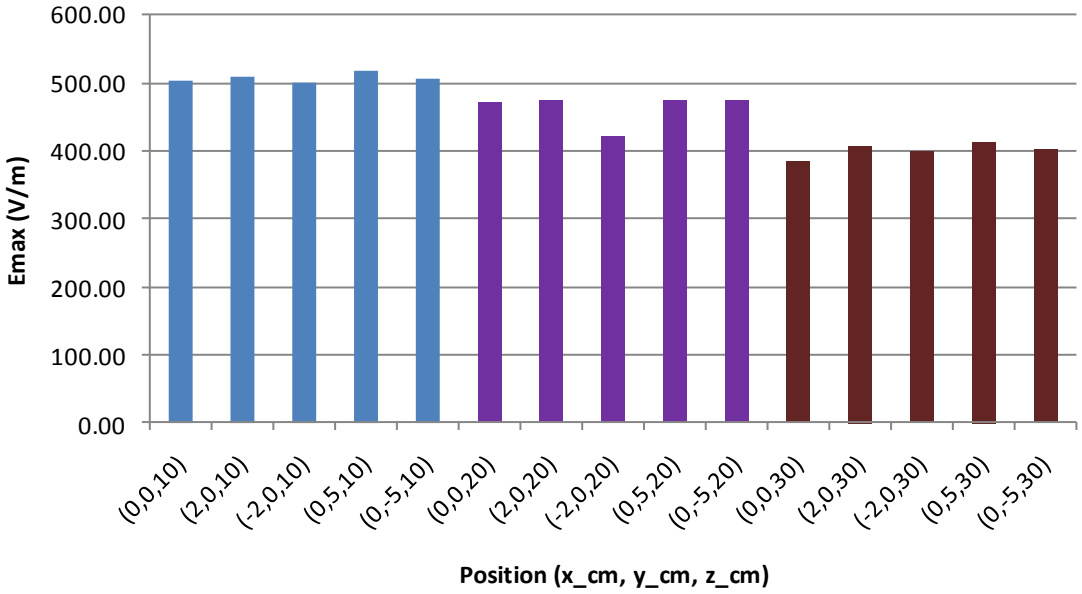

Figure 4-8 The variation due to the X and Y position was within 50 V/m that was smaller compared with those due to the Z-axis.

Analysis of the Z-axis simulations which generated the largest Emax (Z = 100 mm) shows that the absolute maximum occurs when the obese model is shifted closer to the side of the coil (-20, 0, 100) and the minimum occurs when the model is lowered by 50 mm in the Y direction (0, -50, 100). The difference between these is only ~6% of the maximum so the effect is small. When defining the most conservative set of simulation conditions, both X = -20 mm and X = +20 mm as well as Y = +50 mm were used in order to capture the slight variability. Y = -50 mm was not used since it generated the minimum Emax.

4.2.5 Tissue Conductivity and Dielectric Value

The conductivity and permittivity for each tissue were varied from their nominal in order to determine the effect of each on the simulation results. For conductivity, two initial simulations were performed in which the conductivity for each tissue was

simultaneously shifted to 80% (and subsequently 120%) from its respective nominal value [64][65], based on the ±20% tolerance specified in [27]. The two simulations were then repeated for each Z-axis landmark shown in Table 4-5. The Emax results are shown in Figure 4-9.

Table 4-5 Z-Axis Locations Where Conductivity Simulations Performed

Obese Male (mm)	Adult Male (mm)	Adult Female (mm)	Boy (mm)	Girl (mm)
-200	0	-100	-100	-100
-100	100	0	0	0
0	200	100	100	100
100	300	200	200	200
200	400	300	300	300
300	500	400	400	400
400	600	500	500	500
500		600	600	600
600		700	700	700
700		800		
		900		
		1000		

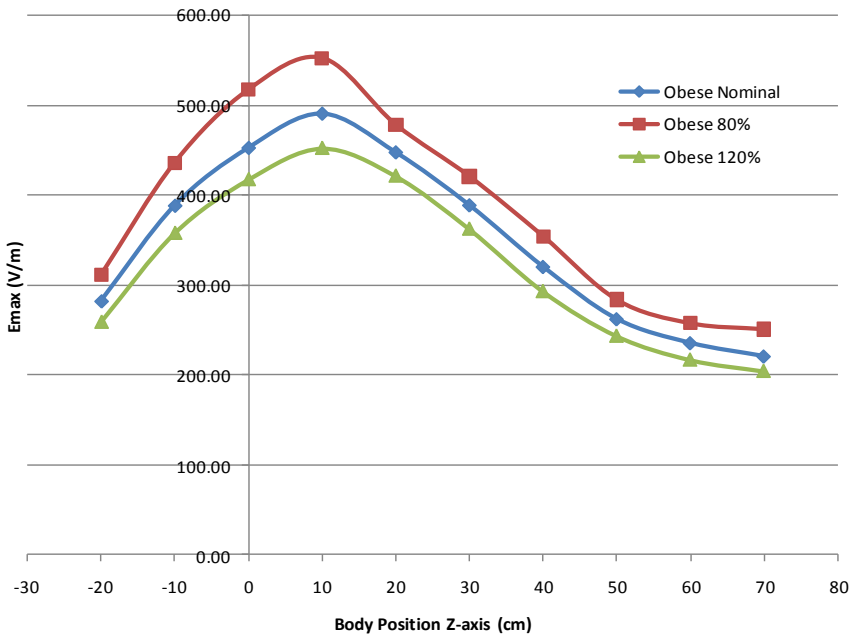

Figure 4-9 The variation in the maximum E_{max} in Obese model as the conductivity changes from 120% to nominal to 80%.

The results of this study show that the E_{max} is higher when the conductivity is shifted to 80% of nominal. These results concur with independent studies [66].

For the dielectric value (permittivity), prior studies have found that localized SAR is proportional to the dielectric value of the tissue [66]. In this study, the dielectric value of a large portion of the body model (muscle) was increased and decreased by a factor of two. The worst case SAR for all but the testicles occurred when the dielectric value was doubled.

The worst case dielectric value of +20% is based on [27]. The conclusion shows that when the conductivity and dielectric value shifted simultaneously to 80% and 120% of nominal, respectively, a larger E_{max} is generated, which defines a conservative set of simulation conditions.

4.2.6 Coil Size

A combination of coil sizes (diameter x length) were investigated in order to determine the most conservative conditions. Ten high-pass (HP) RF body coils were simulated in the dimensional combinations shown in Table 4-6 below. The coil sizes were chosen to cover the range in diameters (66.5 cm - 73.5 cm) and lengths (61.75 cm to 68.25 m) specified in the current version of the ISO technical specification [27], typical values (57cm x 65cm) reported in literature [67], and a length-to-diameter ratio of $\sqrt{2}$ (60 cm x 84 cm) which theoretically yields the maximum B1-field [68].

Table 4-6 RF Body Coil Diameter (cm) x Length (cm)

Coil Diameter (cm)	Coil Length (cm)
60	60
60	66
60	72
60	84
68	60
68	66
68	72
75	60
75	66
75	72

Each were loaded with the adult male model at the X = 0mm, Y = 0mm, and Z = 300 mm landmark. The adult male model was used rather than the obese model due to the ability of the adult male to fit in all of the above coil sizes (to reduce the number of variables in the analysis).

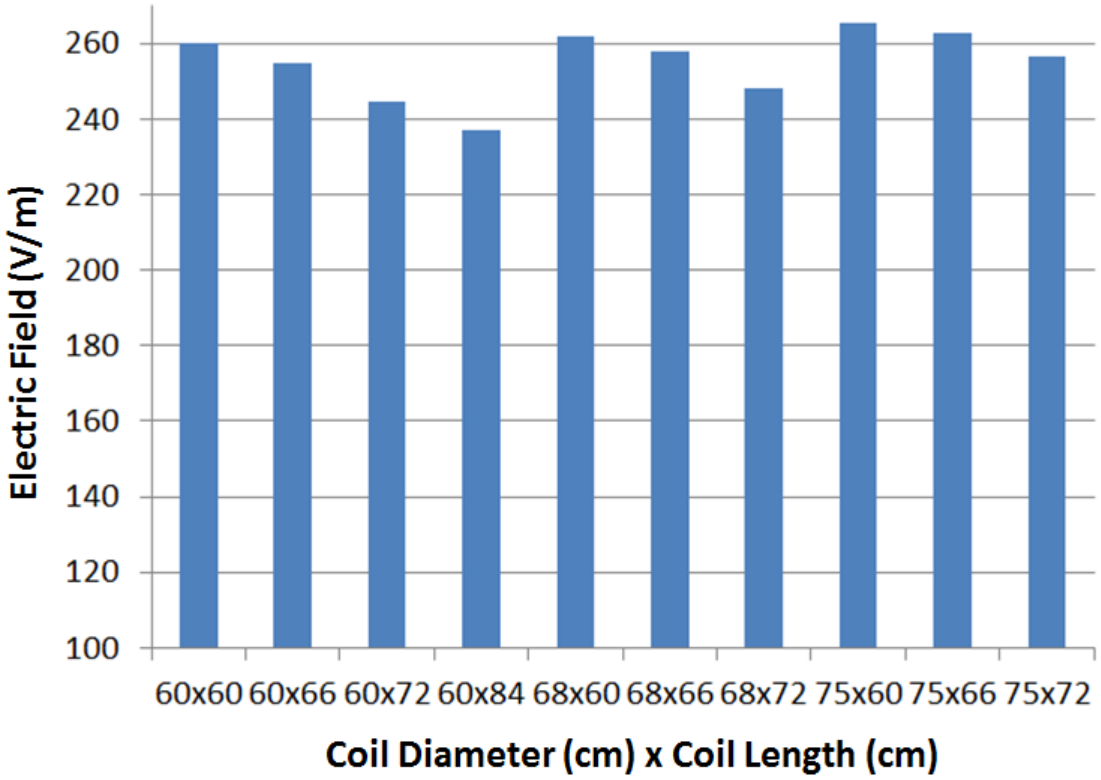

Figure 4-10 Maximum E field with different HP coil size.

Figure 4-10 shows the maximum E_{max} with HP coil with the coil sizes studied. A pattern of increasing E_{max} for decreasing length and increasing diameter is evident. The outcome that the larger diameter and shorter length coils generate larger E_{max} was used when defining a conservative set of simulation conditions.

4.2.7 Most Conservative Simulation Conditions

A set of conservative conditions was defined using the results from the previous sections. These conditions include the obese body model, 80% conductivity, 120% dielectric value, Z-axis within ±10 cm of the worst case, and XY locations of ±20 mm and +50 mm. These conservative conditions were simulated in a variety of high-pass and low-pass coils.

First, the three 75 cm diameter high-pass coils with (0, 0, 100) XYZ location were simulated to verify that the shorter length, larger diameter coils also generated the largest E_{max} when an obese model is used rather than adult male. The results are shown in Figure 4-12 and follow the same pattern as the 75 cm diameter coils with the obese male. Using the same 75 cm x 60 cm coil and changing to the obese model with 80% conductivity and 120% dielectric value caused the maximum E_{max} to be increased by a factor of 2.0 (540/266 = 2.0).

Next, high-pass coils with diameter of 73cm were simulated at Y = 5 cm and Z = 0 cm and 10 cm. The results shown in Figure 4-11 are consistent with previous findings that Z = 1 cm generates a higher E_{max} when compared to Z = 10 cm and that shorter length coils generate higher E_{max}.

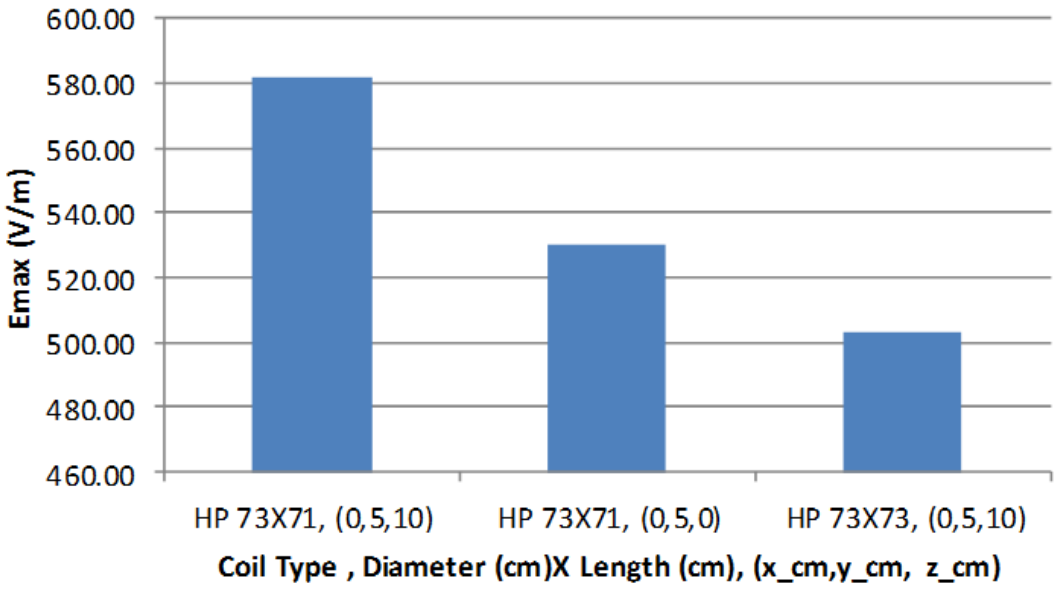

Figure 4-11 E_{max} vs Coil Length and Z-Axis (Obese Male, Cond. 80%, Dielectric V. 120%).

Another set of high-pass coils were simulated to cover the effects of variations in the X and Y directions. The results are shown in Figure 4-13 and follow the trend seen in

Section 4.2.4 where the X = 0 cm had the largest E_{max} although the variation is less than 4%.

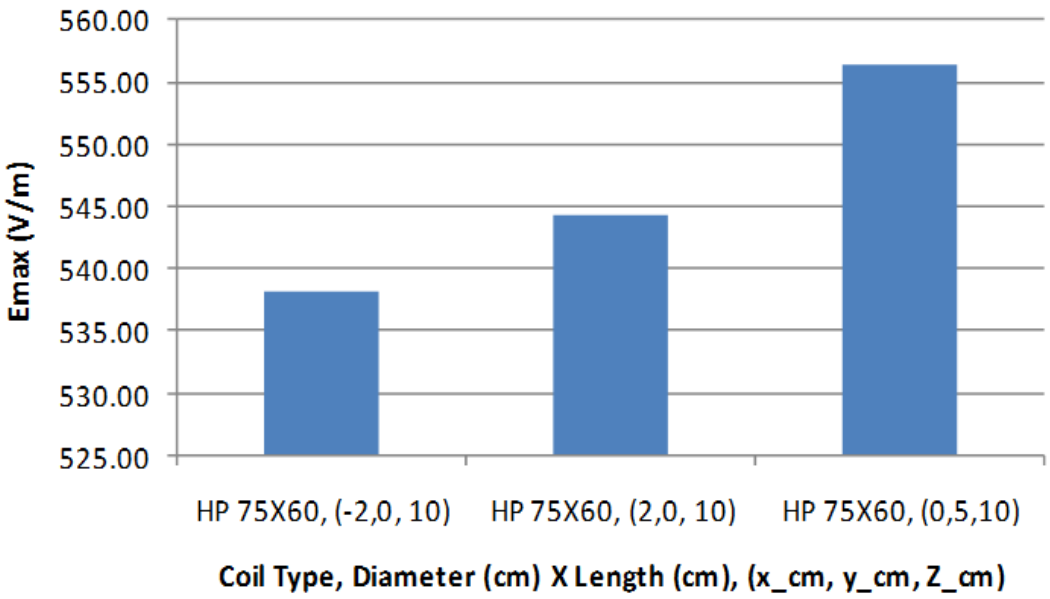

Figure 4-12 E_{max} vs X and Y Location (Obese Male, Cond. 80%, Dielectric V. 120%).

A series of simulations using low-pass coils were also performed. The first set was to verify the trend of increasing E_{max} with a larger diameter and shorter length coils seen in Section 4.2.6. Looking at just the (0, 50, 100) XYZ location for the three coil lengths in Figure 4-14 indicates that this trend does hold with low-pass coils since the highest E_{max} is seen with the 75 cm x 60 cm coil, the second largest with the 75 cm x 66 cm coil and the third with the 75 cm x 72 cm coil. Analyzing this same figure for dependence on the XY location shows that like the high-pass coil, the low-pass coil generates the largest E_{max} at Y = 5 cm.

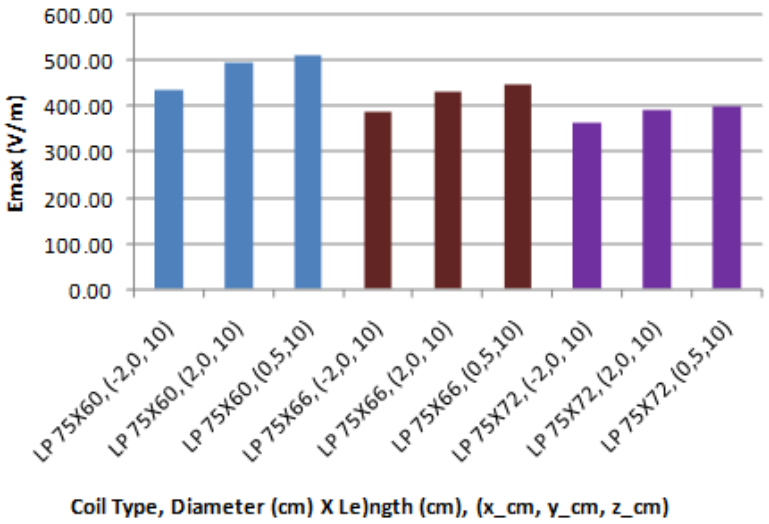

Figure 4-13 E_{max} vs Coil Length and XY Position (Obese Male, Cond. 80%, Dielectric V. 120%).

Next, a 73 cm x 73 cm low-pass coil was simulated at X = ±20 mm and Y = 50 mm. The results in Figure 4-15 compared to those in Figure 4-14 show that for the obese model in a low-pass coil, the higher E_{max} is found with the 75 cm x 60 cm coil for the same XYZ location.

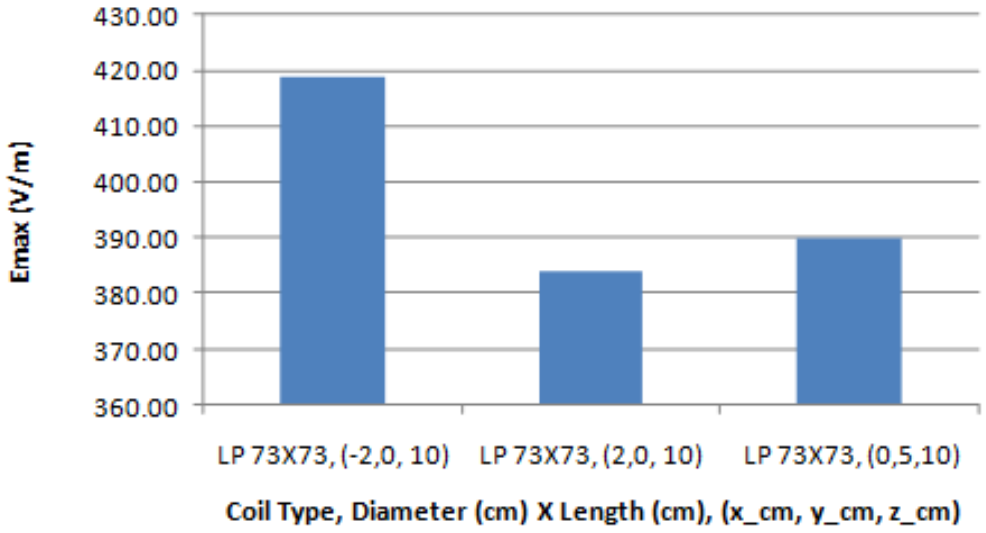

Figure 4-14 E_{max} vs XY Position for 73cm x 73cm LP Coil (Obese Male, Cond. 80%, Dielectric V. 120%).

The last set of low-pass simulations was performed with the Z-axis position = 0 mm. The results in Figure 4-15 show that the 75 cm x 60 cm coil with X = 0 mm and Y = 50 mm generate the largest E_{max}.

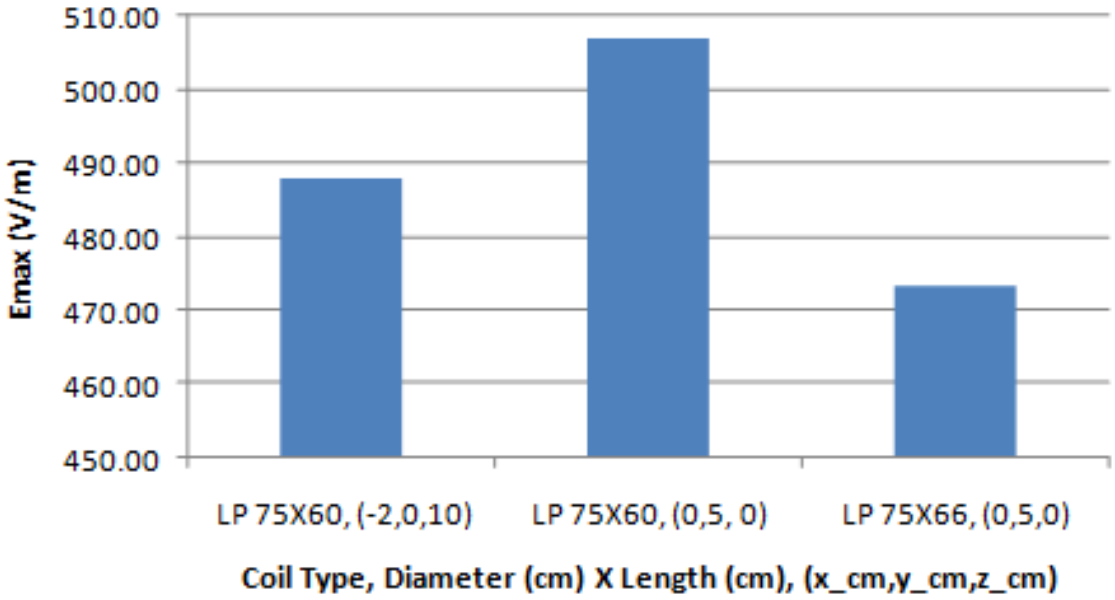

Figure 4-15 E_{max} vs XY Position and Coil Length for Z = 0mm, LP Coil (Obese Male, Cond. 80%, Dielectric V. 120%).

In over 230 simulation conditions, the worst cases of E_{max} are listed below:

The absolute highest E_{max} of 582.18 V/m for the whole body SAR of 2W/kg with 3.2 W/kg head SAR limit was found using a 73 cm x 71 cm high-pass coil (at x=0,y= 5 cm, z=10 cm).

The absolute highest E_{max} of 639.37 V/m for the whole body SAR of 4W/kg with 3.2 W/kg head SAR limit was found using a 75cm x 76 low-pass coil (at x=2 cm, y= 0 cm, z=10 cm).

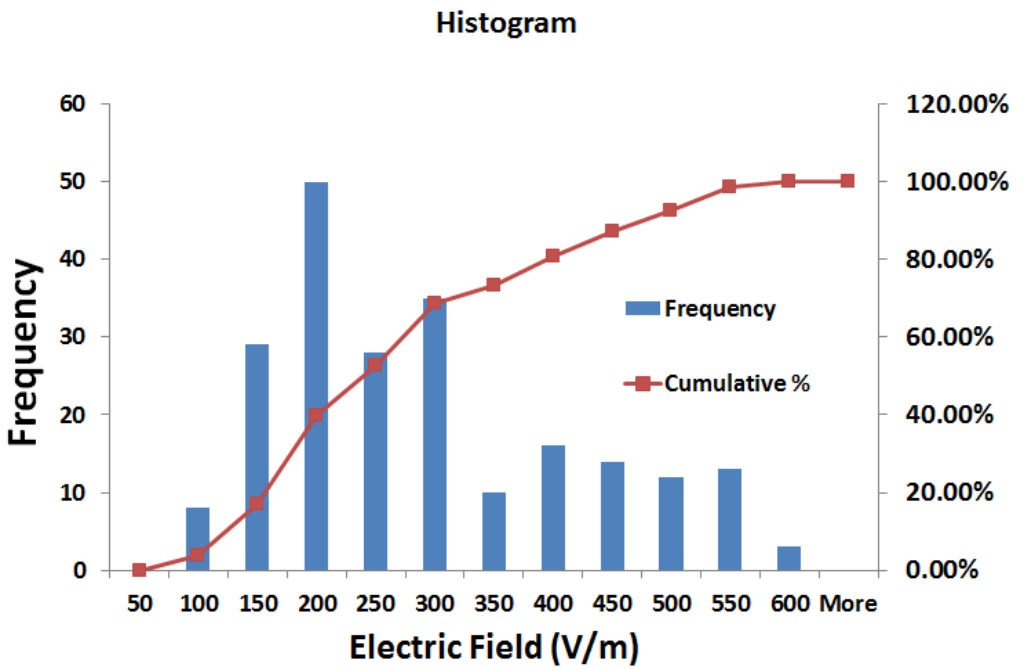

Figure 4-16 Histogram Emax distribution with 2W/kg and head SAR limit of 3.2 W/Kg.

From Figure 4-16, about 99% of the simulations fell into E_{max} <= 550 V/m with 2W/kg and head SAR limit. About 80% simulations fell into E_{max} <= 400 V/m with 2W/kg and head SAR limit. Figure 4-17 shows the distribution of simulation conditions.

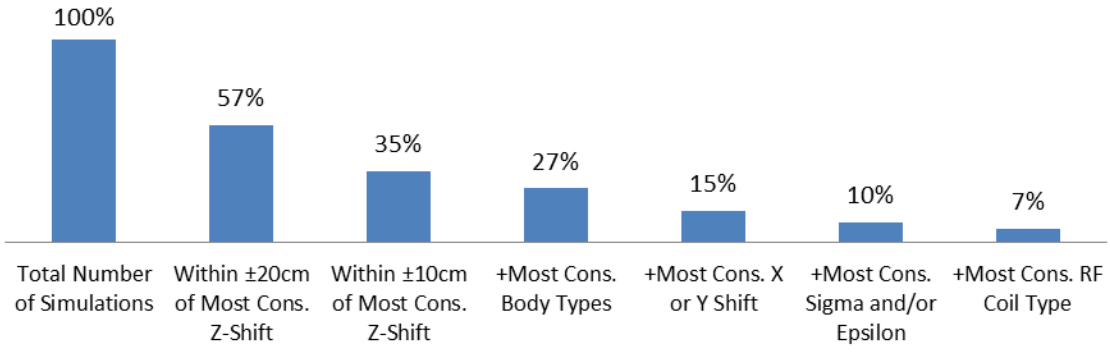

Figure 4-17 Distribution of simulation conditions.

4.2.8 Summary and Conclusions

The Global Emax from implant regions with cardiac implantable devices within the five human body models were extracted from 229 simulation conditions. With the whole body SAR of 2W/kg and the head SAR of 3.2 W/kg, the global highest Emax was 582.18 V/m and it was found using a 73 cm x 71 high-pass coil (at x=0,y= 5 cm, z=10 cm). With the whole body SAR of 4W/kg and the head SAR limit of 3.2 W/kg, the global highest E_{max} was 639.37 V/m and it was found using a 75 cm x76 low-pass coil (at x=2 cm, y= 0 cm, z=10 cm).

The Tier 2 E_{max} used the implant regions of a CRMD device that include left/right pectoral regions, left/right jugular insertion regions, heart, SVC, and left/right subclavian/innominate veins. Since the implant regions of Confirm ICM are only limited to left pectoral regions, The Tier 2 Emax from this report could overestimate the worst case Emax for Conform ICM.

4.3 Study of Tip Electric Field using Reciprocity Theorem

In the development of magnetic resonance imaging (MRI) compatibility implantable medical devices, it is often required to understand the electric field, generated to the radio frequency (RF) coils, at the tips of metallic leads. Detailed electromagnetic simulations are necessary to provide useful information to guide practical designs. However, the dimensions of the RF coils are typically on the order of meters and the dimensions of metallic leads have sub-millimeter features. To include both RF coil and metallic leads in a single electromagnetic simulation becomes computationally prohibitive due to such differences in geometrical feature sizes.

An alternative approach to calculating the tip electric field is proposed [69] which decompose the original brute-force simulations into two efficient simulations: one simulation without the metallic leads structure and the other simulation without the RF coils. The problem can be described in Figure 4-18. The above figure shows a straight lead with a single conductor inside the insulated material placed inside a host medium. It can be induced by any kind of external incident field such as the MRI exposure or plane wave incident.

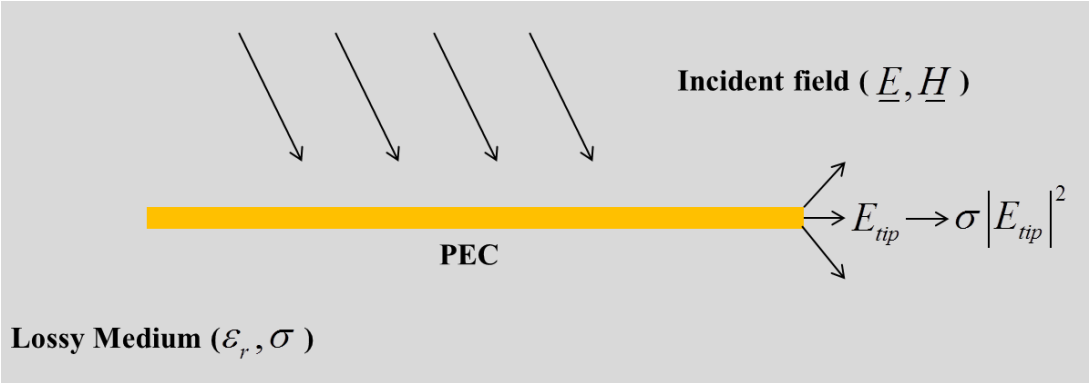

Figure 4-18 Simplified model for leads structure in MRI RF coil.

To simplify the problem, the Huygens' Principle is applied and explained in Figure 4-20. An arbitrary virtual closed surface is first chosen to enclose the lead body and then the external source can be replaced by the tangential electric current $\underline{J}^b$ and magnetic current $\underline{M}^a$ on the closed surface boundaries when the lead body is excluded in the medium. In the second simulation, a dipole testing current $\underline{J}^b$ at the tip of the lead is placed, and induced current I along the leads can be obtained. Applying the reciprocity theorem shown in Equation 4-1,

$$\int_V \left(\underline{E}^a \cdot \underline{J}^b - \underline{H}^a \cdot \underline{M}^b \right) dV = \int_V \left(\underline{E}^b \cdot \underline{J}^a - \underline{H}^b \cdot \underline{M}^a \right) dV . \qquad [4\text{-}1]$$

In the second simulation, only a unit source current is applied, there is no $\underline{M}^a$ in the above formula,

$$\int_V \left(\underline{E}^a \cdot \underline{J}^b - \underline{H}^a \cdot \underline{M}^b \right) dV = \int_V \left(\underline{E}^b \cdot \underline{J}^a \right) dV . \qquad [4\text{-}2]$$

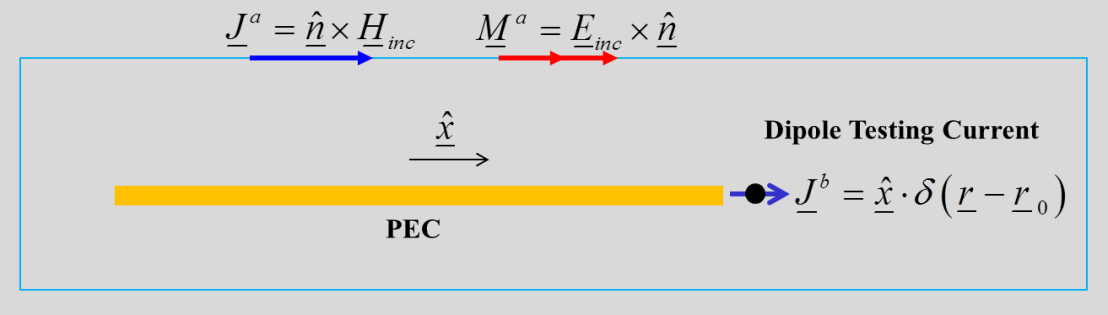

Figure 4-19 The reciprocity model for evaluating lead tip E field.

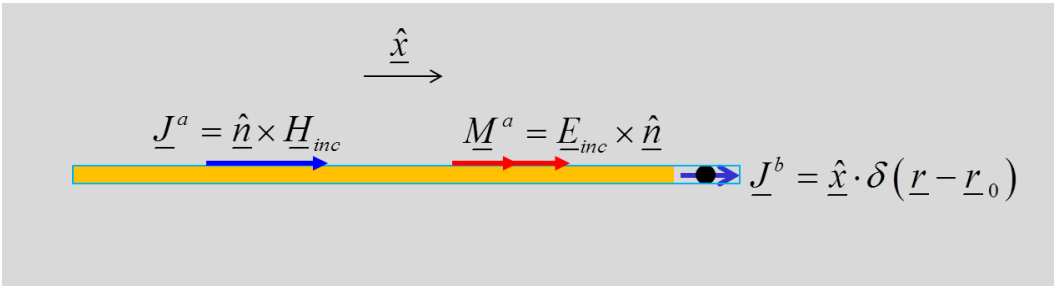

Figure 4-20 Shrink the equivalent incident field plane to the surface of leads structure.

If a surface which is infinitesimal close to the bounding box of metallic leads is selected, as shown in Figure 4-20, the boundary condition of PEC can be applied. And the tangential electric field $\underline{E}^a$ generated by source $\underline{J}^a$ will vanish, so

$$\int_V \left(\underline{H}^b \cdot \underline{M}^a \right) dV = \int_V \left(\underline{E}^a \cdot \underline{J}^b \right) dV . \qquad [4\text{-}3]$$

Since $\underline{J}^b$ is a dipole testing current in the x direction, the right hand side of Equation xx is equal to the x component of $\underline{E}^a$. Thus,

$$\int_V \left(\underline{H}^b \cdot \underline{M}^a \right) dV = E_x^a \,. \qquad [4\text{-}4]$$

The x component of the tip electric field E_x^a can be expressed using the following formula,

$$E_x^a = \int_V \left(\underline{H}^b \cdot \underline{M}^a \right) dV \,, \qquad [4\text{-}5]$$

The integration of $\underline{H}^b$ and $\underline{M}^a$ is evaluated by applying vector identity,

$$\underline{H}^b \cdot (-\underline{n} \times \underline{E}^{inc}) = \underline{E}^{inc} \cdot (\underline{H}^b \times -\underline{n}) \,, \qquad [4\text{-}6]$$

and

$$\underline{M}^a = -\underline{n} \times \underline{E}^{inc} \,, \qquad [4\text{-}7]$$

$$\underline{E}^a = \left(\int_V \underline{H}^b \cdot (-\underline{n} \times \underline{E}^{inc}) dV \right). \qquad [4\text{-}8]$$

The final expression for $\underline{E}^a$ is,

$$\underline{E}^a = \int_l \underline{E}^{inc}(l) \cdot \underline{I}(l) dl \,, \qquad [4\text{-}9]$$

where $\underline{I}(l)$ is the current along the lead path when a current source $\underline{J}^a$ is applied at the lead tip.

The maximum tangential electric field can be obtained using the Tier 3 approach. However, the tip heating is not directly related to the tangential electric field. To evaluate the tip heating, either the tip electric field or the tip specific absorption rate (SAR) is required. Thus, some efficient method is required to get tip electric field information rather than using brute force FDTD simulation.

In the following sections, Equation xx derived from the reciprocity theorem will be validated. The first example is the evaluation of the tip electric field for a simplified

coaxial leads model. In this study, the lead is modeled as a coaxial structure with a 30 cm length. Four different lead orientations (L1, L2, L3, and L4) in the ASTM phantom are shown in Figure 4-21.

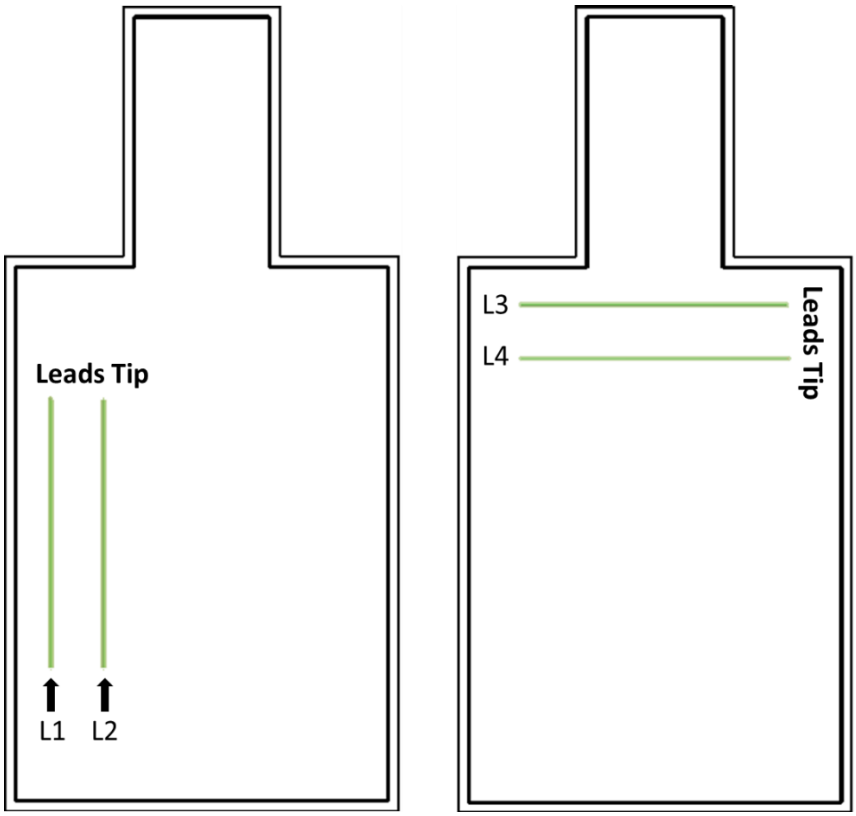

Figure 4-21 Four leads orientations in ASTM phantom.

A testing current source is placed at the tip location. And the induced current along the lead path can be easily obtained. The magnitude and the phase of the induced current distribution along the lead are shown in Figure 4-22.

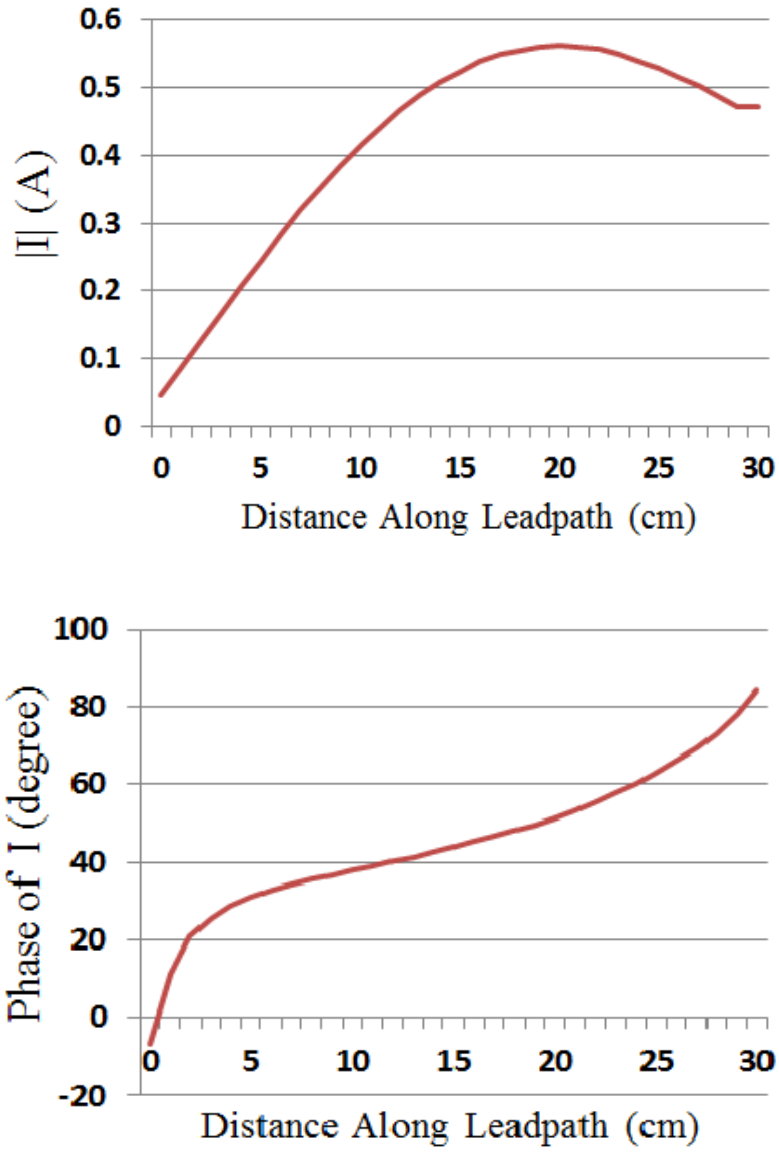

Figure 4-22 Induced current magnitude (top) and phase (bottom) due to a dipole testing current placement at lead tip.

The estimated electric field at the leads tip is evaluated using the induced current and the tangential electric field along the four lead paths (L1, L2, L3 and L4). Since the direct simulation electric field near the lead tip is singularity, the volume-averaged E field defined by ICNIRP-2010 is used for comparison [70]. Figure 4-23 shows the comparison

of E field at leads tip between direct simulation and reciprocity theorem. The estimation results from the reciprocity theorem agree well with the direct simulation results.

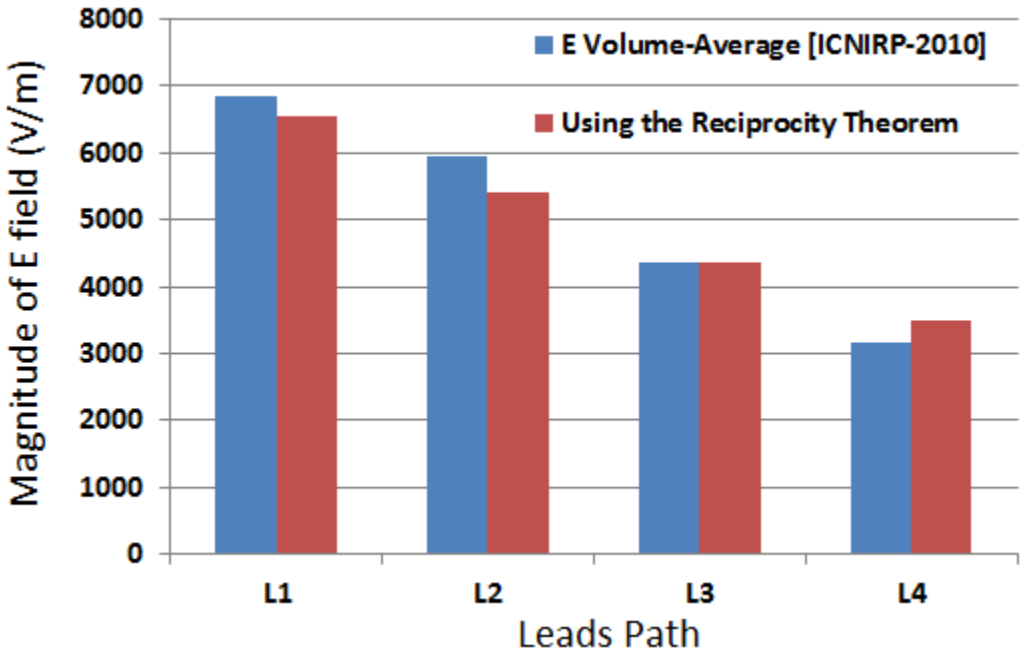

Figure 4-23 Comparison between E field at lead tip between direct simulation and estimation method by the reciprocity theorem.

The second example is a study of the relationship between Erms and RF heating. From the last equation, it is found that the induced current on the lead path has a phase difference larger than 90^{o} between the two ends of the lead structure. However, when the implant is small compared to the wavelength in the ASTM phantom at 64 MHz, the phase variation will have a minor effect on the final integration results. Thus, it will be feasible to evaluate the heating effect using the Erms value. The Erms is defined by,

$$E_{RMS} = \int E_{\tan} dl \,. \qquad [4\text{-}10]$$

In this study, a 10 cm long stent is used in the measurement. As is shown in Figure 4-24, the stent structure is a metallic mesh tube covered by an insulated coating material. At the left end, the metallic tube is fully coated while at the other end, the tube is partially

coated. During the measurement, it is noticed the maximum temperature rise is at the partially coated end marked by the red circle in Figure 4-24.

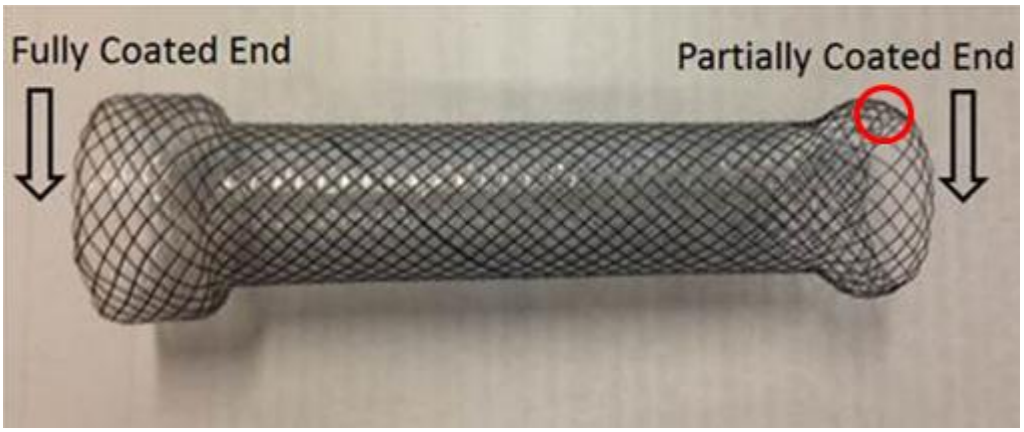

Figure 4-24 Stent structure and the worst heating location (red circle) at partially coated end.

Figure 4-25 shows the six locations of stent placement inside the ASTM phantom. The height of the ASTM gel is 14 cm and the center of the stent is aligned at 5 cm under the ASTM gel surface. The electric field is not symmetric since the stent is not placed at the center of the gel. The spacing between each two adjacent stent locations is 6 cm. The spacing is also 6 cm between the left/right stent and the phantom left/right edge, respectively. The measurement results for temperature rise at the red circle marked in Figure 4-24 is shown in Figure 4-26. Higher temperature rise is found when the stent is closer to the edge. By comparing the electric field plot in Figure xx and the temperature rise measurement curves in Figure 4-26, it indicates that there might be a relationship between the tangential electric field and the temperature increase.

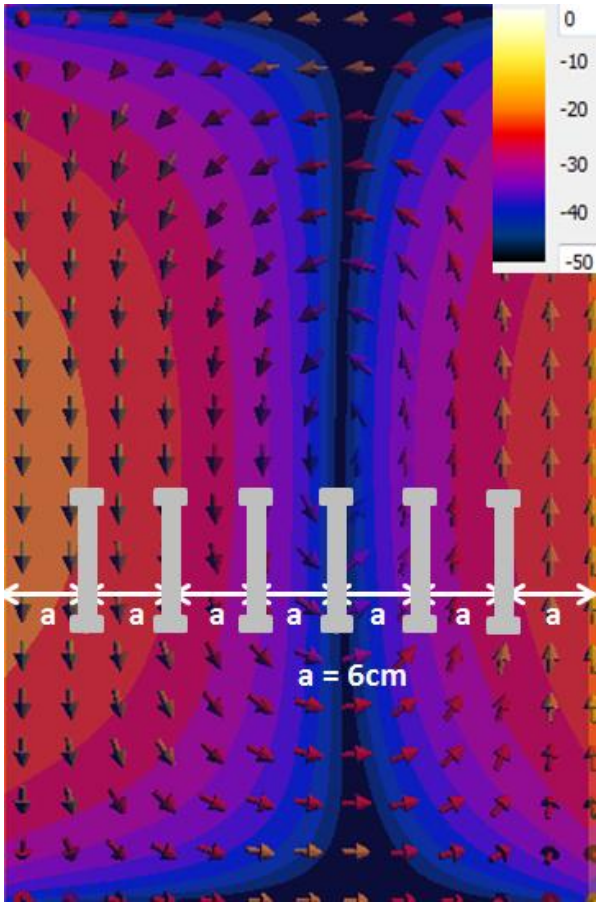

Figure 4-25 Stent placement in ASTM phantom with the incident E field distribution.

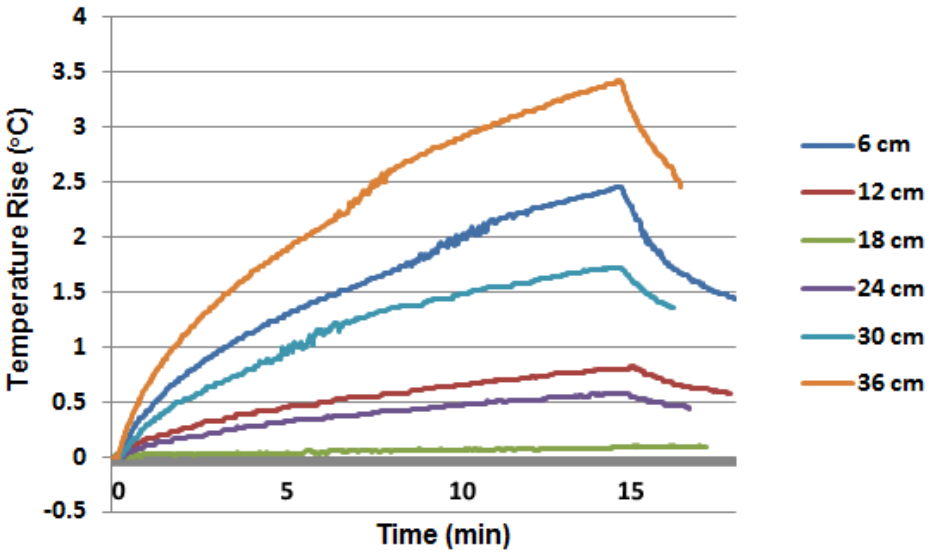

Figure 4-26 Measurement temperature rise for partially coated end of the stent with 6 different. locations.

The incident electric field data is extracted at the six stent locations and the Erms is calculated. Figure 4-27 shows the measurement temperature results with the temperature estimated using Erms. The maximum estimated temperature (at 36 cm) is scaled to the same value as that obtained from the measurement. The rest of the five estimation temperature results are then scaled using the same normalization factor. It is found most estimated data are accurate compared with the measurement. Therefore, scaling using Erms is considered as a good method to identify the heating effect for a short implant in the MRI RF environment.

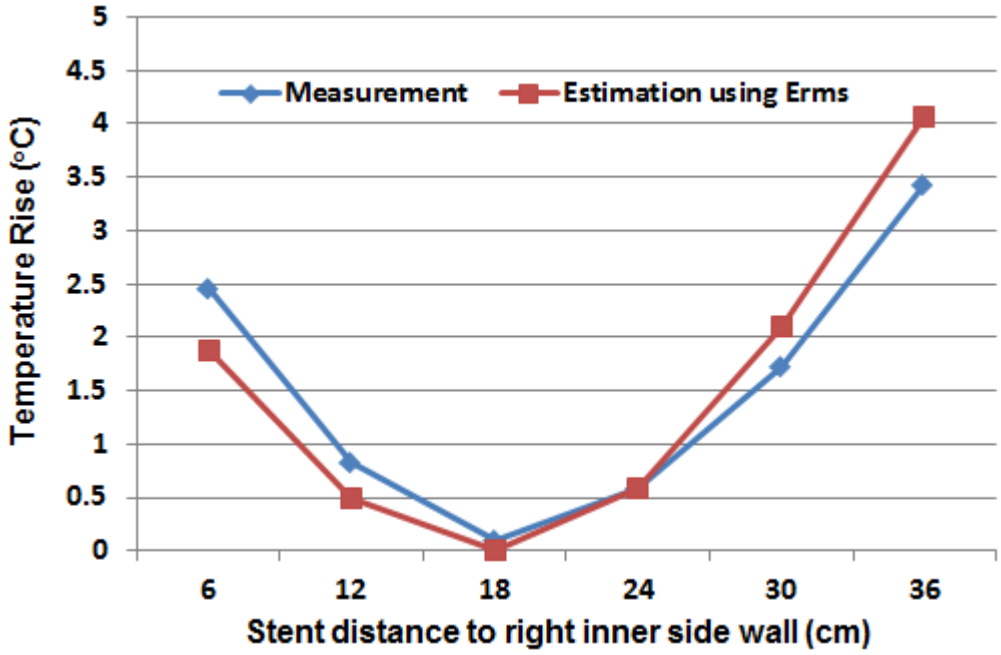

Figure 4-27 Comparison between temperature rise data between measurement and estimation method using Erms.

Chapter 5 Probe Effect during Measurement

5.1 Background

In Chapters 3 and 4, numerical simulations have been performed to study both passive and active medical devices. In order to compare with the simulation results, high precision measurement is desired. A typical experiment setup for temperature measurement of an external fixation system is shown in Figure 5-1. In this setup, four T2™ fiber optic temperature probes (Neoptix, Inc) are used to record temperature increase data when the MRI RF coil is turned on. Due to the rapidly changing gradient of temperature distribution around the worst heating spot, the measured temperature rise data from fiber optic thermal probes are very sensitive to the location where probes are placed. In order to monitor the device tip temperature increment more accurately, the probes are tied to the vertical pins of the external fixator, and the sensitive element on the head of the fiber optic probe is attached to the tip of the pins. This measurement error can be minimized by placing the thermal probe close to the surface of the device using a mounting device. However, Mattei, et al points out that even with similar experimental set-ups, the temperature increase results appear significantly different [10]. This inconsistency in the results might be related to the interference between the fiber optic temperature probe and the electromagnetic field distribution at the measurement location.

In this chapter, the temperature probe model is built into the previous numerical models to study the probe interference to temperature rise in the MRI. Three medical devices are investigated in this study: 1) spinal basis system, which is used to represent implanted orthopedic devices; 2) external fixator with two connection bars and two

insertion pins, which is used to represent external fixation devices; and 3) 20 cm long coaxial lead, which is used to represent the lead structure in AIMDs.

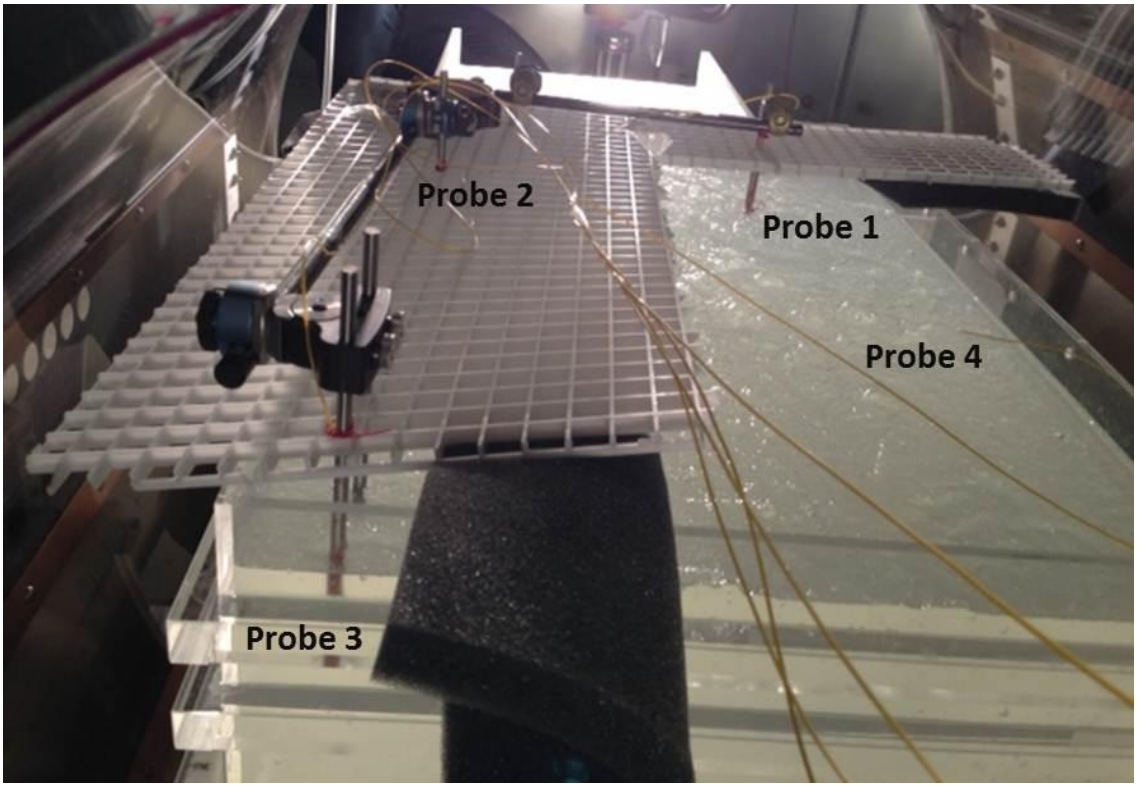

Figure 5-1 Temperature measurement of an external fixation device.

5.2 Methodology

The probe effect on temperature measurement will be studied using numerical simulation. Modeling of the transmitted RF coil as well as the device configuration in the ASTM heating phantom basically follows the description from Chapter 3. Three models are used in this numerical model: 1) the spinal basis system model with a length of 65 mm; 2) the external fixator model used in Chapter 3; and 3) a simplified pacemaker leads model.

The most important part for the probe effect study is the probe position for different medical devices. First of all, a simulation without any probe around the device is

used to find out the worst heating location. The probe is then placed with four different orientations at that location near the device. For different implants, the placement of the probe might be different due to the shape of the device.

Four different possible fiber optic temperature probe orientations are shown in Figure 5-2 for the spinal basis system. (a) is a vertical orientation with probe tip on the top; (b) is a vertical orientation with probe tip on the bottom; (c) is a horizontal orientation with the probe placed tightly along the shorter edge of device plate; (d) is a horizontal orientation with the probe placed perpendicular to the shorter edge of the device plate.

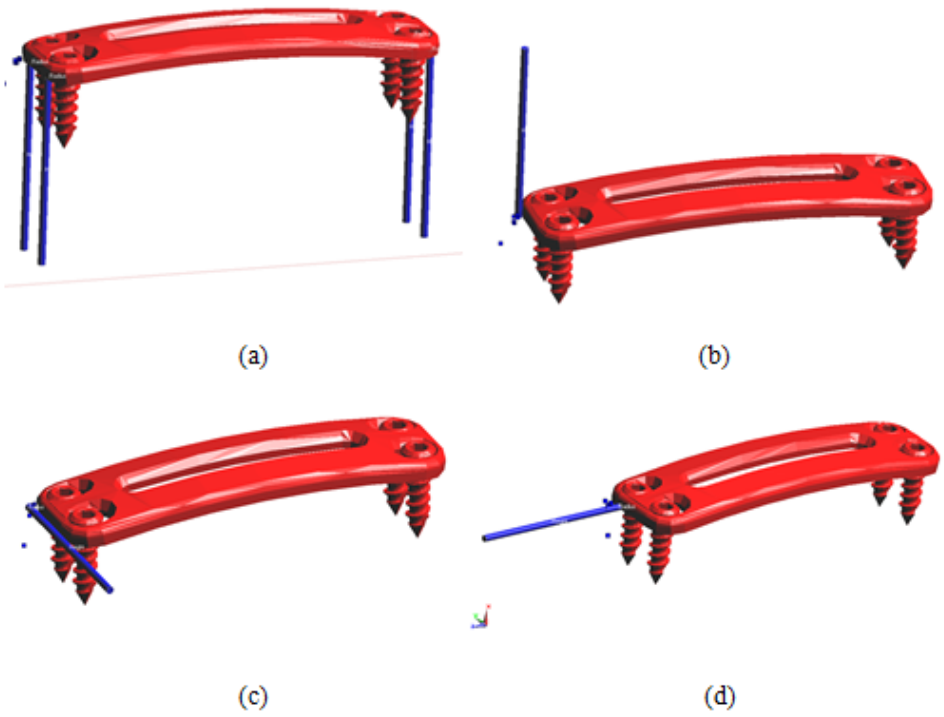

Figure 5-2 Thermal probes positions for the spinal basis system.

Figure 5-3 shows four different probe positions at the screw tip of the external fixation device. The images show that (a) is a vertical orientation, with a 90^{o}C angle

between probe and screw; (b) shows a 135^{o}C angle orientation; (c) shows a measurement location with the sensor touched from the bottom of the screw tip; (d) shows a measurement location with the sensor touching the top of the screw tip.

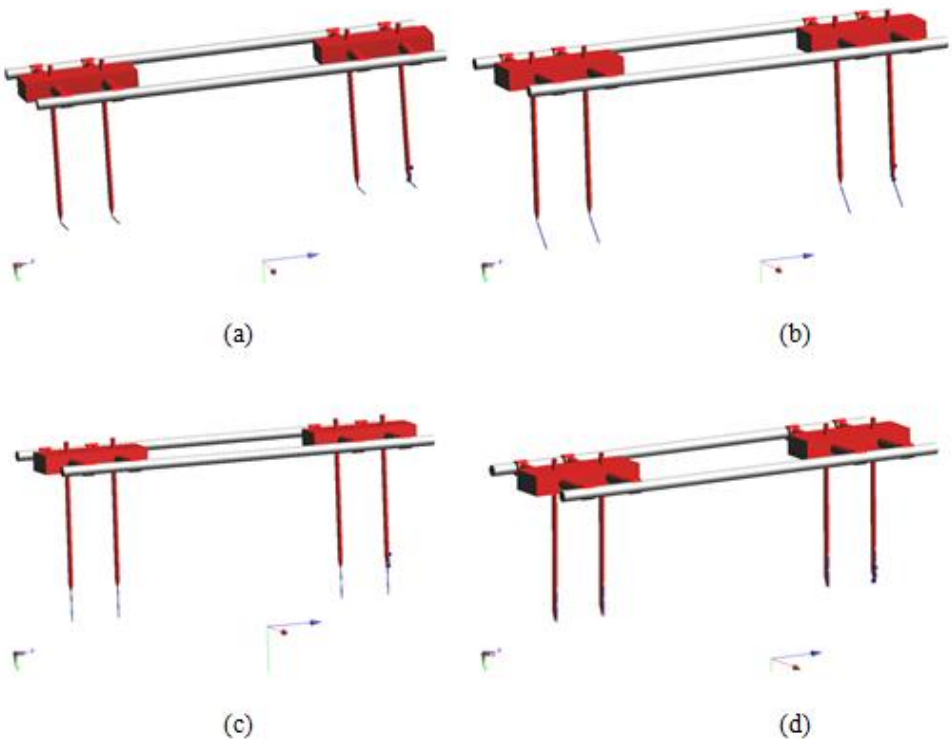

Figure 5-3 Temperature probes positions for the external fixation device.

The probe orientations for measurement of the pacemaker leads shown in Figure 5-4 are similar to those in Figure 5-3 for the external fixation device. The different degrees between the probes and the lead conductors are (a) 90 ^{o}C, (b) 0 ^{o}C, (c) 180 ^{o}C, (d) 135 ^{o}C. EM and thermal simulation are used to find out the effect of different probe orientations on the RF heating.

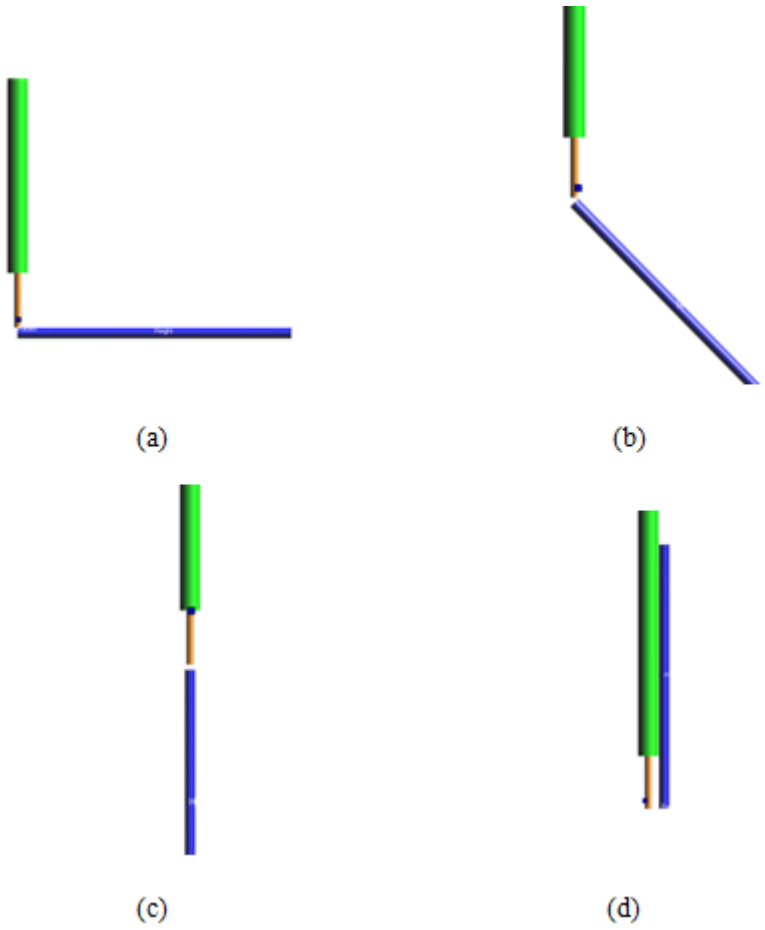

Figure 5-4 Temperature probes positions for AIMD lead strucuture.

5.3 Result and Discussion

The simulation results for the effect of fiber optic probe placement around the three different medical devices are shown in the following figures. Figure 5-5 and Table 5-1 show the results for the maximum temperature rise for the spinal basis system. It is found that around the edge of the metallic plate of the device, there is less than a 1.75 % temperature variation which indicates a negligible influence of the fiber optic probe on temperature measurement.

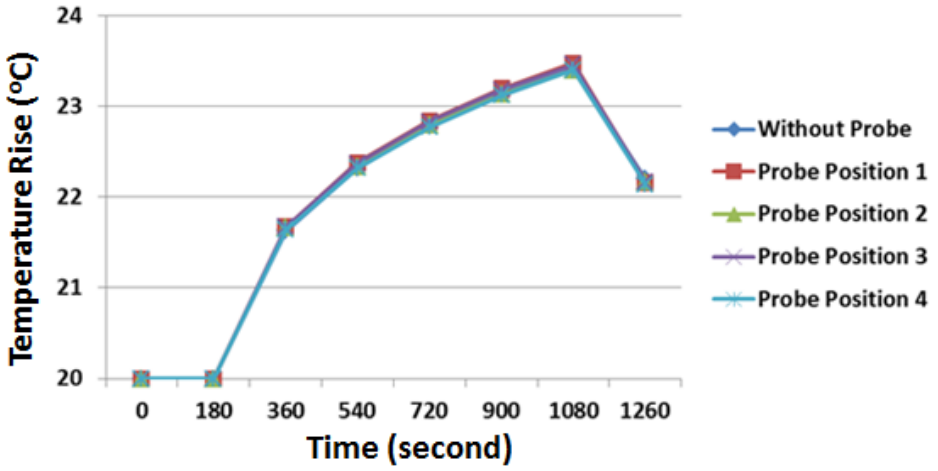

Figure 5-5 Temperature increase at the edge of plate for spinal basis system.

Table 5-1 SAR and Temperature rise results for spinal basis system

	Peak 1g Averaged SAR (W/Kg)	Error %	T increase @ 15 min (°C)	Error %
Without Probe	46.14	0.00	3.42	0.00
Probe Position 1	46.78	1.39	3.48	1.75
Probe Position 2	45.76	-0.82	3.40	-0.58
Probe Position 3	46.13	-0.02	3.46	1.17
Probe Position 4	46.01	-0.28	3.40	-0.58

Figure 5-6 and Table 5-2 show the maximum temperature rise results for the external fixation device. Placing the probe parallel to the screw (Position 3 and Position 4) has significantly less effect than the other two positions. By placing the probe 45° to the screw as shown in Figure 5-6 (b), the temperature rise change could go up to 27%, which cannot be considered as an accurate measurement configuration.

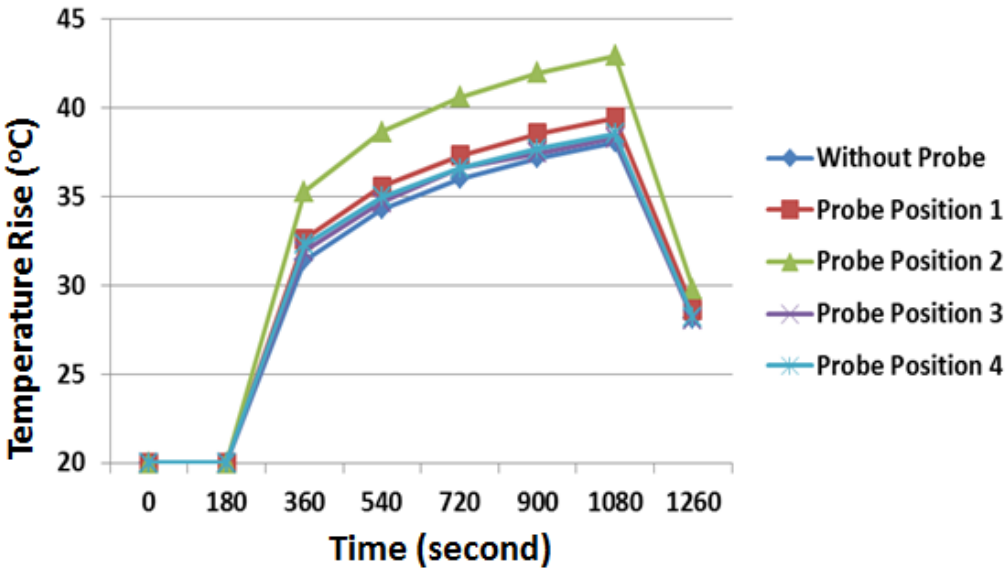

Figure 5-6 Temperature increase at screw tip for external fixation device.

Table 5-2 SAR and Temperature rise results for external fixation device

	Peak 1g Averaged SAR (W/Kg)	Error %	T increase @ 15 min (°C)	Error %
Without Probe	313.49	0.00	18.07	0.00
Probe Position 1	323.61	3.23	19.44	7.58
Probe Position 2	381.35	21.65	22.95	27.01
Probe Position 3	293.66	-6.33	18.30	1.27
Probe Position 4	298.34	-4.83	18.54	2.60

Figure 5-7 and Table 5-3 show the maximum temperature rise results for the lead structure. Similar to the results from the external fixator, the probe placed parallel to the lead path (Positions 3 and 4) has the nearest temperature rise compared to the simulation without the probe. Placing the temperature probe perpendicular to the lead will decrease the temperature rise by around 21%.

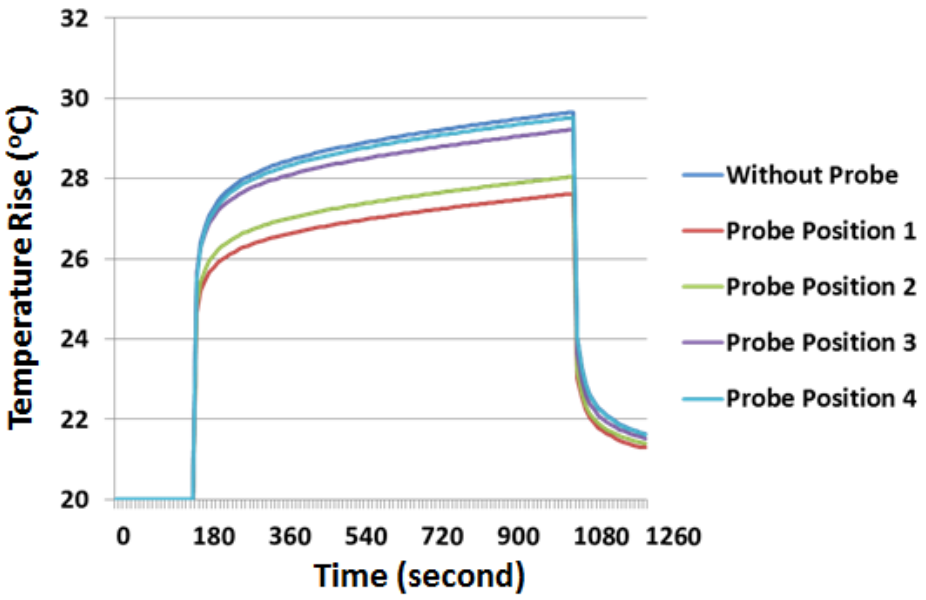

Figure 5-7 Temperature increase at lead tip.

Table 5-3 SAR and Temperature rise results for AIMD lead structure

	Peak 1g Averaged SAR (W/Kg)	Error %	T increase @ 15 min (oC)	Error %
Without Probe	47.50	0.00	9.66	0.00
Probe Position 1	35.90	-24.42	7.62	-21.14
Probe Position 2	38.00	-20.00	8.04	-16.76
Probe Position 3	41.20	-13.26	9.22	-4.55
Probe Position 4	47.00	-1.05	9.52	-1.48

From the simulation study, it is found during the MRI safety testing that the fiber optic temperature probe could have a greater effect on the measurement accuracy on a sharp and elongated structure (screw, leads) than a flat structure (metal plate). It is suggested the temperature probe be placed at a parallel configuration to the elongated screw or leads to minimize the measurement error.

Chapter 6 Conclusions and Future Work

6.1 Conclusions

The primary contribution of this thesis is the extensive studies of RF heating problems of medical devices in MRI systems. The basic implanted orthopedic devices are studied in Chapter 3. Full wave electromagnetic simulation and a thermal simulation tool are used to find a correlation between device length and the maximum temperature increment around the device tip. Measurement results for the worst case heating scenario are in good agreement with the simulation data. The work proposed an efficient and accurate method to evaluate the MRI RF heating effect for a device family with a large number of length variations. With the simulation results of temperature rise statistics for all devices in the device family, only the device that could induce a worst scenario heating effect was tested in the measurement. In the second part of Chapter 3, RF heating for the external fixation device was found to be related to not only the dimension (clamp spacing), but also insertion depth, bar materials, and insulation layer.

In Chapter 4, three methods are discussed for evaluating RF heating for leads structure in active implantable medical devices. The direct simulation method is usually not suggested because the fine structure may generate a huge mesh size that could easily exceed computer memory. A more frequently used method is the four-tier approach. As an example, the Tier 3 method is used to analyze the tangential electric field along a huge number of clinical representative lead pathways with variations in patient size, coil dimension, patient location, permittivity and electrical conductivity for human tissue. The advantage for the Tier 3 approach is its flexibility to increase the number of leads

configurations at any time. The increase of leads configurations will not increase the simulation number. However, Tier 3 provides an overestimation for leads heating so that a product that fails to pass Tier 3 does not mean the product is unsafe in the MRI. Therefore, a third method is proposed to establish a relation between leads heating and incident field using the reciprocity theorem. The reciprocity theorem can solve the leads heating problem very well from a theoretical point of view. It is observed that for straight leads, the estimation of a tip electric field using the reciprocity theorem matches well with the direct simulation results. For a short implant the phase variation has a minor effect on the tip electric field and the RF heating can be quantified using the Erms value. However, further work needs to be done to improve the accuracy of this method.

The measurement error induced by the existence of the fiber optic temperature probe is investigated in Chapter 5. The simulation results indicate a maximum of a 50% temperature change when the temperature probe is placed near the tip of the screws. However, for large and flat metal surfaces of the medical device, the probe will not affect the temperature distribution. This study indicates that in order to get more accurate temperature data from the measurement, the temperature probe needs to be placed perpendicular to the device tip rather than be placed in line with the device path.

6.2 Future Work

A lot of topics related to RF induced heating for medical devices in MRIs have been discussed in previous chapters. However, the RF heating problem will always be an active area of research due to the continuous design of new generation medical devices

and the increasing needs for MRI compatible devices. According to the current progress discussed in the dissertation, some future works need to be worked on.

First, for some device families with large a volume of implants with different lengths and components, it is usually impossible to simulate all the device configurations in the MRI RF coil. An optimized method which can be applied to find out the worst heating configuration in minimum numbers of simulations will make it much easier to evaluate the MRI safety problems for the device family with a huge number of devices.

Second, to evaluate the temperature rise for devices like the cardiac pacemaker, the reciprocity approach needs to be further developed so the heating can be calculated with a known tangential electric field distribution along the lead path and a transfer function between the leads tip and points on lead path. The tangential electric field distribution is obtained from theb Tier 3 method as mentioned in Chapter 4. The transfer function, however, needs to be measured using a well-designed experimental approach.

Third, the insulation material used in the external fixation device is found to have a significant effect on reducing RF heating for the device in Chapter 3. However, the electrical conductivity variation could also contribute to the RF heating. Even more, the electrical conductivity for the insulation layer used in the external fixation device can be assigned artificially by choosing an appropriate material which might be potentially helpful in reducing RF heating of the device. A complete study of insulation layer configurations, including material properties, and layer dimension with the effect on RF heating will be studied in the future to help with the optimized design of MRI conditional external fixation devices.

References

[1] T. O. Wood, "Standards for medical devices in MRI: present and future," *Journal of Magn. Reson. Imaging*, Vol. 26, pp. 1186-1189, 2007.

[2] ASTM F2052-06el, "Standard test method for measurement of magnetically induced displacement force on medical devices in the magnetic resonance environment," ASTM International, West Conshohocken, PA, 2006.

[3] ASTM F2213-06, "Standard test method for measurement of magnetically induced torque on medical devices in the magnetic resonance environment," ASTM International, West Conshohocken, PA, 2006.

[4] ASTM F2182-11a, "Standard test method for measurement of radio frequency induced heating on or near passive implants during magnetic resonance imaging," ASTM International, West Conshohocken, PA, 2011.

[5] E. Mattei, M. Tribenti, and G. Calcagnini, "Complexity of MRI induced heating on metallic leads: experimental measurements of 374 configurations," *Biomedical Engineering Online*, Vol. 7, No. 11, pp. 1-16, 2008.

[6] H. S. Ho, "Safety of metallic implants in magnetic resonance imaging," *Journal of Magn. Reson. Imaging*, Vol. 14, pp. 472-474, 2001.

[7] C. K. Chou, J. A. McDougall, and K. W. Chan. "RF heating of implanted spinal fusion stimulator during magnetic resonance imaging," *IEEE Trans. Biomed. Eng.*, Vol. 44, pp. 367-372, 1997.

[8] J. A. Nyenhuis, A. V. Kildishev, J. D. Bourland, K. S. Foster, G. P. Graber, and T. W. Athey, “Heating near implanted medical devices by the MRI RF-magnetic field,” *IEEE Trans. Magn.*, Vol. 35, pp. 4133-4135, 1999.

[9] J. A. Nyenhuis, S. M. Park, and R. Kamondetdacha, “MRI and implanted medical devices: basic Interactions with an Emphasis on Heating,” *IEEE transactions on device and materials reliability*, Vol. 5, No. 3, pp. 467-479, 2005.

[10] E. Mattei, G. Calcagnini, F. Censi, M. Triventi, and P. Bartolini, “numerical model for estimating RF-induced heating on a pacemaker implant during MRI: experimental validation,” *IEEE Trans. Biomed. Eng.*, Vol. 57, No. 8, pp. 2045-2052, 2010.

[11] E. T. Martin, J. A. Coman, F. G. Shellock, C. C. Pulling, R. Fair, and K. Jenkins, “Magnetic resonance imaging and cardiac pacemaker safety at 1.5-Tesla,” *J. Amer. Coll. Cardiol.*, Vol. 43, pp. 1315-1324, 2004.

[12] A. R. Rezai, D. Finelli, J. A. Nyenuis, G. Hrdlicka, J. Tkach, A. Sharan, P. Rugieri, P. H. Stypulkowski, and F. G. Shellock, "Neurostimulation systems for deep brain stimulation: in vitro evaluation of magnetic resonance imaging-related heating at 1.5 tesla," *Journal of Magn. Reson. Imaging*, Vol. 15, pp. 241-250, 2002

[13] L. T. Blouin, F. I. Marcuis, and L. Lampe, “Assessment of effects of a radiofrequency field and thermistor location in an electrode catheter on the accuracy of temperature measurement,” *Pacing Clin. Electrophysiol*, Vol. 14, pp. 807-13, 1991.

[14] J. Chen, Z. Feng, and J. Jin, “Numerical simulation of SAR and B1-field inhomogeneity of shileded RF coils loaded with the human head,” *IEEE Trans. Biomed. Eng.*, Vol. 45, pp. 650-659, 1998.

[15] D. Formica and S. Silvestri, “Biological effects of exposure to magnetic resonance imaging: an overview,” *Biomedical Engineering Online*, Vol. 3, No. 11, pp. 1-12, 2004

[16] C. M. Collins, W. Liu, and J. Wang, “Temperature and SAR calculations for a human head within volume and surface coils at 64 and 300 MHz,” *Journal of Magn. Reson. Imaging*, Vol. 19, pp. 650-656, 2004.

[17] P. Bernardi, M. Vavagnaro, S. Pisa, and E. Piuzzi, "SAR distribution and temperature increase in an anotomical model of the human eye exposed to the field radiated by the user antenna in a wireless LAN," *IEEE Trans. Microwave Theory Tech.*, Vol. 46, No. 12, 1998.

[18] J. Wiart, and R. Mittra, "Calculation of the power absorbed by tissues in case of hand set mobile antenna close to biological tissue," *Proc. IEEE Symp. Antennas Propagat.*, pp. 1104-1107, Baltimore, Maryland, July, 1996.

[19] P. Bernardi, M. Cavagnaro, S. Pisa, and E. Piuzzi, "Power absorption and temperature elevations induced in the human head by a dual-band monopole-helix antenna phone," *IEEE Trans. Microwave Theory Tech.*, Vol. 49, No. 12, 2001.

[20] A. Hirata, M. Morita, and T. Shiozawa, "Temperature increase in the human head due to a dipole antenna at microwave frequencies," *IEEE Trans. EMC*, Vol. 45, No. 1, 2003.

[21] T. W. Athey, "A model of temperature rise in the head due to magnetic resonance imaging procedures," *Magn. Reson. Med.*, Vol. 9, pp. 177-184, 1989.

[22] J. Jin, *Electromagnetic analysis and design in magnetic resonance imaging*. Boca Raton, Florida, CRC Press, 1988.

[23] SEMCAD X. Reference manual for the SEMCAD simulation platform for electromagnetic compatibility, antenna design and dosimetry, SPEAG - Schmid & Partner Engineering, 2011.

[24] P. Nordbeck, F. Fidler, I. Weiss, M. Warmth, M. T. Friedrich, P. Ehses, W. Geistert, O. Ritter, P. M. Jarob, M. E. Ladd, H. H. Quick, and R. Bauer, "Spatial distribution of RF-induced E-fields and implant heating in MRI," *Magn. Reson. Med.*, Vol. 60, No. 2, pp. 312-319, 2008.

[25] "Recommended practice for measurements and computations with respect to human exposure to radiofrequency electromagnetic fields, 100 kHz to 300 GHz," *IEEE Standard* C95.3 (Institute of Electrical and Electronics Engineers), 2002.

[26] H. H. Pennes, "Analysis of tissue and arterial blood temperatures in the resting human forearm," *Journal of Applied Physiol.*, Vol. 1, pp. 93-122, 1948.

[27] "Assessment of the safety of magnetic resonance imaging for patients with an active implantable medical device," ISO/TS 10974:2012(E).

[28] S. M. Park, J. A. Nyenhuis, C. D. Smith, E. J. Lim, K. S. Foster, and K. B. Baker, "Gelled vs. non-gelled phantom material for measurement of MRI induced temperature increases with bioimplants," *IEEE Trans. Magn.*, Vol. 39, pp. 3367-71, 2003.

[29] S. Oh, A. G. Webb, T. Neuberger, B. Park, and C. M. Collins, "Experimental and numerical assessment of MRI-induced temperature change and SAR distributions in phantoms and in vivo," *Magn. Reson. Med.*, Vol. 63, pp. 218-223, 2010.

[30] ASTM D2413-99, “Standard practice for preparation of insulating paper and board impregnated with a liquid dielectric,” ASTM International, West Conshohocken, PA, 2009.

[31] ASTM D149-09, “Standard test method for dielectric breakdown voltage and dielectric strength of solid electrical insulating materials at commercial power frequencies,” ASTM International, West Conshohocken, PA, 2009.

[32] J. Powell, A. Papadaki, J. Hand, A. Hart, and D. McRobbie, “Numerical simulation of SAR induced around Co-Cr-Mo hip prostheses in situ exposed to RF fields associated with 1.5- and 3-T MRI body coils,” *Magn. Reson. Med.*, Vol. 68, pp. 960-68, 2012.

[33] H. Muranaka, “Evaluation of RF heating on hip joint implant in phantom during MRI examinations,” *Nippon Hoshasen Gijutsu Gakkai Zasshi*, Vol. 66, pp. 725-33, 2010.

[34] R. Kumar, R. A. Lerski, S. Gandy, B. A. Clift, and R. J. Abbound, “Safety of orthopaedic implants in magnetic resonance imaging: An experimental verification,” *Journal of Orthopaedic Research*, Vol.24, pp. 1799-1802, 2009.

[35] R. Luechinger, P. Boesiger, and J. A. Disegi, “Safety evaluation of large external fixation clamps and frames in a magnetic resonance environment,” *Journal of Biomed Mater. Res. B Appl. Biomater.*, Vol. 82, pp. 17-22, 2007.

[36] K. B. Baker, J. A. Tkach, J. A. Nyenhuis, M. Philips, F. G. Shellock, J. Gonzalez-Martinez, and A. R. Rezai, “Evaluation of specific absorption rate as a dosimeter of MRI-related implant heating,” *Journal of Magn. Reson. Imaging*, Vol. 20, pp. 315-20, 2004.

[37] P. L. T. Brian, “A finite-difference method of high-order accuracy for the solution of three-dimensional transient heat conduction problem,” *Amer. Inst. Chem. Eng. J.*, Vol. 7, No. 3, pp. 367–370, 1961.

[38] P. P. Gandhi, Q. Li, and G. Kang, "Temperature rise for the human head for cellular telephones and for peak SARs prescribed in safety guidelines," *IEEE Trans. Microwave Theory Tech.*, Vol. 49, No. 9, 2001.

[39] E. Neufeld, S. Kuhn, G. Szekely, and N. Kuster, “Measurement, simulation, and uncertainty during MRI,” *Phys. Med. Biol.*, Vol. 54, pp. 4151-4169, 2009.

[40] A. Amjad, R. Kamondetdacha, A. V. Kildishev, S. M. Park, and J. A. Nyenhuis, “Power deposition inside a phantom for testing of MRI heating,” *IEEE Trans. Magn.*, Vol. 41, pp. 4185-4187, 2005.

[41] A. T. Fragomen and S. R. Rozbruch, “The mechanics of external fixation,” *HSS J.*, Vol. 3, No. 1, pp. 13-29, 2007.

[42] M. Kowalski, E. H. Schemitsch, R. M. Harringto, J. R. Chapman and M. F. Swiontkowski, “Comparative biomechanical evaluation of different external fixation sidebars: stainless-steel tubes versus carbon fiber rods,” *J. Orthop. Trauma.*, Vol. 10, No. 7, pp. 470-5, 1996.

[43] Y. Liu, J. Chen, F. G. Shellock, and W. Kainz, “Computational and experimental studies of an orthopedic implant: MRI-related heating at 1.5-T/64-MHz and 3-T/128-MHz,” *Journal of Magn. Reson. Imaging*. doi: 10.1002/jmri.23764. [Epub ahead of print], July, 2012.

[44] Y. Liu, J. Shen, W. Kainz, S. Qian, W. Wu, and J. Chen, "Computational study of external fixation devices surface heating in MRI RF environment," IEEE Symposium on Electromagnetic Compatibility, Pittsburgh, August, 2012.

[45] W. Kainz, G. Neubauer, R. Uberbacher, F. Alesch, and D. D. Chan, "Temperature measurement on neurological pulse generators during MR scans," *Biomedical Engineering Online*, Vol. 1, No. 2, pp. 1-8, 2002.

[46] S. Achenbach, W. Moshage, B. Diem, T. Bieberle, and V. Schibgilla, "Effects of magnetic resonance imaging on cardiac pacemakers and electrodes," *American Heart Journal*, Vol. 134, pp. 467-73, 1997.

[47] T. Sommer, C. Vahlhaus, G. Lauck, A. V. Smekal, M. Reinke, U. Hofer, W. Block, F. Traber, C. Schneider, J. Gieseke, W. Jung and Schild H, "MR imaging and cardiac pacemakers: in-vitro evaluation and in-vivo studies in 51 patients at 0.5 T," *Radiology*, Vol. 215, No. 3, pp. 869-79, 2000.

[48] S. Pisa, G. Calcagnini, M. Cavagnaro, E. Piuzzi, E. Mattei and P. Bernardi, "A study of the interaction between implanted pacemakers and the radio-frequency field produced by magnetic resonance imaging apparatus," IEEE Trans. EMC, Vol. 50, No. 1, pp. 35-42, 2008.

[49] R. Gray, W. T. Bibens, F. G. Shellock, "Simple design changes to wires to substantially reduce MRI-induced heating at 1.5 T: implications for implanted leads," *Magnetic Resonance Imaging*, Vol. 23, pp. 887-891, 2005.

[50] C. J. Yeung, R. C. Susil, and E. Atalar, "RF safety of wires in interventional MRI: using a safety index," *Magn. Reson. Med.*, Vol. 47, pp. 187-193, 2002.

[51] C. D. Smith, A. V. Kildishev, J. A. Nyenhuis, K. S. Foster, and J. D. Bourland, "Interactions of MRI magnetic fields with elongated medical implants," *J. Appl. Physics*, Vol. 87, pp. 6188-6190, 2000.

[52] S. M. Park, R. Kamondetdacha, A. Amjad, J. A. Nyenhuis, "MRI safety: RF induced heating on straight wires," *IEEE Trans. Magn.*, Vol. 41, pp. 4197-4199, 2005.

[53] H. Bassen, W. Kainz, G. Mendoza, and T. Kellom, "MRI-induced heating of selected thin wire metallic implants-laboratory and computational studies - findings and new questions raised," *Minim Invasive Ther. Allied Technol.*, Vol. 15, No. 2, pp. 76-84, 2006.

[54] C. J. Yeung, R. C. Susil, and E. Atalar, "RF heating due to conductive wires during MRI depends on the phase distribution of the transmit field," *Magn. Reson. Med.*, Vol. 48, No. 6, pp. 1096-8, 2002.

[55] P. Büchler, A. Simon, and J. Burger, "Safety of active implantable devices during MRI Examinations: a finite element analysis of an implantable pump," *IEEE Trans. Biomed. Eng.*, Vol. 54, No. 4, pp. 726-733, 2007.

[56] L. M. Angelone, J. Ahvenien, J. W. Belliveau, and G. Bonmassar, "Analysis of the role of lead resistivity in specific absorption rate for deep brain stimulator leads at 3T MRI," *IEEE Trans. Med. Imaging*, Vol. 29, pp. 1029-1038, 2010.

[57] E. Mattei, M. Triventi, G. Calcagnini, F. Censi, W. Kainz, H. I. Bassen, and P. Bartolini, "Temperature and SAR measurement errors in the evaluation of metallic linear structures heating during MRI using fluoroptic probes," *Phys. Med. Biol.*, Vol. 52, No. 6, pp. 1633-46, 2007.

[58] http://www.speag.com/products/semcad/solutions/hpc-solutions/hardware-acceleration, 2012.

[59] A. Christ, W. Kainz, E. G. Hahn, K. Honegger, M. Zefferer, E. Neufeld, W. Rascher, R. Janka, W. Bautz, J. Chen, B. Kiefer, P. Schmitt, H. P. Hollenbach, J. Shen, M. Oberle, D. Szczerba, A. Kam, J. W. Guag, and N. Kuster. "The virtual family--development of surface-based anatomical models of two adults and two children for dosimetric simulations," *Phys. Med. Biol.*, Vol. 55, pp. 23-28, 2009.

[60] IT'IS Virtual Population Project http://www.itis.ethz.ch/research/virtual-population/virtual-population-project/, 2010.

[61] C. Hayes. "Radio frequency field coil for NMR," U.S. Patent #4,694,255, September 15, 1987.

[62] E. Neufeld, M. C. Gosselin, M. Murbach, A. Christ, E. Cabot, and N. Kuster, "Analysis of the local worst-case SAR exposure caused by an MRI multi-transmit body coil in anatomical models of the human body," *Phys. Med. Biol.*, Vol. 56, pp. 4649-4659, 2011.

[63] R. W. Overall, J. M. Pauly, P. P. Stang, and G. C. Scott, "Ensuring safety of implanted devices under MRI using reverse RF polarization," *Magn. Reson. Med.*, Vol. 64, pp. 823-833, 2010.

[64] S. Gabriel, R. W. Lau, and C. Gabriel, "The dielectric properties of biological tissues: II measurements in the frequency range 10Hz to 20GHz," *Phys. Med. Biol.*, Vol. 41, pp. 2251-2269, 1996.

[65] S. Gabriel, R. W. Lau, and C. Gabriel, “The dielectric properties of biological tissues: III parametric models for the dielectric spectrum of tissues,” *Phys. Med. Biol.*, Vol. 41, pp. 2271-2293, 1996.

[66] P. Gajsek, W. D. Hurt, J. M. Ziriax, and P. A. Mason, “Parametric dependence of SAR on permittivity values in a man model,” *IEEE Trans. Biomed. Eng.*, Vol. 48, No. 10, 2001.

[67] J. F. Schenck, “Radiofrequency coils: types and characteristics,” *The Physics of MRI, Medical Physics Monograph*, No. 21, American Institute of Physics, New York, pp. 98-134. 1993.

[68] D. Schaefer. “Design of magnetic resonance systems”. *Standard Handbook of Biomedical Engineering and Design*, McGraw Hill, 2003.

[69] R. Qiang, J. Chen, S. Min, I. Viohl, A. Keef, T. Cox and W. Kainz, “An efficient estimation of electric field at leads tip using the reciprocity theorem,” Annual meeting for Bioelectromagnetics, Seoul, South Korea, June, 2010.

[70] ICNIRP Guidelines, “Guidelines for limiting exposure to time-varying electric and magnetic fields (1 Hz to 100 kHz),” *Health Physics*, Vol. 99, No. 6, pp. 818-836, 2010.